Evaluation of Repair Techniques for Impact-Damaged Prestressed Beams

FINAL REPORT
April, 2017

Submitted by

Michael Gangi
Mark Jones
Justin Liesen
Jiaxing Zhou
Research Assistants, Virginia Tech

Vanessa Pino
Research Assistant, University of Miami

Thomas E. Cousins, Ph.D., P.E.
Professor, Clemson University

C.L. Roberts-Wollmann, Ph.D., P.E.
Professor, Virginia Tech

Ioannis Koutromanos, Ph.D.
Assistant Professor, Virginia Tech

Antonio Nanni, Ph.D.
Professor, University of Miami

Submitted to Project Manager
Michael C. Brown, Ph.D., P.E.
Associate Director
Virginia Transportation Research Council

Contract Research Sponsored by

DISCLAIMER

The project that is the subject of this report was done under contract for the Virginia Department of Transportation, Virginia Transportation Research Council. The contents of this report reflect the views of the author(s), who is responsible for the facts and the accuracy of the data presented herein. The contents do not necessarily reflect the official views or policies of the Virginia Department of Transportation, the Commonwealth Transportation Board, or the Federal Highway Administration. This report does not constitute a standard, specification, or regulation. Any inclusion of manufacturer names, trade names, or trademarks is for identification purposes only and is not to be considered an endorsement.

Each contract report is peer reviewed and accepted for publication by staff of Virginia Transportation Research Council with expertise in related technical areas. Final editing and proofreading of the report are performed by the contractor.

This document is disseminated under the sponsorship of the Department of Transportation, University Transportation Centers Program, in the interest of information exchange. The U.S. Government assumes no liability for the contents or use thereof.

Standard Title Page - Report on Federally Funded Project

1. Report No. CAIT-UTC-035	2. Government Accession No.	3. Recipient's Catalog No.
4. Title and Subtitle Evaluation of Repair Techniques for Impact Damaged Prestressed Beams		5. Report Date April, 2017
		6. Performing Organization Code CAIT/Virginia Tech
7. Author(s) Mark Jones, Mike Gangi, Justin Leisen, Vanessa Pino, Carin L. Roberts-Wollmann, Thomas Cousins, Ioannis Koutromanos, Toni Nanni		8. Performing Organization Report No. CAIT-UTC-035
9. Performing Organization and Address Virginia Center for Transportation Innovation and Research 530 Edgemont Road Charlottesville, VA 22903		10. Work Unit No. (TRAIS)
		11. Contract or Grant No. DTRT12-G-UTC16
12. Sponsoring Agencies' Name and Address Virginia Department of Transportation Federal Highway Administration 1401 E. Broad Street 400 North 8th Street, Room 750 Richmond, VA 23219 Richmond, VA 23219-4825		13. Type of Report and Period Covered Final Report 07/01/2013-06/30/2015
		14. Sponsoring Agency Code

15. Supplementary Notes: U.S. Department of Transportation/OST-Office of the Assistant Secretary for Research and Technology
        1200 New Jersey Avenue, SE; Washington, DC 20590-0001

16. Abstract

   Collisions between over height vehicles and bridges occur about 1,000 times per year in the United States. Collision damage to bridges can range from minor to catastrophic, potentially requiring repair or replacement of a bridge beam. For prestressed concrete beams, the traditional repair methods are strand splices and Fiber-Reinforced Polymer (FRP) wraps. A new material, Fabric Reinforced Cementitious Matrix (FRCM), has been developed as an alternative to traditional FRP wrap.

   The first objective of this project was to damage, repair and test four beams retrieved during the demolition of the overpass of Arcadia Road over Interstate 81 at Arcadia, VA. The repair techniques evaluated were strand splices, FRP, FRCM and a combination of FRCM and strand splices. The beams were tested in the lab in simple span configuration with the repair location placed in a region of constant moment. Loads were applied monotonically to failure. One beam was tested in an undamaged condition as a control.

   Several methods were used to calculate strength and behavior. Simple methods from AASHTO and ACI were used for hand calculations of flexural strength. Conventional strain compatibility was also used. Non-linear beam models and non-linear three dimensional finite element models were also investigated as tools to evaluate repaired beams. Material characterization was performed on the concrete, prestressing steel, splice chucks, FRP and FRCM. The material characterization was used to develop the material models for the analyses.

   It was found that the greatest percentage of original strength was returned by the FRP repair and the repair with the combination of FRCM and splice chucks. The lowest percent was returned with only splice chucks when eight of 48 strands were severed and spliced. The FRCM proved to be a viable repair technique, but should be tested in fatigue before deployment on a bridge with high truck traffic. The analysis methods were shown to provide good estimates of strength and load-deflection behavior.

17 Key Words Prestressed Beam Repair, FRP, FRCM, Strand Splices	18. Distribution Statement No restrictions. This document is available to the public through NTIS, Springfield, VA 22161.		
19. Security Classif. (of this report) Unclassified	20. Security Classif. (of this page) Unclassified	21. No. of Pages 79	22. Price

Form DOT F 1700.7 (8-72)   Reproduction of completed page authorized

ABSTRACT

Collisions between over-height vehicles and bridges occur about 1,000 times per year in the United States. Collision damage to bridges can range from minor to catastrophic, potentially requiring repair or replacement of a bridge beam. For prestressed concrete beams, the traditional repair methods are prestressed strand splices and fiber-reinforced polymer (FRP) wraps. A new material, fabric-reinforced cementitious matrix (FRCM), has been developed as an alternative to traditional FRP wrap.

The first objective of this project was to damage, repair and test four beams retrieved during the replacement of the overpass of Arcadia Road over Interstate 81 at Arcadia, VA. The repair techniques evaluated were strand splices, FRP, FRCM and a combination of FRCM and strand splices. The beams were tested in the lab in a simple-span configuration such that each repaired section was subject to uniform moment. Loads were monotonically increased to the point of beam failure. One beam was tested in an undamaged condition as a control.

Several methods were used to calculate strength and flexural behavior. Simple methods from AASHTO and ACI were used for hand-calculations of flexural strength. Conventional strain compatibility was also used. Non-linear beam models and non-linear three-dimensional finite element models were also investigated as tools to evaluate repaired beams. Material characterization was performed on the concrete, prestressing steel, splice chucks, FRP and FRCM. The material characterization was used to develop the material models for the analyses.

It was found that the greatest percentage of original strength was returned by the FRP repair and the repair with the combination of FRCM and splice chucks. The lowest percent was returned by only splice chucks when eight of 48 strands were severed and spliced. The FRCM proved to be a viable repair technique, but should be tested in fatigue before deployment on a bridge with high volumes of truck traffic. The analysis methods were shown to provide good estimates of strength and load-deflection behavior.

FINAL CONTRACT REPORT

EVALUATION OF REPAIR TECHNIQUES FOR
IMPACT-DAMAGED PRESTRESSED BEAMS

Michael Gangi
Mark Jones
Justin Leisen
Research Assistants, Virginia Tech

Vanessa Pino
Research Assistant, University of Miami

Thomas E. Cousins, Ph.D., P.E.
Professor, Clemson University

C.L. Roberts-Wollmann, Ph.D., P.E.
Professor, Virginia Tech

Ioannis Koutromanos, Ph.D.
Assistant Professor, Virginia Tech

Antonio Nanni, Ph.D.
Professor, University of Miami

INTRODUCTION

Impact-Damaged Bridge Beams

Over-height vehicle collisions with overhead bridges occur frequently. Though data are unavailable on the exact number of over-height vehicle impacts that occur, it is estimated that 1,100 of these collisions occur in the United States every year (Agrawal et al. 2013). Many of these collisions are simple scrapes, but significant damage to the overhead bridge can occur, which may require repair or replacement of an individual beam or an entire bridge.

It is important to assess and classify the impact damage that occurs to determine how to proceed. Damage can be classified as minor, moderate, or severe (Harries et al., 2012). Minor damage includes shallow spalls, cracks, scrapes, and water stains, none of which affect the capacity of the girder (Harries et al., 2009). Repairs of minor damage are not essential, though they are often done for aesthetic or preventative maintenance purposes. Moderate damage includes larger and deeper cracks and sufficient spalling to expose prestressing strands, though not severing them. Moderate damage does not affect the capacity of the beam, and repairs are done to prevent further deterioration. Severe damage is further classified into three categories: Severe I, Severe II, and Severe III. Severe I damage requires structural repair to restore ultimate

1

capacity, or the strength limit state. Serviceability is not addressed in Severe I damage and repair, so repair methods that restore some prestressing force, known as active repairs, are not necessary. Structural damage classified as Severe II damage requires structural repair to restore both the ultimate capacity and the service limit state, meaning that prestress force needs to be restored with the repair method. Severe III damage is too extensive for practical repair, and the member must be replaced (Harries et al., 2012).

Repair Techniques

Research into different repair techniques has been performed for many years. In 1980, National Cooperative Highway Research Program (NCHRP) project 12-21 was initiated. The first phase of the project provided guidelines for assessment, inspection, and repair of damaged prestressed concrete girders (Shanafelt and Horn, 1980). A damage classification system was proposed to categorize damage into three categories: minor damage, moderate damage, and severe damage. In addition, 11 different repair techniques were developed and discussed in detail to repair severe damage, including strand splicing, external post-tensioning, steel jacketing, combinations of the repair methods, and girder replacement. The objective of the second phase of the NCHRP 12-21 project was to provide a manual for the evaluation and repair of damaged prestressed concrete girders. In addition, repair methods mentioned in the first report were tested, and further guidelines were provided (Shanafelt and Horn, 1985).

Additional repair methods have been developed since the completion of the NCHRP 12-21 project in 1985. Fiber-reinforced polymer (FRP) has emerged as a viable repair technique, both as an externally bonded sheet and as near-surface-mounted (NSM) reinforcement. Fabric-reinforced cementitious matrix (FRCM) and steel-reinforced polymer (SRP) have recently been developed as alternatives to externally bonded FRP. After a detailed literature review (Jones, 2015), three methods of repair were chosen for further study in this project: strand splicing, FRP, and FRCM.

Strand Splicing

Strand splice repairs can be used to repair prestressed concrete beams that have one or more damaged or severed prestressing strands. Splices reconnect broken strands and restore prestressing force. Strand splicing has been shown to provide a quick and efficient repair that can easily be combined with an externally bonded repair method such as FRP or FRCM.

Commercially available strand splice systems utilize a reverse thread coupler connected to threaded anchors on each end. Figure 1 shows Grabb-it™ Splice Chucks used in this project. A prestress force in the strand is introduced by turning the coupler, which moves the anchors toward each other. These splices re-tension the strand to 60-80% of the ultimate tensile strength of the undamaged strand. It is recommended to re-tension the strands to a value close to the long-term effective prestress of undamaged strands (Harries et al., 2012). Research has shown that splices restore 85-96% of the original tensile strength of the strand (Zobel et al., 1997).

Figure 1. Installation of Splice Chucks

Ensuring that the strands are re-tensioned to the proper value is important. Calibrating the amount of tension restored can be based on the torque-wrench method or the turn-of-the-nut method. The torque-wrench method involves setting a torque wrench to a specified torque value and converting that to a prestress force. Though this method is an easy way to measure the prestress force applied, it can prove to be an inaccurate calibration of the re-tensioning force because of the influence of friction in the coupler and anchor system (Labia, 1996). The turn-of-the-nut method uses the displacement between the splice chucks on each end of the coupler to measure stress. This measures the change in length of the strand, which can then be converted to strain, by assuming a stiffness of the strand and the chucks, and ultimately the applied stress.

Geometry of the beam is an important consideration for strand splice repairs. Splice chucks have a diameter of up to 1.625 in, and strands may be too closely spaced to accommodate splices on adjacent strands. This means that longitudinally staggering the splices of adjacent strands is important to ensure that all of the strand splices in a repair fit together. Each strand splice repair requires removal of the concrete cover around the strand for 24 to 30 in of length so that the coupler and splice chucks can fit in place. For strand splice repairs on the bottom row of strands in a girder, the reduced amount of concrete cover over the splice chucks may be an issue in terms of long term durability.

Strand splicing has been shown to be an effective way to restore original beam strength. Zobel et al. (1997) provided the following recommendations for the use of strand splice repairs: a) when the ultimate flexural strength of the beam with the remaining undamaged strands is greater than the factored design moment; b) when fatigue is not a major concern; and c) when repairs consist of less than 10-15% of the total number of strands in the beam.

Fiber-Reinforced Polymer (FRP) Composites

FRP materials are a novel repair material that has been proven a viable alternative to traditional repair methods for reinforced concrete, masonry, and prestressed concrete structural elements. FRP is comprised of fibers embedded into a polymeric resin matrix. As a system, the resin protects and transfers the load to the fibers. Typical fibers used in structural applications are made from glass, carbon, and aramid where the purpose of the fibers is to carry the load and

give the system high tensile strength and rigidity in the longitudinal direction. FRP composites are inherently isotropic, as they exhibit excellent tensile strength in the direction of the fibers and relatively low strength in the transverse direction of the fibers. FRP composite systems exhibit elastic behavior up to failure and do not experience yielding. Material properties include low to high modulus of elasticity values, depending upon the fiber and the resin in the composite. FRP materials are resistant to corrosion and exhibit good weathering durability performance compared to other construction materials.

FRP technology tailored to reinforced concrete repair was first introduced in the early 1990s (Nanni, 1997) and since then has become increasingly common because of the many studies that have been conducted and reported to understand better the properties of FRP systems and their optimal uses. FRP as a repair technique has been proven structurally efficient in restoring stiffness and strength to damaged bridge beams (Di Ludovico et al., 2005). The great success of using FRP composites in repair and rehabilitation of concrete structures was driven by their high strength-to-weight ratio (lightweight), high tensile strength, and anti-corrosive properties.

ACI 440.2R-08, *Guide for the Design and Construction of Externally Bonded FRP Systems for Strengthening Concrete Structures* (ACI 440.2R, 2008) provides current design criteria for the design and construction of externally bonded FRP systems specifically for concrete. The document covers all components necessary for effective FRP design and construction applications: material properties, recommended construction requirements, design recommendations, and design examples. Recently, the American Association of State Highway and Transportation Officials (AASHTO) published guidelines for the strengthening repair of reinforced concrete structures and components using FRP Composites in *Guide Specifications for Design of Bonded FRP Systems for Repair and Strengthening of Concrete Bridge Elements* (FRPS-1). This document was published in 2012 and is built from ACI 440.2R-08. The AASHTO FRPS-1 document is of great importance and is a breakthrough for bridge strengthening and repair using composites.

Fabric-Reinforced Cementitious Matrix (FRCM) Composites

FRCM has recently emerged as an attractive repair and strengthening material because of its inherent heat resistance and compatibility with the concrete substrate (for example, it can be applied on a wet surface and allows vapor permeability). FRCM systems consist of one or more layers of dry fabrics made of carbon, glass, aramid, or polyparaphenylene benzobisoxazole (PBO) that are sandwiched between layers of cementitious mortars (Figure 2). The term "dry fabrics" stems from the fact that the fibers are not fully impregnated by the cementitious matrix, contrary to FRP systems. Fabrics are produced with various window sizes and their light weight, high tensile strength, and ease of application makes the system appealing. The cement-based matrix exhibits high compressive strength, but low tensile strength, as well as protecting and transferring the load to the fibers. Therefore, the fibers are the primary tensile load carrying mechanism. Even though some interesting field applications have been reported that justify FRCM as a potential strengthening technology (Nanni 2012), experimental and theoretical research is still needed to fully characterize FRCM and quantify its mechanical effectiveness.
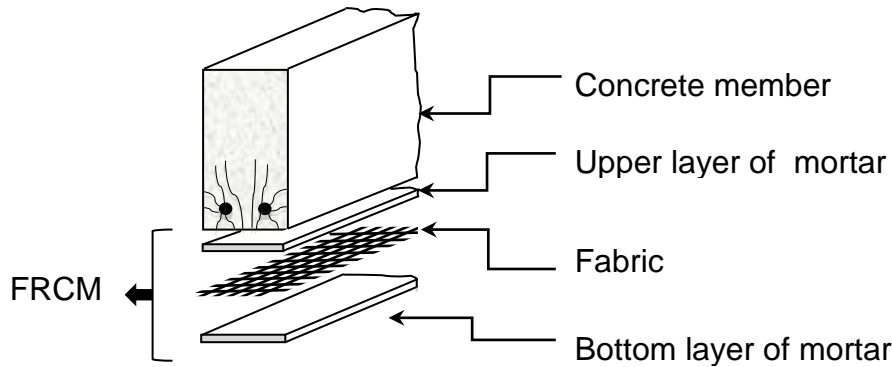
Figure 2. Schematic Representation of FRCM for Strengthening Concrete Structures

The current criteria used to evaluate, characterize, and approve FRCM composite systems for strengthening existing masonry and concrete structures, AC434 – *Acceptance Criteria for Masonry and Concrete Strengthening Using Fabric-Reinforced Cementitious Matrix (FRCM) Composite Systems*, was developed by the International Code Council Evaluation Service (ICC-ES, 2013b). It covers all standards and test procedures required to evaluate FRCM products for code compliance. Similarly, the current design and construction guidelines for FRCM systems, ACI 549.4R-13 – *Guide to Design and Construction of Externally Bonded Fabric Reinforced Cementitious Matrix (FRCM) Systems for Repair and Strengthening Concrete and Masonry Structures*, was developed by the American Concrete Institute (ACI Committee 549, 2013). This document also contains necessary guidance for effective design and construction of FRCM systems: material properties, system qualifications, installation guidelines, design considerations for reinforced concrete or masonry substrates, reinforcement details, and design examples.

Opportunity

In the spring of 2013, the bridge carrying Rt 614, Arcadia Road, over I-81 at Arcadia was demolished and replaced with a new bridge. The primary motivation for the replacement was the damage to the beams over the southbound lanes caused by impact from over-height vehicles. The new bridge provides additional clearance so impacts should no longer be a problem. The deck was saw-cut and the beams removed essentially intact. Four of these beams were delivered to the Virginia Tech Murray Structural Engineering Laboratory for testing. This provided an excellent opportunity to test repair techniques on full-scale bridge beams, without the cost associated with fabrication of new beams.

PURPOSE AND SCOPE

Objectives

The primary objective of this project was to develop recommendations to VDOT for the evaluation and repair of impact damaged prestressed bridge beams. This was to be accomplished by completing the following work plan:

1. Repair and test four beams from the Arcadia Rd overpass – Three repair techniques were investigated: strand splices, FRP layups and FRCM. One beam was tested in its undamaged condition, while the other three beams were intentionally damaged, repaired, and tested to determine if the repair technique could return the beam to its original strength.

2. Characterize material properties of beams and repairs – All materials in the original beams and in the repairs were tested to determine basic material properties.

3. Determine best practices for modeling repaired beams – Several methods for calculating strength and behavior of the tested beams were evaluated to determine the best practices for calculation of original and repaired strength and load-deflection behavior. These methods included the AASHTO LRFD Bridge Design Specifications methods (AASHTO, 2010), a conventional strain compatibility approach, two-dimensional non-linear beam models using OpenSees^{TM} software, and three-dimensional non-linear finite element models using LS-DYNA^{TM} software.

4. Extrapolate from laboratory tests to in-situ beam evaluations – The beams extracted from the Arcadia Bridge were unusual because only a narrow section of the bridge deck was left attached to the top flange of each beam. To better understand the behavior of in-situ beams with a wider effective top flange width, the best practices for modeling determined in Task 3 were used to calculate strength and behavior of a more realistic set of bridge beams with tributary composite deck area.

5. Provide recommendations on repair of impact-damaged beams – Based on all testing and analysis performed in this project, recommendations are made for evaluating and repairing impact-damaged prestressed concrete bridge beams.

SCOPE

As mentioned earlier, three repair methods were investigated in this project: strand splicing, FRP and FRCM. Other types of repairs were beyond the scope of this project.

METHODS

This section presents the methods used for damage, repair and testing of the four beams extracted from the Arcadia overpass. Methods for material property characterization are also presented. Fundamental material property testing was performed at the University of Miami, and tests of materials from the original beams and the beam repairs were performed at Virginia Tech. Methods used for analysis of the tested beams are also presented in this section.

Description of Available Beams

Four AASHTO Type III beams were extracted from the Arcadia overpass. The beams were 60 ft long, and each had 50 prestressed strands, which included two straight strands in the top flange, 40 straight strands in the bottom flange, and eight harped strands. The harping points were located at 24 ft from each end of the beam. Cross sections of the beam between the harping points and near the end of the beam are shown in Figure 3. Each prestressing strand had a nominal diameter of 0.375 in, with a cross-sectional area of 0.080 in^2. Seven-wire stress-relieved strand with a minimum ultimate tensile strength of 250 ksi was used in the beams,.
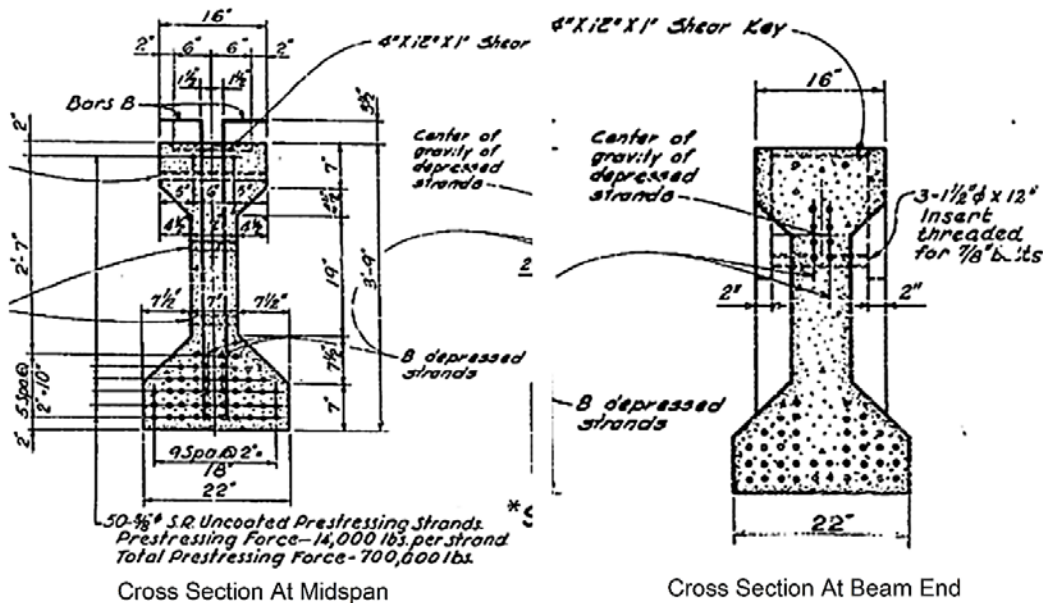

Figure 3. Cross Section of a Beam (VDOH, 1957)

In the Arcadia overpass, a composite concrete deck was placed above the beams. The composite deck spanned between the beams, which were spaced 7 ft- 4 in center to center. The beams were removed from the bridge by saw cutting through the deck, and removing most of the width of the composite deck. A narrow section of the deck was left attached to each beam. The deck width varied for each beam, and though relatively constant, varied along the length of each beam. A cross section of a beam with deck concrete is shown in Figure 4. Shear reinforcement consisted of two No. 5 single leg stirrups, with variable spacing along each girder as shown in Figure 5. Figure 5 also shows the center of gravity of the harped prestressing strands.

Table 1 presents a summary of the four beams. They are designated A through D. Beam A was the exterior beam on the north side of the span crossing the south bound lanes of I-81. It had been previously struck and damaged by over height vehicles, and had been repaired with splice chucks and patch mortar. As a result of the damage, the beam broke into two pieces during extraction and handling. One was 44 ft long, and this was tested as the control beam. The shorter piece of the beam was used to extract concrete, reinforcing steel and prestressing steel samples for testing to determine material properties. Beam B was damaged and repaired in one location, at mid-span. Eight strands were severed and the beam was repaired using splice chucks and patch mortar. Beam C was damaged and tested at two locations, at the third points.

Four strands were severed at each location, and one location was repaired with splice chucks, while the other was repaired with FRP. Finally, Beam D was also damaged in two locations, at the third points. Four strands were severed at each location, and one location was repaired with FRCM, while the other was repaired with both splice chucks and FRCM. Detailed descriptions of the damage and repair techniques and testing protocols are presented later in this section.
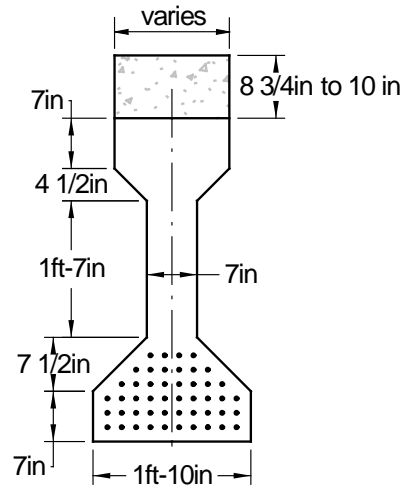
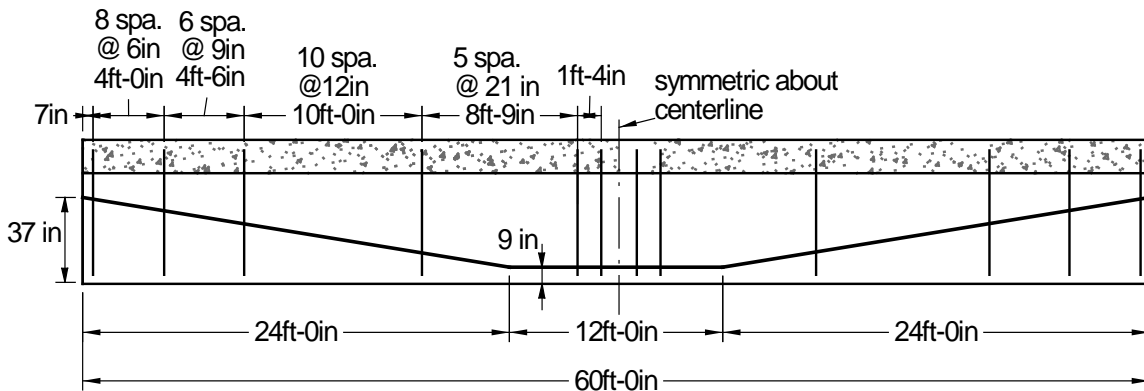

Figure 4. Cross Section with Existing Deck

Figure 5. Cross Section with Stirrup Layout and Harped Strand Pattern.

Material Property Characterization

Beam Materials

To accurately model and assess behavior, materials tests were conducted on the beam concrete, the deck concrete, the prestressing strands, the shear reinforcing bars, and the repair materials. Material tests were each performed in accordance with the proper standard set by the American Society for Testing and Materials (ASTM).

Deck and Beam Concrete

Core samples of the beam concrete and the deck concrete were taken from the unused section of Beam A using a concrete core drill. Cylinder samples were 2.75 in in diameter and

approximately 6 in long. Two cylinders from the beam concrete and two cylinders from the deck concrete were obtained and tested for compressive strength in accordance with ASTM C42. Two additional core sample cylinders were taken from the beam and tested for splitting tensile strength in accordance with ASTM C96.

Table 1. Summary of Beams, Damage and Repair

Beam	Length	Test No.	No. Severed Strands	Description of Repair
A	44 ft	1	0	Control Test
B	60 ft	2	8	Strands Spliced
C	60 ft	3	4	FRP
		4	4	Strands Spliced
D	60 ft	5	4	FRCM
		6	4	Strands Spliced and FRCM

Reinforcing Steel

Two steel reinforcing bars were extracted from the unused portion of Beam A and tested in tension for yield strength and ultimate strength. The 3-ft long bars were gripped with the hydraulic V-Grips of the SATEC universal test machine. An internal extensometer, an internal load cell, an external wire pot, and a 2-in clip-on extensometer were used to measure the load and the displacement of the bars during testing.

Prestressing Steel

Prestressing strands were tested in tension to develop an accurate stress-strain curve and find the ultimate tensile strength. According to the bridge plans, the prestressing strands used were stress-relieved strands with a minimum ultimate tensile strength of 250 ksi. Two strand samples were extracted from the unused section of Beam A and prepared for testing using the procedures developed by Loflin (2008). The strands were tested in the SATEC universal machine. Hydraulic V-grips were used to grip copper tubing bonded with epoxy around the ends of the strands, and load and displacement sensors internal to the SATEC universal testing machine, an external wire pot, and an external extensometer were used to measure the load and the displacement of the strand.

Fiber-Reinforced Polymer (FRP)

Two FRP systems were evaluated for this project: C200H and C400H fibers, both using the same resin. C200H is a high-strength unidirectional carbon fiber sheet made from carbon fibers with a minimum nominal fiber density of 600 gsm (grams per square meter, or g/m^2). C400H is a high-strength unidirectional carbon fiber sheet made from carbon fibers with a minimum nominal fiber density of 1,350 gsm. The two types of carbon sheets are shown in Figure 6.

FRP Preparation and Installation

Mechanical mixing of the saturating resin was implemented following the manufacturer's specifications, whereby the two-part resin was mixed completely until a smooth, uniform streak-

free consistency was reached. Part A and Part B of the epoxy resin were mixed according to the mixing ratio suggested by the manufacturer's instructions: 100 part A to 33 part B by weight.
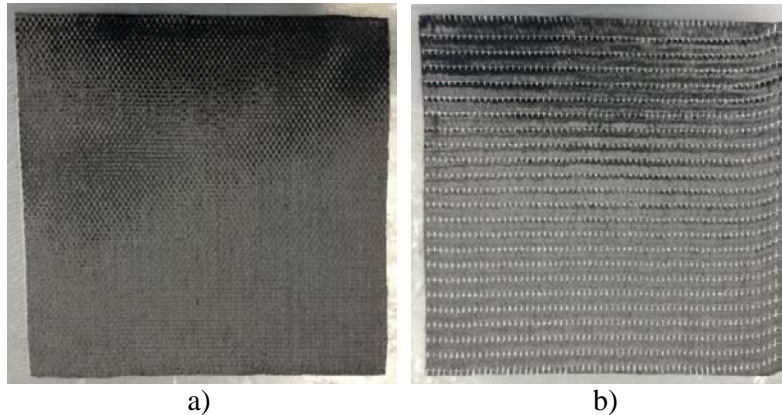

a)   b)
Figure 6. FRP Material Constituents: a) C200H b) C400H

The following steps were taken in the specimen preparation:

Step 1: Fiber pre-impregnation setup: The fiber sheet roll under evaluation is set up for saturation on the pre-impregnation frame following the manufacturer's specifications and using recommended equipment.

Step 2: Fiber sheet cutting: Individual pieces of fiber sheet roll are cut to fabricate.

Step 3: Resin mix and fiber impregnation: The designated saturating epoxy resin is mixed using mechanical means and poured into the reservoir of the frame. The fiber roll is fed through the resin bath in the frame to saturate the fiber.

Step 4: CFRP panel fabrication: Discrete pieces of the fiber sheet are placed on non-stick sheets on a flat surface. Another non-stick sheet is used to sandwich the CFRP panel to ensure a flat panel is produced. A plastic trowel is then used to remove excess resin (see Figure 7). Panels were left to cure for a minimum of: a) 24 hours before removing the non-stick sheets and b) 72 hours prior to testing.

A wide variety of tests were performed on the FRP repair materials at the University of Miami. All test results can be found in Pino and Nanni (2015). Only the Direct Tension test is directly related to the laboratory beam tests, and so is presented herein.

Direct Tension

This test is to determine the tensile properties in the fiber direction for the FRP systems under evaluation as a benchmark (without any aging or environmental exposure). Average properties include tensile chord modulus of elasticity, ultimate tensile stress and ultimate tensile strain (elongation). Tensile coupons were tested according to AC125, Section 5.8, Table 3 of *Physical and Mechanical Properties of FRP Composite Materials* (ICC-ES 2013a) and reference

standard ASTM D3039/D3039M – 08, *Standard Test Method for Tensile Properties of Polymer Matrix Composite Materials*.

Figure 7. FRP Panel Fabrication

In total, 20 coupons were prepared: five continuous one-ply C200H samples, five continuous one-ply C400H samples, five continuous two-ply C200H samples, and five continuous two-ply C400H samples. Nominal specimen dimensions were 10 in long by 1 in wide with the thickness based on type and number of plies.

Specimens were obtained from 12-in square FRP panels. The specimens were cut to the prescribed dimensions using a high-precision diamond blade saw from different randomly selected panels. Tabs were installed as indicated in ASTM D3039 (2008) after sanding the ends of the coupon specimens. Uniaxial tensile load was applied to all specimens. Testing for the specimens was performed using a hydraulic universal test frame with a maximum capacity of 55 kips. Tensile load was measured with the internal load cell of each frame, while the elongation of the specimen was measured using a clip-on extensometer with a 2.0-in gauge length, placed at mid-length of the coupon specimen. The extensometer was removed at 50% of the expected tensile strength during the test to avoid damage of the instrument. Specimens were gripped with hydraulic wedge grips.

Fabric-Reinforced Cementitious Matrix (FRCM)

The FRCM system used in this project consists of two main elements: the mesh and the mortar. The mesh is comprised of PBO fiber fabric with an unbalanced network made of 0.394-in and 0.747-in spaced fiber rovings. The free space between rovings is roughly 0.197 in and 0.591 in, respectively, and the nominal thickness in the two fiber directions is 0.0018 in in the primary direction and 0.0004 in in the secondary direction (see Figure 8). The mortar is a stabilized inorganic cementitious matrix used for concrete flexural and shearing stress reinforcement.

FRCM Preparation and Installation

The inorganic matrix product is a prepackaged proprietary mortar prepared by mechanical mixing, since hand mixing is not suggested by the manufacturer. The preparation initiates by adding the dry powder cementitious matrix to 90% of the water needed for the mix.

Mixing continues for at least 3 minutes until a homogeneous matrix paste is formed. If necessary, the remaining 10% water is mixed for an additional 2 minutes. Upon completion, the mortar rests for 2 minutes before being applied to the substrate surface. The matrix-to-water ratio used for the preparation of the product was 1.59 gal of water to 55.12 lbs material for this mortar.
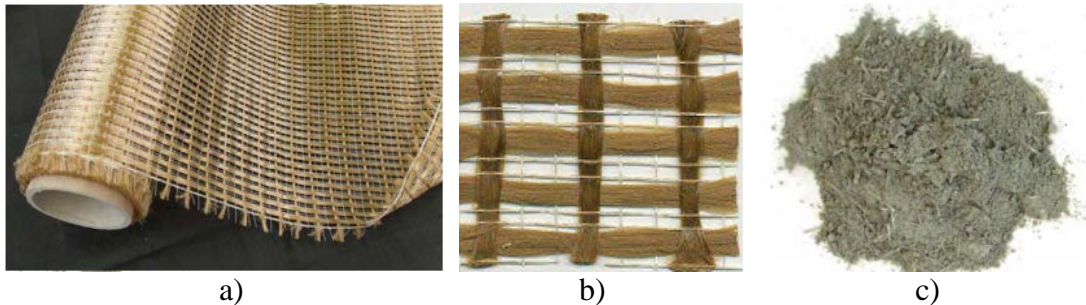

a)   b)   c)

Figure 8. FRCM Material Constituents a) Mesh Fabric Roll b) Mesh Fabric Grid c) Mortar

Preparation of the specimens required the following steps:

Step 1: Apply the first layer of matrix with a trowel on the structure surface with a thickness of 0.12 to 0.16 in (see Figure 9a).

Step 2: Lay the pre-cut fiber mesh with the appropriate fiber orientation on top of the first matrix layer and press lightly with bottom of trowel to embed the fabric in the matrix. (Figure 9b).

Step 3: Add a second layer of the matrix with the trowel to cover the fiber mesh with a thickness of 0.12 to 0.16 in to create a sandwich. (Figure 9c).

Step 4: For multiple layers, repeat steps 2 and 3 until desired number of layers is reached.

Other Specifications: An overlap of 4.75 in was used when joining fiber meshes together when applicable. The product must be applied at an environmental temperature range between 41ºF and 95ºF as specified by the manufacturer.

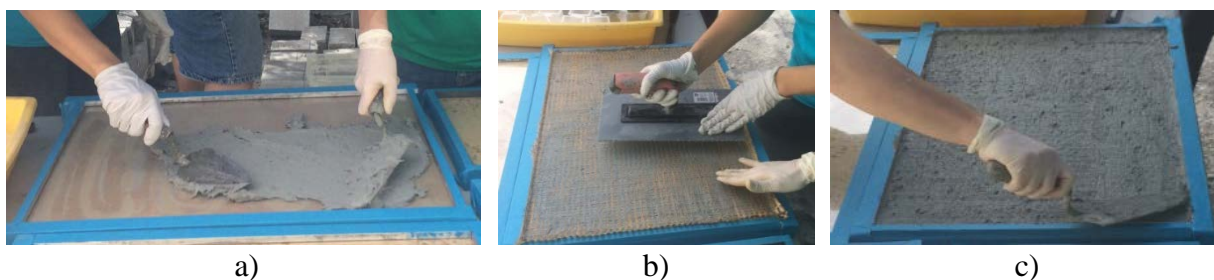a)   b)   c)

Figure 9. Specimen Preparation a) First Layer of Mortar b) Placing Mesh c) Layer of Mortar (Sandwich)

A wide variety of tests were performed to characterize the material behavior of the FRCM. These tests were performed at the University of Miami, and complete results can be found in Pino and Nanni (2015). In this report, only results that are pertinent to the lab tests are

12

presented. Several of the tests were repeated for the actual repair materials applied to the laboratory test beams.

Compressive Strength of Matrix Mortar

This test is to evaluate the compressive strength of the mortar used for FRCM strengthening application per AC434 Section 4.3 (ICC-ES, 2013b) and reference standard ASTM C109/C109M (2013). In the Miami lab, ten 2-in cube samples were cast in cube molds per ASTM C109. Immediately upon completion of molding, the mold was placed in a moist room for curing for 24 hours. Specimens were removed from the molds after the first day of curing and five samples were exposed to a limewater conditioning environment for each of two curing durations: 7 days and 28 days. Uniaxial compression load was applied to the cube specimens using a screw-type universal test frame.

Compressive Strength of Repair Mortar

This test is to evaluate the compressive strength of repair mortar used for concrete substrate repair prior to application of FRCM strengthening systems. Tests are performed per AC434 Section 4.3 (ICC-ES, 2013b) and reference standard ASTM C109/C109M (2013). Ten 2-in cube samples were cast in cube molds per ASTM C109. Immediately upon completion of molding, the mold was placed in a moist room for curing for 24 hours. Specimens were removed from the molds after the first day of curing and five samples were exposed to a limewater conditioning environment for each of two curing durations: 7 days and 28 days. Uniaxial compression load was applied to the cube specimens using a screw type universal test frame.

For the repairs performed on the laboratory beams by Structural Technologies in July 2014 and March 2015, 4-in diameter cylinder samples were taken for the repair mortar and tested for ultimate compressive strength. Tests were performed in a Forney compression test machine at 24 hours, 48 hours and 7 days of age.

Direct Tension

This test is to determine tensile strength, elongation, and modulus of elasticity of the FRCM strengthening composite system using coupons under ambient conditions. Tensile coupons were tested according to AC434, Section 4.2.3 - Tensile Strength and Annex A - Tensile Testing of FRCM Composite Specimens (ICC-ES, 2013b). In total, 15 coupons were prepared: five continuous one-ply samples, five continuous two-ply samples, and five lapped one-ply samples.

Panels were allowed to cure for 28 days before coupons were cut with a circular diamond blade saw from larger FRCM material panels. Continuous and lap single ply rectangular coupons had dimensions of 16×2×0.4 in. Continuous two-ply rectangular coupons had dimensions of 16×2×0.55 in. Fiber alignment was set in the 0° direction along the length of the coupon. Lap tensile strength coupon specimens were made following the same methodology, with the difference of a nominal mesh overlap length of 4.72 in.

Steel metal tabs with clevis openings were bonded to each end of the specimen with Loctite PL[TM] Premium Polyurethane Construction Adhesive. The tab lengths were 6 in for one-ply and two-ply continuous tensile coupons and 4 in for the single ply lap tensile coupons. The glue cured for at least 24 hours prior to testing.

All specimens were conditioned prior testing under laboratory ambient conditions at room temperature $73 \pm 6°F$ and $60 \pm 5\%$ relative humidity, for at least 28 days. Uniaxial tension load was applied to the tensile coupons. Testing was performed using a screw-driven Instron Universal Test Frame with a maximum capacity of 30 kips. Axial deformation was measured using a clip-on extensometer with a 4-in gauge length, placed mid-length of the specimen. The gripping mechanism was a clevis-type connection on one end and a double-clevis connection on the other end (see Figure 10).
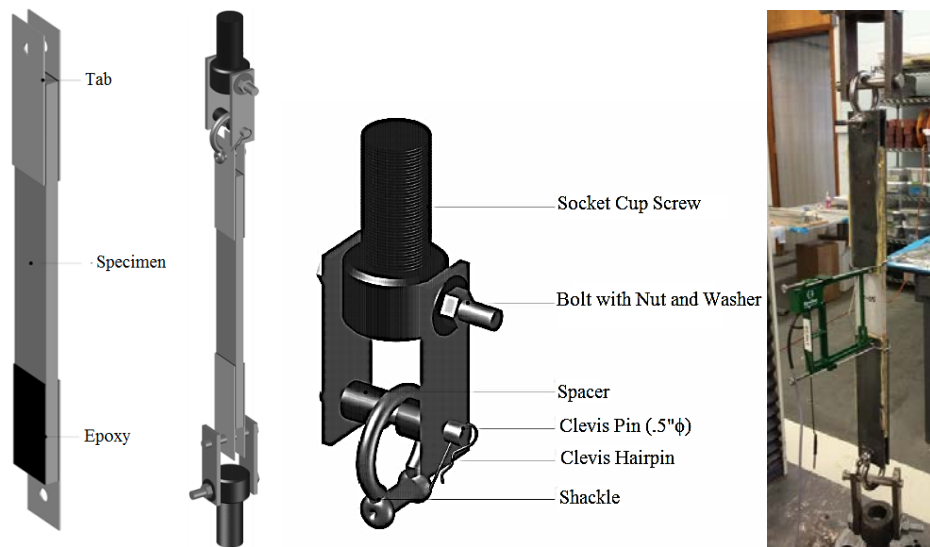

Figure 10. Specimen Test Setup with Clevis Grips and Extensometer

Early Age Compressive Strength

In addition to the 28 day tests, tests were performed to determine the early age development of compressive strength of the matrix mortar under ambient conditions. A total of 40 specimens were tested, five each at eight ages: 1, 2, 3, 7, 14, 21 and 28 days.

Splice Chucks

Tension tests of the splice device were conducted in the lab. Prestressing strands were anchored between two steel abutments that were in turn anchored to the strong floor. A strand was anchored at each of the abutments with reusable chucks, and between the abutments, a strand splice connected the two strand segments. The abutments were placed 16 ft apart for the first test, 6 ft apart for the second test, and 4 ft apart for the third test. A load cell was placed between the abutment and the chuck at one end, and a center-pull hydraulic ram was placed between the abutment and the chuck at the other end. The splice was tightened using a calibrated

torque wrench and load cell readings were taken at specified torque values to compare to the theoretical values given by the manufacturer in Table 2. After completing the torque test, the strands were loaded to failure with the hydraulic ram. In all tests, the strands failed before the splice chuck.

Table 2. Suggested Installation Torque (after Prestress Supply Incorporated 2010)

Grade	Prestressing Strand			Splice Chuck Torque Values	
	Strand Dia. in	80% of Ultimate, lbs	Ultimate Strength, lbs	in-lb	ft-lb
	3/8	16,000	20,000	1800	150
250	7/16	21,600	27,000	2430	203
	1/2	28,800	36,000	3240	270
	3/8	18,400	23,000	2070	173
270	7/16	24,800	31,000	2790	233
	1/2	33,000	41,300	3710	309

Effective Prestress

Tests were conducted to determine the effective prestress of the strands in Beam D. Eight strands needed to be severed as part of the damage process. Six of these strands were monitored during cutting to evaluate effective prestress. The strands were cut with an electric grinder with a steel-cutting blade, as shown in Figure 11a, and an extensometer was used to measure the change in length of the strand when cut, as shown in Figure 11b. Wire ties were utilized to reduce vibration and help to keep the strand in place as it was being cut, and duct tape was placed near the location of the saw cut to prevent unraveling of the strand.

a)   b)

Figure 11. a) Electric Grinder Cutting a Strand, b) Extensometer to Measure Length Change

Damage and Repair Methods

Beam A

As mentioned previously, Beam A was broken into two pieces during demolition of the Arcadia overpass. The two sections were separated from each other by cutting the prestressing strands. The 44-ft piece was tested in its existing condition, with no additional damage or repair.

15

Beam B

      Beam B was a 60-ft long beam that was damaged at the midspan and repaired using the strand splice method. The applied damage consisted of removing 8 ft of concrete, approximately 4 ft on either side of midspan, and severing eight prestressing strands. The damage location is shown in Figure 12, and a cross section view showing the severed strands is shown in Figure 13. The length of the damage area was chosen to be 8 ft, based on the average width of a semi-trailer (YRC Worldwide, 2015). To damage the girder, it was set on its side and struck with a hydraulic hammer attached to a backhoe, as shown in Figure 14a. After the rough damage was inflicted by the jack hammer, the edges of the repair area were saw cut to a depth of at least 1.0 in to create a defined edge to the repair area. Additional concrete was chipped out from around exposed strands to allow for placement of the splice chucks and to create space for the repair mortar to flow around the strands (see Figure 14b).
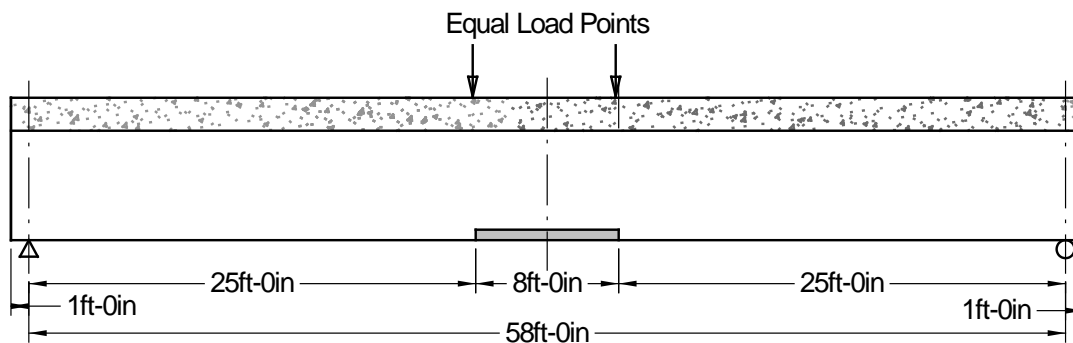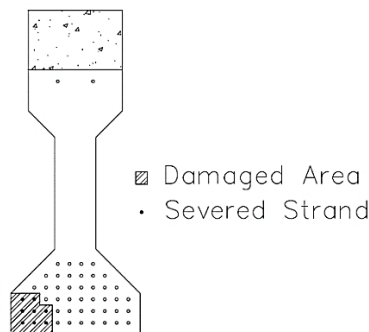

Figure 12. Beam B Damage Location

Figure 13. Beam B Damage Cross Section with Eight Strands Severed

      Eight strands were severed and re-tensioned to represent significant enough damage that girder replacement might be considered. The amount of prestressing force loss in a girder that requires replacement varies by state. Some state departments of transportation will replace a girder if any strands are damaged. Other departments of transportation will replace a girder if 10% of the strands are damaged, whereas some state departments of transportation will consider repair methods if less than 25% of strands are damaged (Wipf et al., 2004). Ignoring the two top strands, severing of eight strands, or 17% of the strands, was chosen for this test. In other beams, only four strands were severed to represent a repair of more moderate damage.

(a)   (b)

Figure 14. a) Damaging Beam B with Hydraulic Hammer b) Damage Location of Beam B Before Repair

Repair was performed by Structural Technologies. Strands were spliced and splices were tightened with a torque wrench to 80% of minimum ultimate tensile strength of the strand, based on information provided by the splice manufacturer (Prestress Supply Incorporated, 2010)(see Table 4). After the splices were installed and tightened, the damaged concrete was repaired using a high-strength, quick-cure mortar. Detailed repair procedures can be found in Jones (2015). The repair was performed in two days by three Structural Technologies workers. Figure 15, Figure 16 and Figure 17 show the progress of the repair, including installation of the strand splice, formwork for the concrete placement, and the beam after removal of the formwork.

Figure 15. Completed Installation of Strand Splices

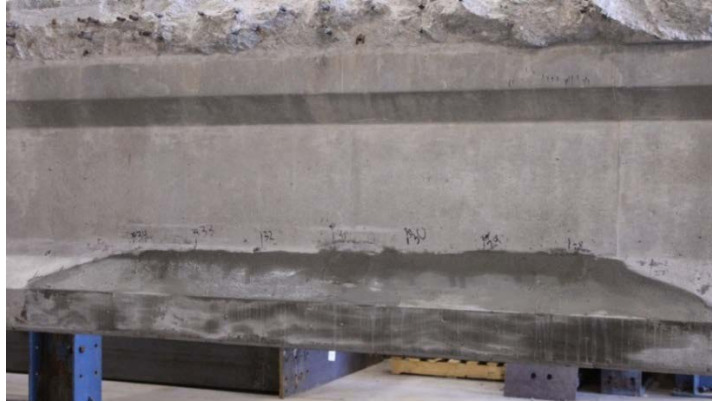**Figure 16. Formwork for Concrete Placement**

17

Figure 17. Completed Repair after Form Removal

Beam C

Beam C, a 60-ft Beam, was damaged for approximately 4 ft of length at the one-third and two-thirds points along the length of the girder. Four of the 48 prestressed strands in the bottom flange of the beam were severed at each of the two damage locations. Having two damage locations on one beam allowed two different repair techniques to be tested on the same beam. Damage to each repair location was limited to 4 ft of damage to ensure that one repair would not influence the results of the other repair. Figure 18 shows the damage locations along the length of the girder, and Figure 19 shows a cross section at the damage locations. At each location, two strands were severed in the bottom row of strands, one strand was severed in the second row from the bottom, and one strand was severed in the third row from the bottom. To damage the girder, it was set on its side and struck with a hydraulic hammer attached to a backhoe. The damaged area was then prepared by saw cutting the edges and chipping around strands as was done for beam B.
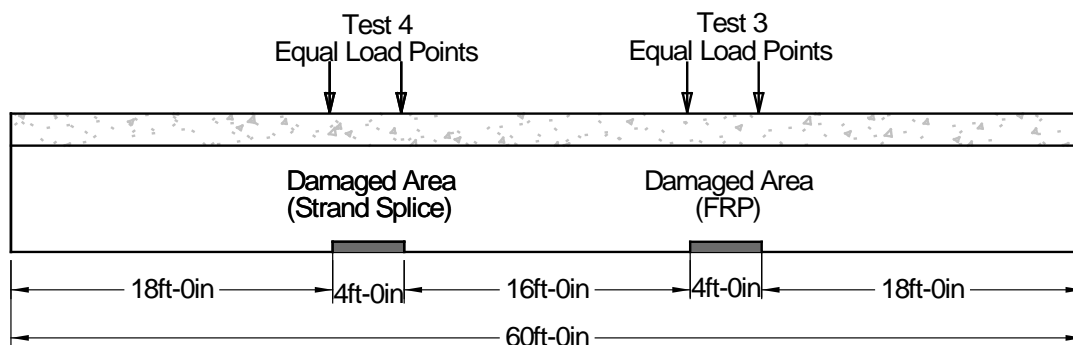

Figure 18. Beam C Damage Locations

This repair was also performed by Structural Technologies. At the first location, strands were spliced and splices were tightened with a torque wrench to 80% of the minimum ultimate tensile strength of the strand (see Table 2). After the splices were installed and tightened, the damaged concrete was repaired in the same way as Beam B. This repair, in addition to the strand splice repair on Beam B, was performed in two days by three Structural Technologies workers. Figure 20 and Figure 21 show the progress of the repair, including the prepared repair area, installation of the strand splices and repair area after removal of formwork.
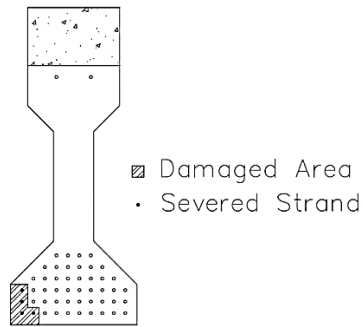
18

Figure 19. Beam C Cross Section Through Damaged Area

Figure 20. Damage Location for Test 4 Before Repair

At the other damage location on Beam C, the repair method used was FRP layup. Structural Technologies conducted the repair with a repair mortar and C400 FRP composite. C400 FRP is a 0.08-in thick fabric with an ambient-cure epoxy resin. The strands were not spliced, but were held in position using short pieces of No. 4 reinforcing bar and tie wire. The concrete patch was placed in the same fashion as the splice repairs. After the concrete patch was placed and allowed to cure for at least 12 hours, the FRP was installed.

Figure 21. Completed Installation of the Strand Splices and Beam after Form Removal

While the repair mortar was curing, the sheets of fabric were cut to the appropriate length and the equipment required for installation was set up. Prior to installation of the FRP, a hammer tap test (sounding) was conducted to make sure that there was sufficient bond between the repair mortar and the original beam concrete. Next, the surface was prepared for the FRP. This included making sure there were not any raised sections or inconsistencies from the

19

formwork. In addition, corners where the fabric was going to be applied were rounded to a minimum of a 0.5-in radius. This was to ensure that there were not any locations that could result in voids, damage, or increased stress in the fabric. Because the FRP system is a contact-critical system, a grinder was then used to roughen the surface of the concrete to the aggregate level. After the surface was prepared, the resin was mixed and applied to the substrate surface as a primer. After the primer was applied to the beam, a resin putty mixture was applied to fill in any voids on the surface of the girder and create as smooth a surface as possible to which the fabric would bond (See Figure 22).

Figure 22. Spreading Putty over Area of Beam to be Repaired

The fabric sheets were pulled through the epoxy and rolled through a press to ensure that the epoxy sufficiently penetrated the fibers (see Figure 23). The saturated fabric was then stretched along the length of the repair section and a ribbed roller was pressed against it to help it to bond with the putty (see Figure 23).

Figure 23. Fiber-Reinforced Polymer Saturation Process and Rolling of FRP Fabric to Ensure Bond to Concrete

After the first layer of fabric was installed, an additional layer of putty was spread across the sheet and the second layer of fabric was saturated, pressed, and rolled onto the bottom of the beam. This resulted in the primary longitudinal fabric being two layers of C400 FRP, each 16 ft long. A third layer of putty was applied and FRP sheets were saturated and installed in the transverse direction to provide confinement and enhance the bond of the longitudinal sheet to the beam. After the transverse sheets were applied, a final layer of putty was spread across them and leveled to provide a clean and smooth outer surface that was free of abnormalities.

Beam D

Beam D, a 60-ft long girder, was damaged for approximately 4 ft of length at the one-third and two-thirds points along the length of the girder. Four of the 48 prestressed strands in the bottom flange of the girder were severed at each of the two damage locations, identical to those in Beam C (see Figure 19). Figure 24 shows the damage locations along the length of the beam. The damage was inflicted in the same way as for the previous beam. Before repairs, at least 1 in of concrete was chipped throughout the repair surface to create a clean edge to the repair (see Figure 25). At one location, strand splice chucks were used to reconnect the severed strands. At the other location, the severed strands were held in position by reconnecting them with a short length of No. 4 reinforcing bar. Both locations were then repaired with FRCM.
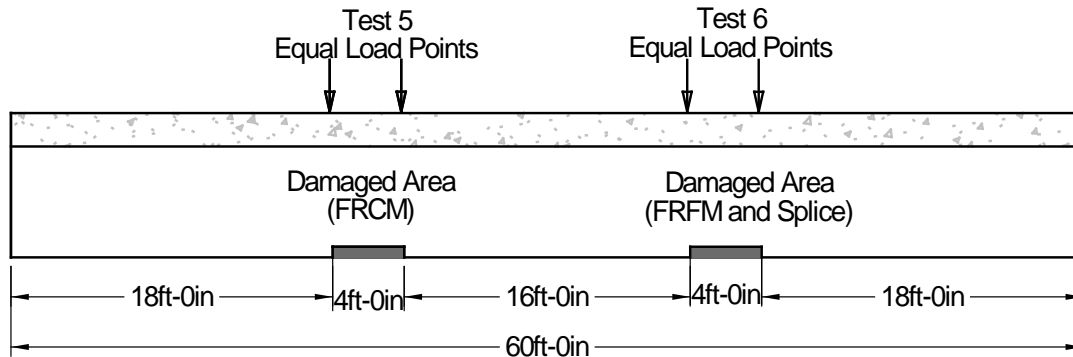

Figure 24. Beam D Damage Locations

Figure 25. Beam D after Chipping and Saw Cutting

The repairs on Beam D were also performed by Structural Technologies. The repair at both of the damage locations was done using a repair mortar, a mesh and a matrix mortar. After the concrete patch was placed and allowed to cure in the same fashion as the other repairs, the FRCM was installed. The concrete patch repair, in addition to the strand splice and patch repair in Test 6, was performed in two days by two Structural Technologies workers. Surface preparation is extremely important, and several hours were spent grinding the concrete substrate. Figure 26a shows the surface after the formwork was removed at one of the locations, and Figure 26b shows the surface after the grinding operation.

Each area of damage had the same FRCM repair. Four layers of PBO mesh were applied to the bottom flange on the bottom face and each side up to the bottom of the web. The first layer of mesh was 15 ft long, the second layer was 13 ft long, the third layer was 11 ft long, and

21

the fourth and final layer was 9 ft long. These layers were centered at the center of the damage, 20 ft from each end of the beam. The mesh was delivered on a roll, and lengths were cut and labeled prior to beginning of the repairs. The surface was wetted to a saturated surface dry condition. Before the first mesh layer, between each mesh layer and after the final layer was installed, a layer of matrix mortar was troweled on (see Figure 27). The layers of mesh were placed on the fresh mortar and pressed with a trowel to embed the mesh in the mortar (see Figure 27). A diagram of the FRCM repair sequence and mesh lengths is shown in Figure 28.

(a)   (b)

Figure 26. a) Repair Location after Formwork Removal b) Repair Location after FRCM Surface Preparation

Figure 27. Trowling Mortar over a Layer of Mesh and Pressing Mesh into Layer of Mortar
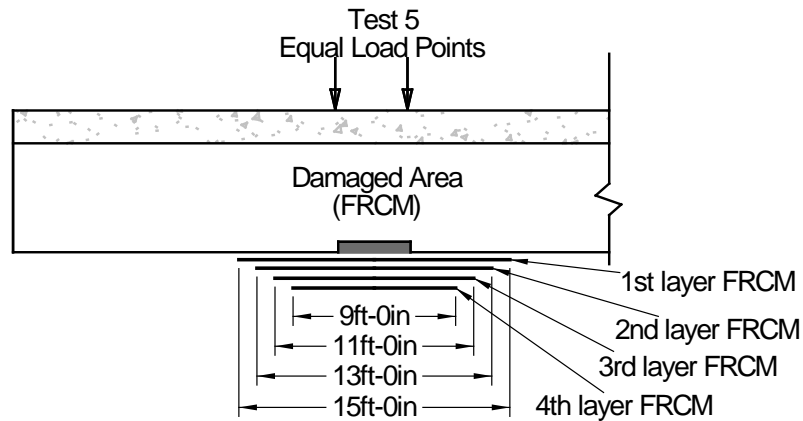

Figure 28. FRCM Repair Sequence at Both Damage Locations on Beam D

22

Laboratory Tests

Typical Test Setup

All beams were tested in a simple-span configuration with a roller support at one end and a pin support at the opposite end. Loads were applied with a 400-kip actuator and a spreader beam, so two equal loads were applied. The spreader beam was situated directly over each repaired section, to place the repair in a region of essentially constant moment. Each beam was analyzed for its test configuration to confirm a flexural failure would occur prior to a shear failure.

Typical Instrumentation

Each test had similar instrumentation. Table 3 presents the instrumentation type, measurement and calibration information. Figures 29 through 31 are photographs of the instruments used for testing.

Table 3. Instrumentation Information

Instrument	Measurement	Calibration Precision	Figure
Wire Potentiometers	beam vertical and horizontal delflection	0.001 in	29 and 30
Linear variable differential transformer (LVDT)	Slip between repair material and beam concrete and longitudinal deformation of beam	0.001 in	29 and 31
Mini linear variable differential transformer (MLVDT)	Longitudinal deformation near bottom of beam	0.001 in	30
500 kip load cell	Load applied by hydraulic actuator	200 lb	30
Bridge Diagostic Inc. (BDI) strain transducers	Longitudinal strain through depth of beam below point of applied load	1 $\mu\varepsilon$	31

a)   b)

Figure 29. Measurement of a) Displacement using Wire Potentiometers Below Load Point and b) Slip Between Beam and FRCM Repair Material Using LVDT

<center>a)   b)</center>

Figure 30. a) MLVDT, Strain Transducer, and Potentiometer and b) Load Cell, Actuator, Spreader Beam, Rubber Bearing Pads

Figure 31. LVDT and Three Strain Transducers Beneath the Load Point

Test 1

Beam A was tested as the undamaged control test to provide a baseline for comparison with subsequent tests. Beam A was approximately 44 ft in length. As mentioned earlier, it was the longer segment of a beam that had broken into two pieces. The bottom flange of the beam was spalled at the broken end for about 7 ft. To ensure that the control test would represent an undamaged beam, the section of beam from the undamaged end to 37 ft from that end was considered to be undamaged. The composite deck was cut during demolition of the bridge, but some existing deck still remained intact and attached to the girder. The existing deck on Beam A was roughly cut, with approximate dimensions 10-in deep and 24-in wide. Despite some damage to the concrete deck, it was assumed to act as fully composite. A schematic showing the loading arrangement and the location of instrumentation is presented in Figure 32.

The beam was tested on May 27, 2014 with an applied load reaching 353 kips and a deflection of 1.43 in. The load was applied in 20-kip increments, and at each load step, the load was held steady and the beam was inspected and cracks were marked. At 280 kips of applied load, the strain tranducers were removed to ensure they would not be damaged in case of failure

<center>24</center>

and, because of the potential for a failure, the beam was no longer closely inspected between load intervals. A hydraulic pump malfunctioned at 353 kips, and the test had to be stopped until the pump could be replaced. The pump was replaced, and the girder was re-tested on June 2, 2014. The load was applied in increments of 50 kips until reaching 250 kips, at which point 20-kip increments were used until reaching 401 kips. This exceeded the rated capacity of the test frame, so the test was concluded.
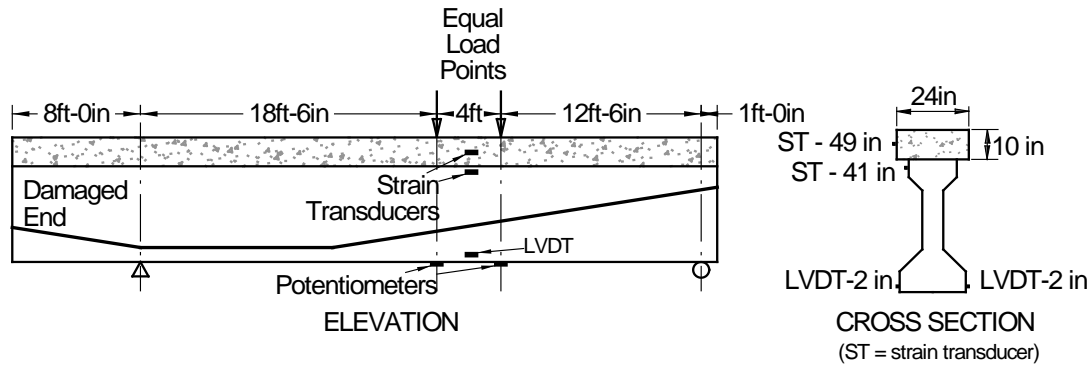

Figure 32. Test 1 Loading Arrangement and Instrumentation Layout

Test 2

Test 2 was performed on Beam B, which had eight severed strands repaired with splice chucks. Figure 33 presents the loading arrangement and instrumentation layout. Beam B was tested on August 21, 2014. At 40-kip increments to 80 kips, the load was held steady and the beam was inspected and cracks were marked. From 80 kips until 160 kips, the girder was inspected at 20-kip increments, at which point the load increment was decreased to 10 kips until failure.
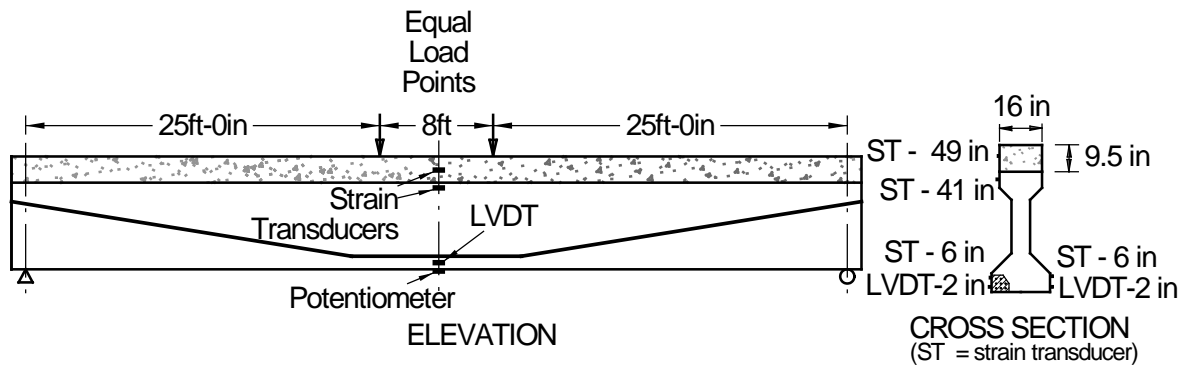

Figure 33. Test 2 Loading Arrangement and Instrumentation Layout

Test 3

Test 3 was performed on the area of Beam C that had four strands severed and was repaired with FRP layups. Figure 34 and Figure 35 present the loading arrangement and instrumentation layouts for the first and second iterations of Test 4.
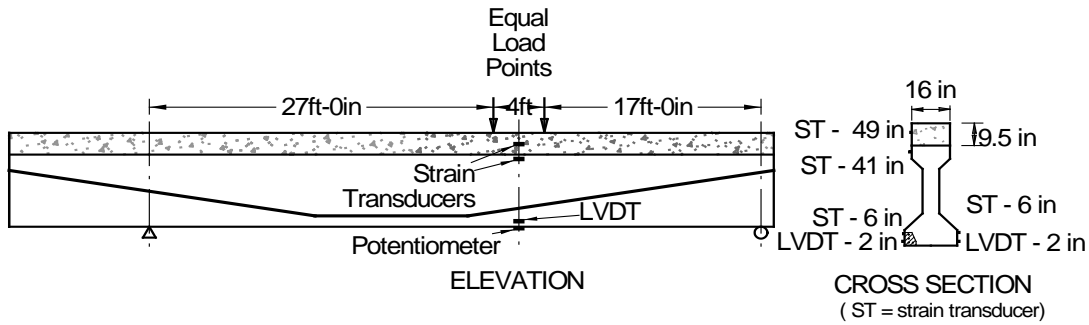
25

Figure 34. Test 3, Iteration 1 Loading Arrangement and Instrumentation Layout
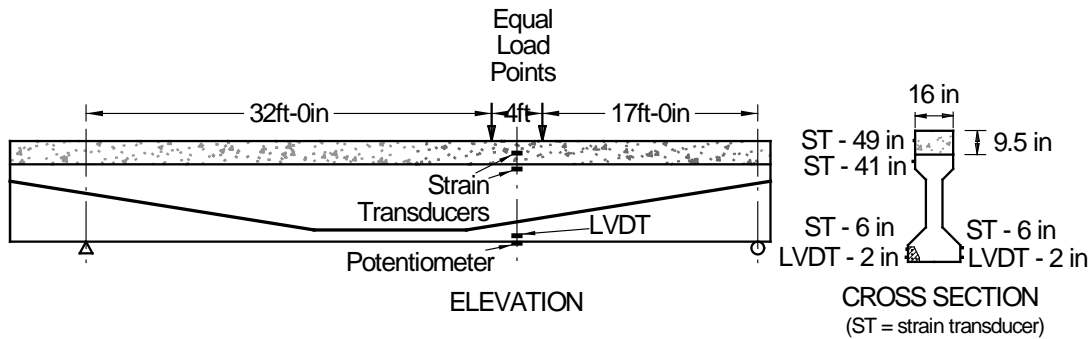

Figure 35. Test 3, Iteration 2 Loading Arrangement and Instrumentation Layout

The beam was first tested on October 21, 2014. The load was increased at approximately 20-kip increments and at each pause, the beam was inspected and cracks were highlighted and marked. After reaching 260 kips, for safety reasons, the strain transducers were removed and up-close inspection ceased. The load had been increased to 312 kips and 3.16 in of deflection when the flexural cracking approached the four-strand splice repair section to be tested in Test 4. In addition, shear cracks in the web of the girder started to form in locations with minimal shear reinforcement. In order to avoid damaging the four-strand splice repair section, propagating shear cracking, and adversely affecting the results of Test 4, the test was stopped and a second test to load the girder to failure was scheduled for after the completion of Test 4. The second iteration was conducted on December 18, 2014. At 180 kips, the actuator slipped and was no longer exerting a consistent vertical force on the girder. A frame used in the second iteration of Test 4 to hold the actuator level was used to try to keep the actuator from slipping. After the third attempt to load the girder to failure, the concrete in the constant moment region between the load points showed evidence that indicated a flexural compression failure and the test was determined to be complete.

Test 4

Test 4 was performed on the area of Beam C that had four strands severed and repaired with splice chucks. Figure 36 presents the loading arrangement and instrumentation layout for the first iteration of Test 4.
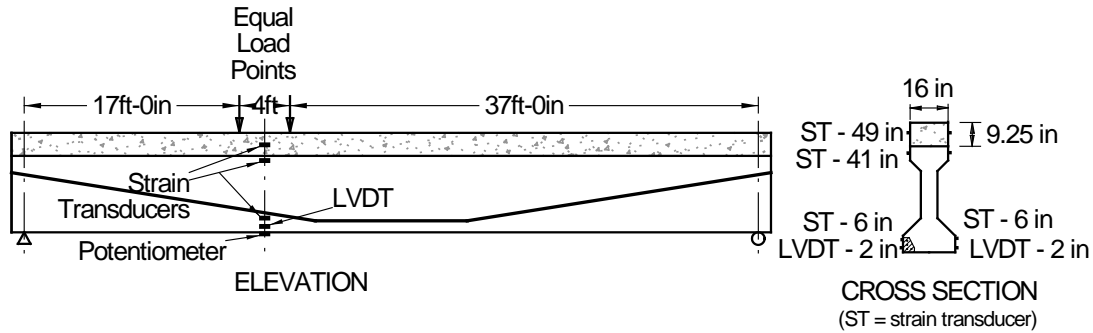
Figure 36. Test 4, Iteration 1 Loading Arrangement and Instrumentation Layout

The first iteration of Test 4 was done on November 20, 2014. At 20-kip increments until reaching 180 kips, the load was held steady and the beam was inspected and cracks were marked. After reaching 180 kips, the load increment was decreased to 10 kips. At 200 kips of applied load, for safety reasons, the beam was no longer closely inspected. The load increased to 241 kips when the actuator appeared as though it would slip out of plumb with the beam, and the test was stopped. This was caused by rotation in the beam at the points of load relative to the actuator. For the second iteration, the span length was decreased to 50 ft to reduce the rotation at the points of loading.

A second iteration of Test 4 was done on November 25, 2014 (see Figure 37). At 50-kip increments until reaching 200 kips, the load was held steady and the beam was inspected and cracks were marked. After reaching 200 kips, the load increment was decreased to 10 kips until reaching failure.

Test 5

Test 5 was performed on the area of Beam D that had four strands severed and repaired with FRCM. Figure 38 presents the loading arrangement and instrumentation layout for Test 5. An unusual aspect of this specimen was that there were saw-cut gaps in the deck from demolition of the bridge that were not filled in before the test (see Figure 39). These gaps were about 0.5-in wide across the entire width and depth of the deck and there were eight of them spaced along the length of the girder. The load was applied in 20-kip increments and the beam was examined and cracks marked at each step.
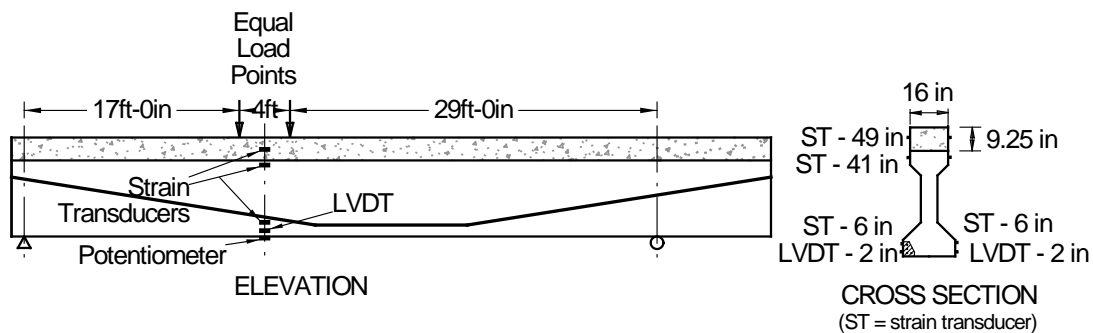

Figure 37. Test 4, Iteration 2 Loading Arrangement and Instrumentation Layout
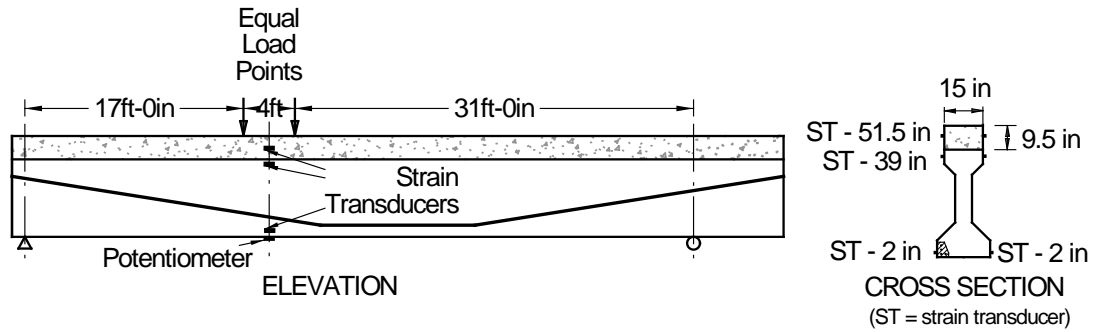
Figure 38. Test 5 Loading Arrangement and Instrumentation Layout

Figure 39. Saw-Cut Gaps in the Deck Concrete of Beam D

Test 6

Test 6 was performed on the area of Beam D that had four strands severed and repaired with both FRCM and splice chucks. Figure 40 presents the loading arrangement and instrumentation layout for Test 6. Prior to the test of this beam, the gaps in the deck, as seen in Figure 41, were filled with repair grout. The load was applied in 20-kip increments and the beam was examined and cracks marked at each step.

Figure 40. Test 6 Set-up and Instrumentation

Modeling Techniques for Tested Beams
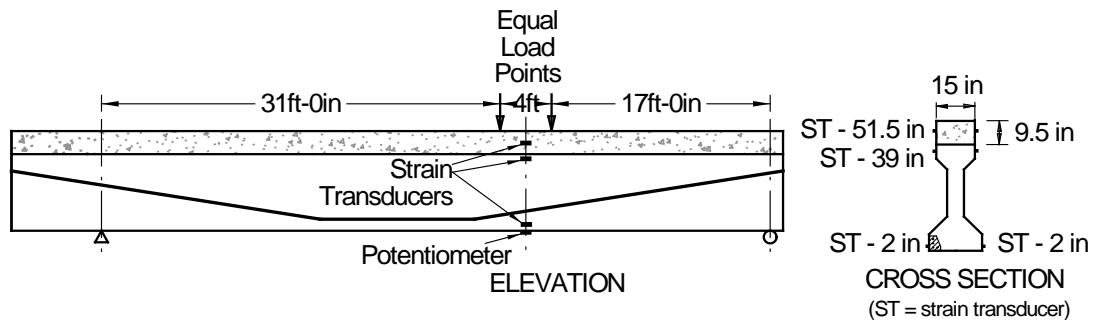
AASHTO LRFD Bridge Design Specifications

For each test, an estimate of flexural strength was made based on the AASHTO Bridge Design Specification (2010) equations. Modifications were made to account for the repairs. Cracking moments were also calculated based on AASHTO equations.

The nominal moment capacity was calculated based on tested material properties of 6,650 psi compressive strength for the concrete in the beam and 6,020 psi compressive strength for the concrete in the deck. The tensile strength of the concrete in the beam used for calculations was the tested value of 424 psi. To calculate the effective prestress force, the results of effective prestress Tests 1 and 5 were averaged; inconclusive results were obtained from the other tests. This gave an effective prestress stress of 132 ksi, which was used for all unbroken strands. For spliced strands, an effective prestress of 163 ksi, which was the tested value at an applied torque of 150 ft-lbs, was used in strength and cracking calculations. The prestressing ultimate strength for calculations was based on the tested ultimate strength of 262 ksi. The design values for the FRP composite system used in the calculations were based on the tested values for double-ply samples with the following properties: 12,100 ksi modulus of elasticity, 0.011 in/in ultimate strain, and 136 ksi ultimate tensile strength. The strength of the FRCM was based on test results as well.

In order to simulate the damage to the beam for Tests 2, 3, 4, 5 and 6, the total area of prestress strands was reduced by the number of severed strands associated with each test at the damaged area of the girder. This reduced the effective prestress force where the strands had been severed. Next, to simulate the repair, the effective strengths were added back in as an additional tensile force. For the strand splices (Tests 2, 4 and 6), the ultimate and yield stresses in the spliced strands were based on tests. During strand splice testing, the strands failed prior to the splice chucks, therefore, the calculations using tested properties assumed 100% of the ultimate and yield stresses of 262 ksi and 242 ksi, respectively.

For Test 3, the FRP was modeled as additional tensile reinforcement. To determine the location of neutral axis, the tested ultimate stress for 2-ply of 136 ksi was used in the tested material properties calculations. To calculate the effective force in the FRP at failure, the strain in the fabric was calculated by relating it proportionally to the additional strain in the prestressing strand at failure and the neutral axis depth. The tested modulus of elasticity of 12,100 ksi was used to determine the stress in the fabric and the tensile force in the calculations. For Tests 5 and 6 with the FRCM repairs, a tensile force was added at the centroid of the repair material. The force in the material was based on the expected strain at the time of concrete crushing. Example calculations are found in Liesen (2015) and Jones (2015).

Strain Compatibility Approach

To predict the complete response of the beams, a moment-curvature analysis of each beam was performed (Michael, 2010). The analysis included six points in the loading progression: 1) no applied moment, 2) decompression of concrete around strand, 3) first flexural

cracking, 4) top concrete fiber strain of 0.0015 in/in, 5) prestress strand yield strain of 0.009 in/in, and 6) top concrete fiber strain of 0.003 in/in. The strand tensile stress-strain behavior used in these calculations is given in Figure 50. The idealized stress-strain diagram was developed by Gangi (2015) and was used in the finite element modeling as a bilinear approximation of the stress-strain results obtained during the prestress strand tests. For the concrete stress versus strain relationship, the modified Hognestad model was used (Hognestad, 1956). Asymmetrical bending was not considered in these calculations. The tested properties of the strand, FRP and FRCM that were used in the LRFD analysis were also used in the strain compatibility analysis.

Analytical Models

Experimental tests like those presented in the previous sections provide unique insights about the impact of collision-induced damage and the effectiveness of retrofit techniques. Still, experimental tests must always be supplemented with analytical simulations. The analytical models allow for the evaluation of a large number of different configurations, which cannot all be tested experimentally. In this project, the experimentally tested girders failed almost exclusively by crushing in the compressive zone of the section. Such failure was induced because of the narrow deck. In in-service girders with wider decks would probably fail in the tension zone of the composite section. Thus, numerical models are necessary herein to investigate the performance of damaged and repaired girders, which includes the effect of a wider deck.

This section describes the analytical models developed for the analysis of damaged and repaired girders. Two types of models have been employed, namely, nonlinear beam models and three-dimensional, continuum-based, finite element models. The nonlinear beam models are attractive for their conceptual simplicity, computational efficiency and their capability to capture the response of flexure-dominated beams. The three-dimensional, continuum-based finite element models can capture aspects of the response in more detail, such as the confinement effect on concrete and the shear-flexure interaction in bridge girders.

Description of Nonlinear Beam Models

In the present study, the beam models are defined using the analysis program OpenSees (Mazzoni et al. 2006). The modeling approach employed is schematically summarized in Figure 41a. Specifically, the length of each girder is modeled using several beam elements, each beam element corresponding to a portion of the girder length. The harped strands in each girder are modeled with nonlinear truss elements. To ensure the compatibility between the strands and the beams at each location along the length of the girder, each nodal point of the truss elements is connected with rigid links to the corresponding nodal point of the beam element.

Sectional Model

The sectional response of the beam elements is obtained using a fiber formulation. Specifically, the cross-section is discretized into multiple fibers, as schematically shown in Figure 41b. Each fiber has an assigned area and an assigned uniaxial stress-strain law. At each

stage in an analysis, the beam model can provide the reference axial strain, ε_o, and the curvature, φ, at each section. Assuming that a beam is aligned with the x-axis and the sectional depth of the beam is aligned with the y-axis as shown in Figure 41a, the strain ε_i of each fiber "i" can be calculated using the following expression.

$$\varepsilon_i = \varepsilon_o - \varphi \cdot y \tag{1}$$

The "-" sign in Equation (1) is required when positive curvature leads to tension in the bottom fibers of a horizontal beam section.

Given the strain ε_i, the uniaxial material law assigned to the fiber "i" gives the stress σ_i of the fiber. Then, given the cross-sectional area, A_i, of each fiber, the axial force and bending moment of the section is obtained by summing the axial forces and bending moment contributions of all the fibers.

$$N = \sum_i \left(A_i \sigma_i \right) \tag{2}$$

$$M = -\sum_i \left(A_i \cdot \sigma_i \cdot y_i \right) \tag{3}$$

The approach summarized in Equations (1) through (3) can be extended in three-dimensional beam analysis. The advantage of a fiber sectional model like the one employed herein is that the axial-flexure interaction of a nonlinear girder can be naturally captured, with the provision that appropriate uniaxial stress-strain laws are used for the concrete, prestressing strands and retrofit components. The influence of the piece of deck on each girder is accounted for in the beam models by assuming that the thickness of the piece of deck is equal to 8.75 in and the width of the deck is equal to the flange width of the girder section.
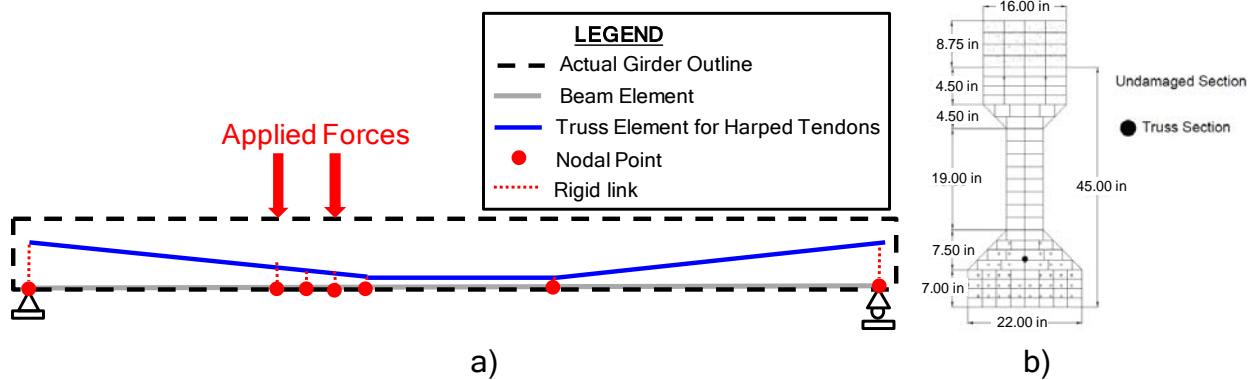
Figure 41. Schematic Description of Nonlinear Beam Model: a) Model Layout and b) Fiber Sectional Model

Material Models and Calibration of Material Properties in Beam Models

The concrete in the girder is modeled using the Hognestad material law (Hisham and Mohd, 1994), as summarized in Figure 42a, which can account for the effect of tensile strength degradation caused by cracking, compressive strength degradation caused by crushing and the stiffness degradation caused by damage in the material.

31

The material in the tendons is described with an elastoplastic law that includes linear kinematic hardening. For monotonic uniaxial loading, such elastoplastic law leads to a bilinear shape of the stress-strain curve, as shown in Figure 42b. An initial autogenous strain is defined for the material of each tendon, such that the tendon stress was equal to the estimated value of actual prestress in the bridge girders. The prestress in the tendons is assumed to be 140 ksi.
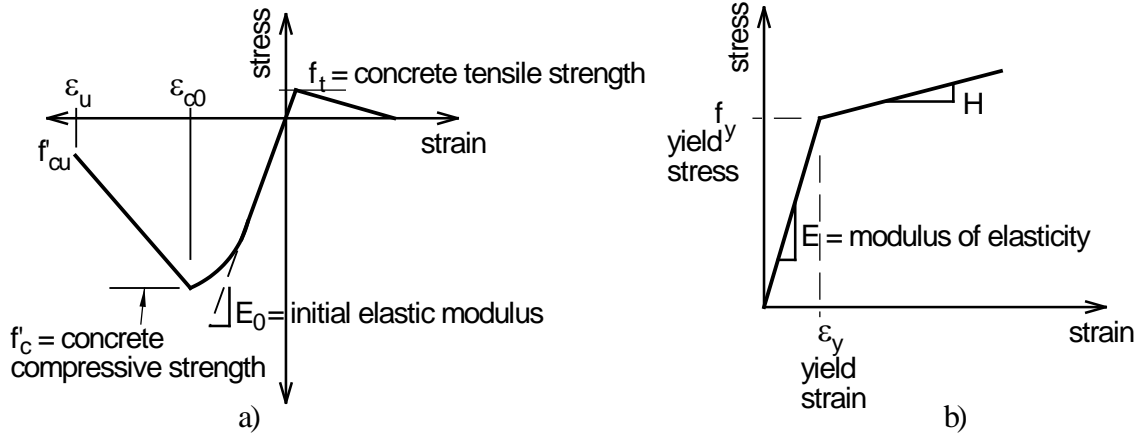

Figure 42. Uniaxial Material Laws used in Beam Models: a) Hognestad Concrete Material Model (Hisham & Mohd, 1994) and b) Elastoplastic Material Model With Linear Kinematic Hardening for Strands

Based on material test data on the girder and deck concrete and on the strands, the material models were calibrated to match the experimentally obtained material strength values. The calibrated uniaxial stress-strain laws for the concrete in the girder and in the deck are presented in Figure 43a, while the calibrated model stress-strain curve of the strand material is compared to the experimentally obtained curve in Figure 43b.
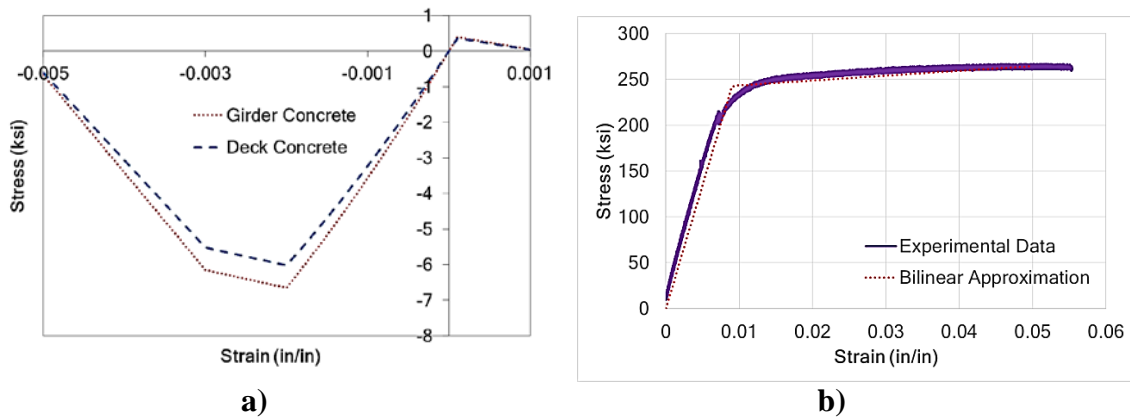
Figure 43. Calibrated Material Laws for Concrete and Steel: a) Hognestad Concrete Material Model (Hisham & Mohd, 1994) and b) Calibration of Tendon Material Model With Material Test Data

For the beam concrete, the peak compressive strength is $f'_c = 6.65$ ksi, while for the deck concrete the compressive strength is $f'_c = 6.02$ ksi. For both concrete models, the peak tensile strength, f_t, was taken as 10% of the compressive strength; the residual compressive strength, f'_{cu}, is 10% of the compressive strength at a ultimate concrete strain of $\varepsilon_u = -0.005$; and the peak compressive strength occurs at $\varepsilon_{co} = -0.002$.

32

The splices are modeled using a multilinear elastoplastic material law. The specific law allows the user to define a stress-strain curve consisting of multiple linear segments and to explicitly capture the effect of material strength degradation caused by fracture. In the present study, and given that the splices had been installed with 150 ft-lb torque, the prestressing in the spliced tendons is assumed to equal 200 ksi, or $0.8 f_{pu}$ where f_{pu} is the ultimate tensile stress of the prestressing strand, in accordance with the manufacturer's recommendation (Prestress Supply Incorporated, 2010). Given the inherent uncertainty in the ultimate strength of the splices, several alternative hypotheses have been examined. The lower bound of splice strength is assumed to be 212.5 ksi and the upper bound is assumed to be 250 ksi (f_{pu}).

Figure 44a presents the stress-strain curves of the spliced tendons for different values of splice failure stress. These curves have been obtained on the basis of the assumption that the spliced strands have the same stress-strain behavior as the undamaged strands and that splice failure leads to sudden strength degradation. It is worth mentioning that the spliced strand stress-strain curve corresponding to splice failure at 250 ksi leads to strain behavior that differs from that of the undamaged tendons. Specifically, the nominal strength of the strands is 250 ksi, and the bilinear stress-strain curve reaches this value at a strain of 0.022. The curve of the undamaged tendons, shown in Figure 44b, reaches higher stresses than 250 ksi, i.e., it reaches a stress of 264 ksi at a strain of 0.05.

The FRP material overlays are also modeled using a multilinear stress-strain curve. The stress-strain curve of the overlays is established using data from the manufacturer. The modulus of elasticity of FRP is $E_f = 10,700$ ksi and the rupture strain for an overlay is $\varepsilon_{fu} = 0.014$. The possibility for debonding of the overlays also needs to be accounted for by the models.

a)   b)
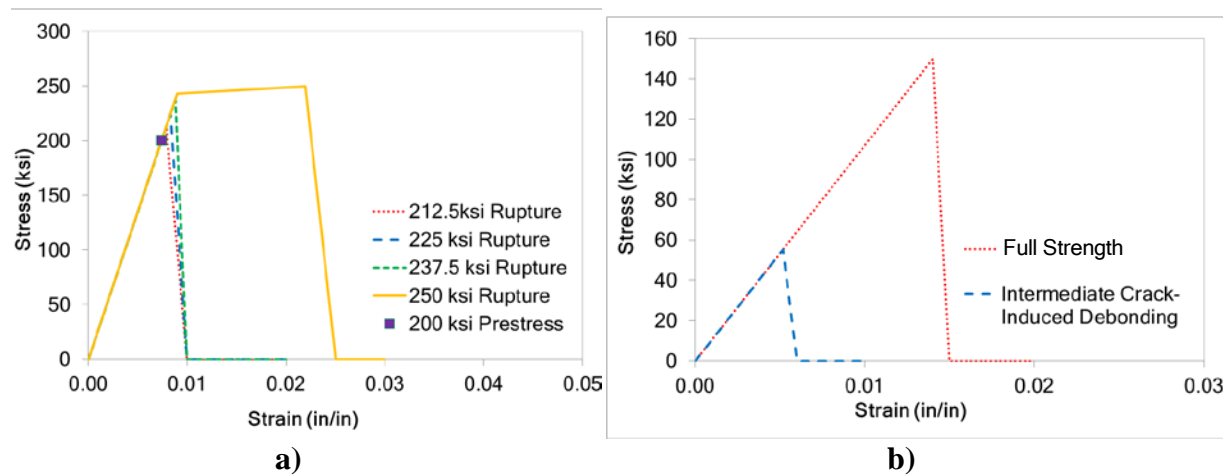
Figure 44. Uniaxial Material Laws for Retrofit Materials: a) Spliced strand stress-strain curves corresponding to different levels of splice failure and b) FRP overlay stress-strain curves corresponding to full fiber strength and to debonding

FRP end peeling (also referred to as plate-end debonding) can result from the normal stresses developed at the ends of externally bonded FRP reinforcement. With this type of debonding, the existing internal reinforcing steel essentially acts as a bond breaker in a horizontal plane, and the concrete cover pulls away from the rest of the beam (Teng et al. 2002). The possibility that such failure occurs is evaluated in Appendix C of Gangi (2015) using

guidance found in ACI 440.2R-08 (2008). The calculations in Gangi (2015) lead to the conclusion that plate-end debonding is not probable. Therefore, it is not examined further in the analytical models of the present study.

Another type of debonding is intermediate crack-induced debonding, for which debonding (loss of adhesive strength) occurs in the vicinity of a crack away from the end regions of the overlays, and then the debonding crack propagates toward the end region of the overlay. ACI 440 2R.08 (2008) provides guidelines to estimate the effective strain, ε_{fd}, at which such FRP debonding can occur. The calculations are presented in Appendix C of Gangi (2015) and give a value $\varepsilon_{fd} = 0.0052$. Since this strain value is less than the rupture strain of the FRP, intermediate crack-induced debonding is deemed the most probable failure mode. The stress-strain curve used for the FRP material is presented in Figure 44b, which compares the stress-strain curve corresponding to full strength (i.e., rupture of the FRP) and the curve corresponding to intermediate crack-induced debonding, which is used in the numerical models.

The behavior of the FRCM overlays was also described using a multi-linear material law. Two alternative stress-strain curves are employed in the present study. The first curve is based on information provided by the manufacturer of the material. According to the manufacturer, the thickness of each FRCM strip is $t_f = 0.0018$ in, the modulus of elasticity is $E_f = 39,200$ ksi and the strain at rupture is $\varepsilon_{fu} = 0.021$. The second curve has been obtained from experimental tests conducted at the University of Miami (Pino and Nanni 2015). ACI 549.4R-13 (2013) establishes an idealized stress-strain curve for FRCM overlays, as shown in Figure 45a. The idealized curve consists of two linear segments. The first linear segment corresponds to the initial stage of behavior. After the strain exceeds a transition strain value, shown in Figure 45a, the slope of the idealized stress-strain law declines (see Figure 45a inset). Using the material test data, Pino and Nanni (2015) established a stress-strain curve similar to that proposed in ACI 549.4R-13. The transition point corresponds to strain and stress values of 0.00017 and 54 ksi, respectively, while the failure corresponds to a strain of 0.017 and a stress of 241 ksi. The ACI 549.4R-13 (2013) states that to account for these three failure modes, the effective tensile strain level in the FRCM reinforcement attained at failure, ε_{fe}, should be limited to the design tensile strain of the FRCM composite material, ε_{fd}, defined as $\varepsilon_{fe} = \varepsilon_{fd} \leq 0.012$. So basically, in the model, the failure strain of the FRCM material was set to be 0.012. The two alternative curves employed for the FRCM, i.e., the one provided by the manufacturer and the one obtained from experimental tests, have been modified to have failure at strain of 0.012, and are shown in Figure 45b.

Solution procedure

In the analysis procedure, the self-weight of each beam is initially applied as a distributed load. The additional concentrated loads, e.g., the applied forces in the experimental tests, are then applied on the models, in incremental load steps. A Newton-Raphson iterative scheme is employed to satisfy the nonlinear equations of equilibrium. Given that strength degradation is expected to occur in the analytical models pursued herein, a displacement-control algorithm (McGuire et al., 2015) is used. In this algorithm, a constrained equation is enforced in each solution step. The load increments are such that a selected nodal displacement reaches a target value in each step. The use of a displacement-control algorithm allows the solution to proceed and converge at each step, even when strength degradation occurs in the analysis.
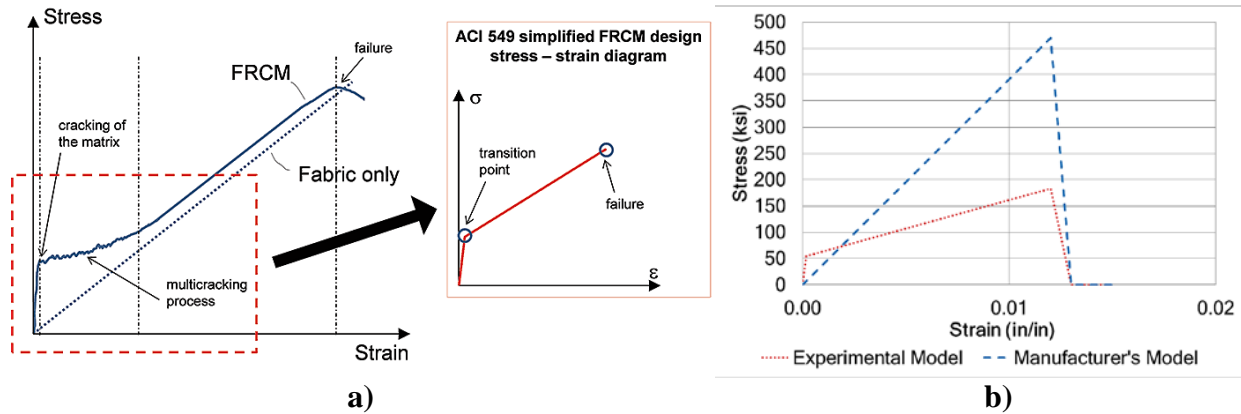
Figure 45. Uniaxial Material Laws for FRCM: a) Idealized stress-strain curve (Tumialan 2014) and b) Alternative stress-strain curves employed in the present study

Description of Continuum-Based Finite Element Models

The three-dimensional, continuum-based, finite element (FE) analyses of the damaged and repaired bridge beams were conducted using the commercial program LS-DYNA (Hallquist, 2007). A schematic presentation of a three-dimensional continuum FE model is presented in Figure 46. As seen in the figure, the model explicitly accounted for the loading apparatus (i.e., the presence of a spreader beam) by means of additional elastic solid elements. The prestressing strands are modeled using truss elements with an appropriate uniaxial stress-strain law.

The damaged and/or repaired regions of the girders are explicitly modeled in the simulations, using appropriate material models and elements. The retrofit overlays (the FRP strips and the FRCM layers) are modeled through the superposition of shell elements on the appropriate locations of the model.
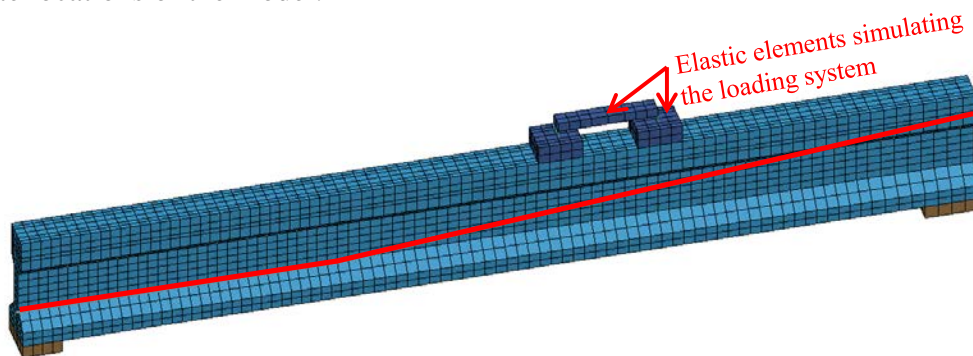

Figure 46. Schematic Presentation of Continuum-based Finite Element Model of Bridge Beam, Highlighting the Truss Elements That Represent the Harped Strands

Given that the presence of the saw cuts at the compressive zone of the girders affected the response of several test specimens, these cuts were accounted for in the FE analyses.

Continuum-Based FE Model Material Models

The behavior of the concrete in the girders and in the repair patches was described using the Winfrith material model (Broadhouse 1995). The specific material model is based on the yield surface proposed by Ottosen (1977), that captures the effect of biaxial and triaxial stress states on the compressive strength of the material. The effect of tensile strength degradation caused by cracking is also accounted for by the model. The material model allows the definition of a compressive failure strain, i.e. the strain at which the concrete is assumed to be fully crushed. In the present study, this failure strain is set equal to -0.003. For this model, beam concrete properties were assumed for the entire cross-section (including deck) for simplicity, though this is not a conservative assumption. Figure 47 shows the concrete material model used for the solid elements in the continuum-based FE analysis.

The material of the strands for the FE models was described by an elastoplastic law with linear kinematic hardening that was calibrated in an identical fashion as that for the beam models. The target prestress in the tendons was obtained in the analyses by defining a temperature increase in the models, which in turn created the autogenous strain required to generate the prestress of each strand.

The strand splices were also modeled as an elastoplastic material with linear kinematic hardening. The analysis software allows the definition of a failure strain, i.e. the value of plastic strain at which the material loses its resistance. By appropriately defining the value of the failure strain, the present study could account for the failure of the strand splices for various levels of tensile strain.
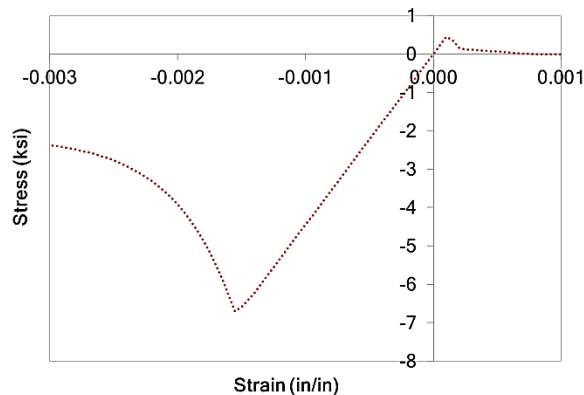
Figure 47. Concrete Material Uniaxial Stress-Strain for Continuum-Based FE Models

The FRP is modeled in LS-DYNA using an enhanced version of the brittle damage model by Chang and Chang (1987) for composite materials. The specific material model can account for the orthotropic nature of an FRP strip, i.e. for the different strength and stiffness properties for the directions parallel and perpendicular to the fibers. Additionally, the model can account for different material strength values that depend on the loading directions. The shell elements used to simulate the FRP overlays include – as different layers – both the strips whose fibers are aligned with the axis of the girder specimen and the transverse strips. The strength in the direction perpendicular to the fibers is assumed to be 10% of the peak strength of the strip.

36

The constitutive model by Chang and Chang (1987) was also used to describe the behavior of the FRCM overlays. The transverse fiber area of the FRCM is about 25% of the corresponding area of the longitudinal fibers, i.e. the fibers that were aligned with the axis of the specimens. For this reason, the strength for the transverse direction of the FRCM overlays is set to 25% of the corresponding strength in the longitudinal direction.

RESULTS

Material Property Characterization

Beam Materials

Deck and Beam Concrete

Table 4 summarizes the failure loads, compressive strengths, and average compressive strength of the cores collected from the beam and the deck. Table 5 summarizes the failure loads, tensile strength, and average tensile strength of the cores collected from the beam. The average compressive strength in the girder was 6,650 psi, which is greater than 5,000 psi as specified by the bridge plans (available in Liesen (2015)). The average compressive strength in the deck was 6,020 psi, which is greater than the specified bridge deck concrete compressive strength of 4,000 psi. The average tensile strength was 424 psi, which is $5.2\sqrt{f'c}$ (in psi).

Table 4. Beam and Deck Concrete Compressive Strength

Sample	Cylinder #	Load, lbs	Diameter, in	Area, in^2	Strength, psi	Average, psi
Beam	1	39,000	2.75	5.94	6,570	6,650
	2	40,000	2.75	5.94	6,730	
Deck	3	35,000	2.75	5.94	5,890	6,020
	4	36,500	2.75	5.94	6,150	

Table 5. Beam Concrete Tensile Strength

Cylinder #	Load, lbs	Diameter, in	Length, in	Strength, psi	Average, psi
5	7,500	2.75	4.50	386	424
6	10,000	2.75	5.00	463	

Reinforcing Steel

Table 6 summarizes the failure loads, tensile strengths, and average tensile strength of the reinforcing steel samples collected from Beam A. The average yield strength was 49.3 ksi and the average tensile strength was 78.5 ksi. These values are consistent with Grade 40 reinforcing steel (Nilson 1987). Figure 48 presents the stress-strain relationships for both tests.

Table 6. Reinforcing Bar Failure Tensile Strength

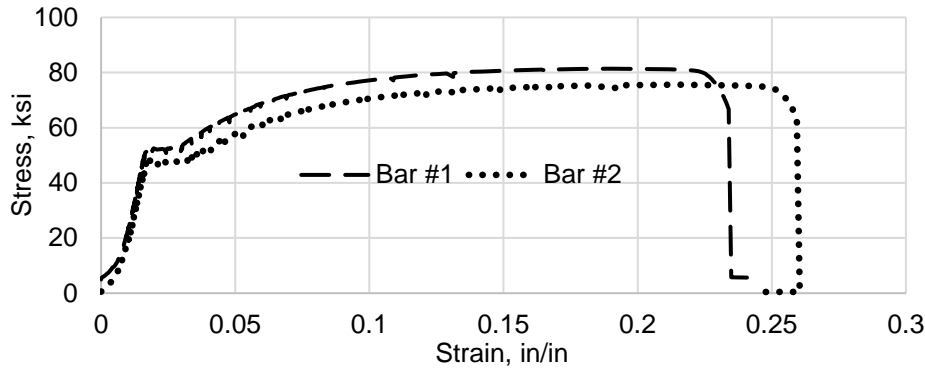| Bar #	Load, kips	Diameter, in	Area, in²	Yield, ksi	Average Yield, ksi	Strength, ksi	Average Strength, ksi
1	16,000	0.5	0.20	52.3	49.3	81.4	78.5
2	14,900	0.5	0.20	46.2		75.6	

Figure 48. Reinforcing Bar Stress-Strain Relationship

Prestressing Steel

Table 7 summarizes the failure loads, tensile strengths, and average tensile strength of the prestressing strand samples collected from Beam A. The average tensile strength was 262 ksi. The average tensile strength indicates Grade 250 prestressing strands (Nilson 1987), which is consistent with the strand specified in the bridge plans (found in Liesen (2015)). Figure 49 shows the stress-strain relationship from the prestress strand tensile tests and the bilinear approximation used for analysis.

Table 7. Prestress Strand Strength

Strand #	Load, lbs	Diameter, in	Area, in²	Yield, ksi	Average Yield, ksi	Strength, ksi	Average Strength, ksi
1	20,500	0.375	0.08	218	214	257	262
2	21,400	0.375	0.08	210		267	

Fiber Reinforced Polymer (FRP)

Direct Tension

All specimens behaved linear-elastically until failure. The primary mode of failure was by tensile rupture of the test coupons with a sudden explosive, gauge middle failure and long splitting gauge middle failure, respectively. The results reported herein have been computed per ASTM D3039 and are reported in Table 8. Note that the results have been calculated using the computed area based on average of three specimen width measurements and nominal thickness.
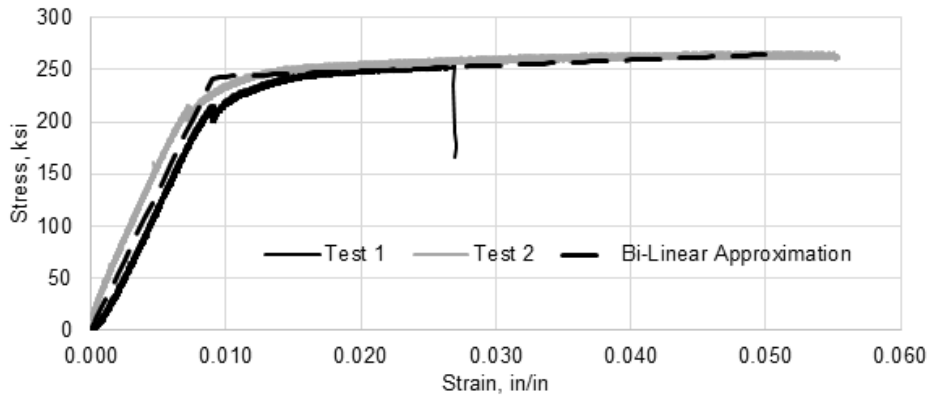
Figure 49. Prestress Steel Stress-Strain Relationship (Gangi, 2015)

Table 8. FRP Tensile Test Results

Specimen ID	Average Width, in	Average Thickness, in	Average Area, in^2	Average Force, lbs	Average Stress, ksi	Average Modulus of Elasticity, ksi	Average Ultimate Strain, %
1 PLY_C200H	1.01	0.04	0.041	7,810	192.6	10,980	1.75
1 PLY_C400H	0.95	0.08	0.076	14,250	187.6	11,040	1.70
2 PLY_C200H	1.02	0.08	0.081	15,910	195.4	13,880	1.41
2 PLY_C400H	1.04	0.16	0.167	22,590	135.6	12,120	1.12

Fabric Reinforced Cementitious Matrix (FRCM)

Compressive Strength of Matrix Mortar

The compressive strength requirement of AC434 Section 4.3 (ICC-ES, 2013b) is 2,500 psi at 7 days and 3,500 psi at 28 days after casting. As shown in the results in Table 9, on average the grout met the requirements as stated. The values in Table 9 are the averages of five tests at each time.

Table 9. Compression Tests of Matrix Mortar Cubes

Specimen ID	Ave. Area, in^2	Peak Load, lb	Compressive Strength, psi	Standard Deviation, Psi
7 Days	4	12,190	3,050	219
28 Days	4	14,640	3,660	430

Compressive Strength of Repair Mortar

Table 10 presents the results of the compression tests of the repair mortar from the characterization study.

Table 10. Compression Tests of Repair Mortar Cubes

Specimen ID	Ave. Area in^2	Peak Load lb	Compressive Strength, psi	Standard Deviation, psi
7 Days	4	18,690	4,670	136
28 Days	4	20,730	5,180	74

Table 11 summarizes the failure load, compressive strength, and average compressive strength for the cylinders collected from the repair concrete. The July 14, 2014 repairs were on Beams B and C. The March 15, 2015 repairs were on Beam D. The average compressive strength at 24 hours was 3,820 psi, which does not meet the advertised design strength of 4,500 psi. The average compressive strength was 6,070 psi at 7 days, which is less than the advertised design strength of 7,700 psi.

Table 11. Repair Concrete Compressive Strength

Time	Repair #	Cylinder #	Failure Load, lbs	Area, in^2	Strength, psi	Average per Repair, psi	Average, psi	Design, psi
24 hr	Jul-14	1	45,000	12.57	3,580	4,060	3,820	4,500
		2	57,000	12.57	4,540			
	Mar-15	3	50,000	12.57	3,980	3,580		
		4	40,000	12.57	3,180			
48 hr	Jul-14	5	69,000	12.57	5,490	5,730	4,970	-
		6	75,000	12.57	5,970			
	Mar-15	7	46,000	12.57	3,660	4,220		
		8	60,000	12.57	4,770			
7 day	Jul-14	9	82,000	12.57	6,520	6,250	6,070	7,700
		10	75,000	12.57	5,970			
	Mar-15	11	83,000	12.57	6,600	5,890		
		12	65,000	12.57	5,170			

Direct Tension

Figure 50 presents the stress versus strain diagrams for the single-ply FRCM coupons tested in direct tension. Plots for the two-ply and one-ply lap specimens can be found in Pino and Nanni (2015). The stress-strain behavior of FRCM control coupon specimens is bi-linear as expected. The initial branch of the curve corresponds to the uncracked specimen, followed by a second branch with a reduced slope, which corresponds to the cracked specimen.

For the single-ply continuous and lap-splice specimens, the primary failure mode is slippage of the fibers after multiple cracking perpendicular to the direction of the load throughout the length of the specimen. A secondary de-bonding failure mode located at the tab ends was observed in some cases. For the two-ply continuous specimens, the primary failure mode is also slippage of the fibers after multiple cracking, but the crack damage progression varied because of the additional layer of fabric. Cracking begins where a crack spans the entire width of the specimen, then the crack begins to propagate through the thickness, but instead of propagating through the entire thickness, the crack propagates through the first layer, and then propagates parallel to the length of the specimen.

The values of modulus of elasticity for the cracked and uncracked specimens are determined as follows, where the experimental curve is divided at the transition point between the two bi-linear portions. This transition point is located where the experimental curve changes slope.
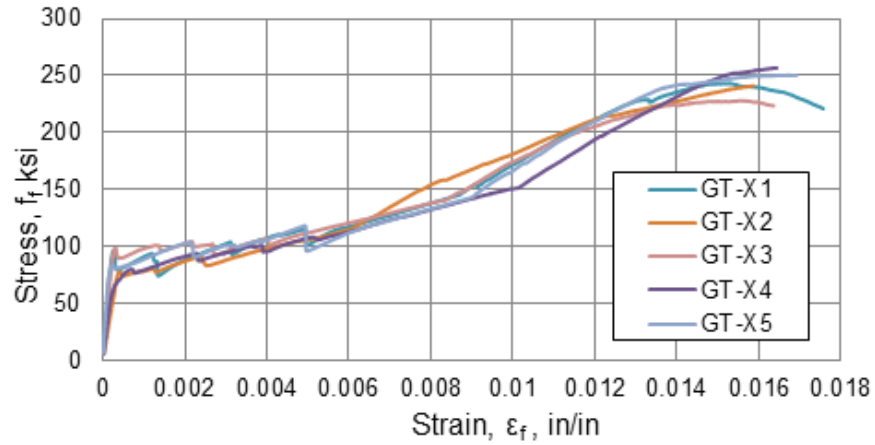
Figure 50. Stress vs. Strain Behavior of Single-Ply Direct Tension Tests

Modulus of the cracked specimen: On the segment of the response curve corresponding to cracked behavior after the transition as defined in AC434 A7.2 (ICC-ES, 2013b), two points are selected on the experimental curve at a stress level equal to $0.90f_{fu}$ and $0.60f_{fu}$. The slope of the line that connects these two points represents the tensile modulus of elasticity at that region:

$$E_f \; = \; \frac{\Delta f}{\Delta \varepsilon} \; = \; \frac{(0.90\, f_{fu} - 0.60\, f_{fu})}{(\varepsilon_{f@0.90\, f_{fu}} - \varepsilon_{f@0.60\, f_{fu}})} \tag{4}$$

where:

E_f = Modulus of elasticity of the cracked specimen;
Δf = Change in stress;
$\Delta \varepsilon$ = Change in strain (tension is positive);
ε_f = strain in fiber corresponding to indicated level of stress
f_{fu} = Ultimate tensile strength; and

Modulus of the un-cracked specimen: It is calculated using the slope between two points. The first point is the origin. The second point is the intersection of the linear trend of the first portion of the experimental curve and the linear trend of the second portion of the experimental curve.

Table 12 contains the average stress, strain and elastic modulus results for the single-ply and two-ply direct tensile tests and lap-tension tests using nomenclature as specified in AC434 .

Early Age Compressive Strength Testing of Matrix Mortar

Table 13 presents the compression test results of matrix mortar cubes at each age. Each result is the average of five tests. It can be seen that compressive strength gain slows after 7 days.

41

Table 12. Direct Tension Properties of FRCM Specimens

Description	Symbol	Single Ply	Two Ply	One-Ply Lap
Modulus of elasticity of the uncracked specimen, ksi	E_f^*	262,000	75,300	365,000
Modulus of elasticity of the cracked specimen, ksi	E_f	18,500	7,170	33,150
Tensile stress corresponding to the transition point, ksi	f_{ft}	54	105	31
Tensile strain corresponding to the transition point, in/in	ε_{ft}	0.00017	0.0027	0.0092
Ultimate tensile strength, ksi	f_{fu}	241	280	236
Ultimate tensile strain, in/in	ε_{fu}	0.0176	0.0277	0.635

Table 13. Early Age Compressive Strength Test Results for Matrix Mortar

Time	Compressive Strength	
	Average Stress, psi	Std. Dev, psi
1 day	1,571	126
2 days	2,221	123
3 days	2,279	204
7 days	3,153	307
14 days	3,010	549
21 days	2,822	118
28 days	3,488	840

Splice Chucks

Table 14 shows the results from the splice chuck torque tests. The table presents the measured stress in the strand, based on load cell readings, in comparison to predicted values of stress at a given torque found in Table 2 as provided by the splice chuck manufacturing company (Prestress Supply Incorporated, 2010). The test averages are also reported as a percentage of the manufacturer's suggested stress. As higher torque was applied to the splice, the measured stresses became smaller than the manufacturer's values as shown in Figure 51.

The applied torque during the installation of the strand splices for Tests 2, 4 and 6 was 150 ft-lb for a design stress of 200 ksi. However, based on the torque splice chuck tests, the strand stress corresponding to a torque of 150 ft-lb was 163 ksi. A general trend was observed that longer strands had lower measured stress for the same applied torque.

Table 15 shows the results from the tests to failure on the spliced strand. In all three tests, the strands failed prior to the splice chuck. It should be noted that the strand used for these tests was Grade 270 prestressing strands while the strands in the beams were Grade 250. Based on these results, the strands should fail in tension before the splice chuck.

Table 14. Strand Splice Chuck Torque Test Results

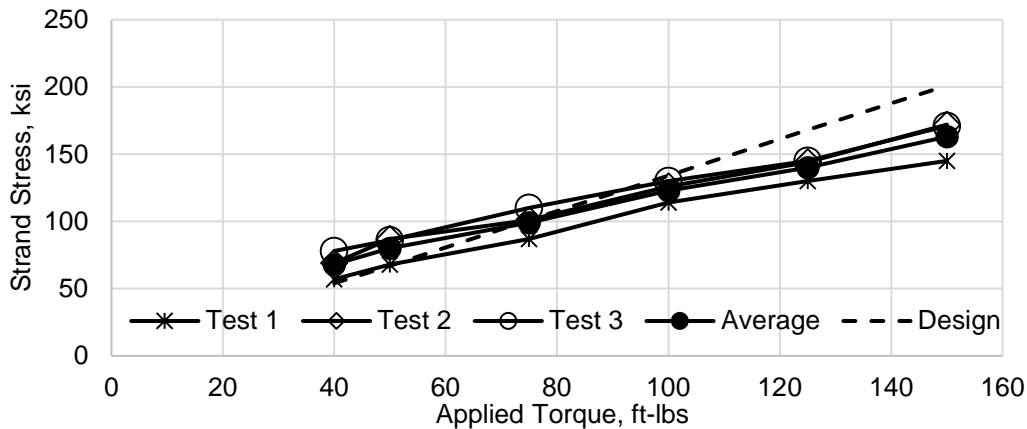| Torque, ft-lb	Test 1 16 ft ksi	Test 2 6 ft ksi	Test 3 4 ft ksi	Average ksi	Manufacturer's Stress, ksi	% Average Tested vs. Design
40	57	69	78	68	54	127%
50	68	87	86	80	67	120%
75	87	101	110	99	101	99%
100	114	126	130	123	134	92%
125	130	144	145	140	168	83%
150	145	172	171	163	200	81%

Figure 51. Strand Splice Torque-Tension Relationship

Table 15. Spliced Strand Tension Test

Test #	Load, lb	Length Chuck-to-Chuck, ft	Stress, ksi	Failure Mode
1	23,300	16	291	Strand Fracture
2	22,800	6	285	Strand Fracture
3	24,000	4	299	Strand Fracture
Average:	**23,300**		**292**	

Effective Prestress

Table 16 summarizes the effective prestress tests. The results of measurements of strands 2, 3, 4 and 6 indicate that the extensometer slipped. When averaging only the results from Strands 1 and 5, the effective prestress force was 132 ksi. Using AASHTO equation 5.9.5.3-1 to estimate time-dependent losses, the approximate effective prestress force after losses is 143 ksi. The measured result of 132 ksi is within 8% of the stress calculated using the AASHTO approximation.

Table 16. Effective Prestress Force

Strand #	Initial Length, in	Length Change, in	Strain, in/in	Effective Prestress Force, ksi
1	2.0104	0.0102	0.0051	137
2	2.0085	0.0191	0.0095	257
3	2.0057	0.0310	0.0155	417
4	2.0131	-0.0012	-0.0006	-16.1
5	2.0071	0.0095	0.0047	128
6	2.0059	0.0254	0.0127	342

Laboratory Tests

Test 1

The control test, with a span of 35 ft, reached an applied load of 401 kips, resulting in a maximum applied moment of 3,070 k-ft plus self-weight of the beam and deck of approximately 1.0 kips/ft, for a total moment of 3,223 k-ft. The maximum deflection was 1.85 in on the second trial, not including 0.20 in of residual deflection after the first trial. The cracking load was approximately 267 kips, resulting in an applied cracking moment of 2,050 k-ft and a total cracking moment of 2,197 k-ft.

At 401 kips, the actuator reached its maximum capacity, so the control test had to be concluded without failing the beam. Cracking patterns between and around the load points were consistent with impending flexural failure. Figure 52 shows the measured moment versus deflection curve compared to the predicted moment capacities found using AASHTO and moment-curvature methods. Since the beam had already cracked during the first trial, the second test trial showed less stiffness as it neared the original cracking moment. Table 17 compares the cracking moment and the nominal moment obtained from the test with predictions using AASHTO and moment curvature. This table also includes a ratio of the experimental moments divided by the predicted moments. The predictions based on each analysis method are conservative in estimating both the ultimate moment capacity and the cracking moment.

Test 2

Test 2, with a span of 58 ft, reached an applied load of 197 kips, for a maximum applied moment of 2,470 k-ft and a total moment, including approximately 0.78 kips/ft self-weight of the girder and deck, of 2,798 k-ft. The maximum deflection was 4.12 in. The cracking load was approximately 60 kips, which equates to an applied cracking moment of 750 k-ft and a total cracking moment of 1,077 k-ft.

The failure mode of Test 2 was a flexural-tensile failure in which one repaired strand slipped out of its splice chuck and one strand ruptured. Cracks formed and widened in the repair area, showing signs of failure prior to reaching the ultimate load and providing warning of an imminent failure. Figure 53 (left) shows the repair concrete at failure. After completion of the

test, the repair concrete was chipped out to investigate the performance of the strand splices and observe the failure. Figure 53 (right) also shows the failure, with one repaired strand having slipped out of the splice chuck and another prestressed strand having ruptured. The picture was taken after the girder was removed from the testing area and stored outside for a period of time, which allowed rust to form. Many of the spliced strands experienced significant yielding, with permanent deformation evident.
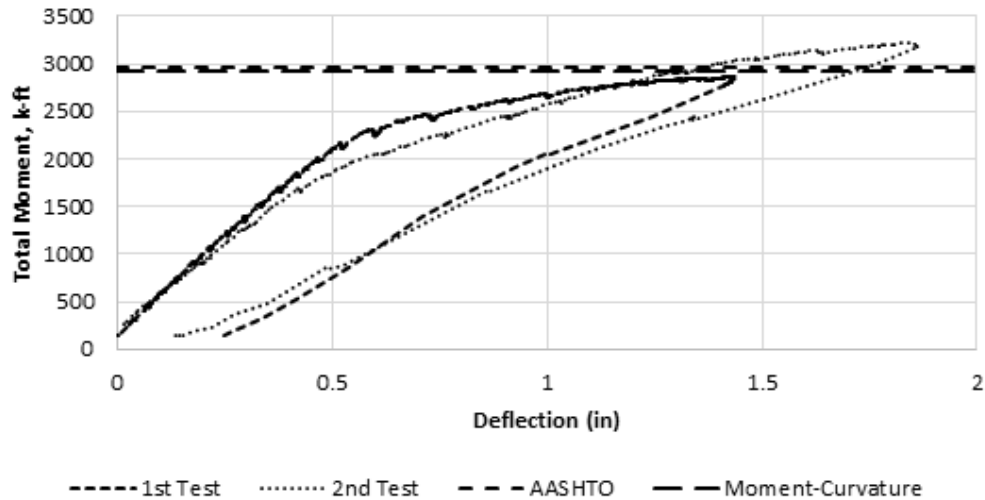

Figure 52. Test 1 Moment Versus Deflection Behavior

Table 17. Test 1 Cracking and Ultimate Moment Experimental Data Versus Analytical Predictions

	Cracking Moment, k-ft	Ultimate Moment, k-ft	$M_{cr\ test}/$ $M_{cr\ calculated}$	$M_{n\ test}/$ $M_{n\ calculated}$
Tested	2,200	3,220	-	-
AASHTO	1,950	2,950	1.13	1.09
Moment-Curvature	2,150	2,930	1.02	1.10

M_{cr} = moment necessary to induce cracking; M_n = nominal (unfactored) ultimate moment capacity

Figure 53. Flexural Cracks in Patch Concrete at Failure (left) and Failed Splices and Strands (right)

The total moment versus deflection curve of the test is shown in Figure 54 as compared with predictions using AASHTO and moment-curvature. Table 18 compares the cracking moment and the nominal moment obtained from the test data with predictions using each analysis method. Each method accurately predicted the nominal moment capacity of the girder.

45

The lower cracking moment from the experimental data is likely caused by the repair concrete not being precompressed during installation.
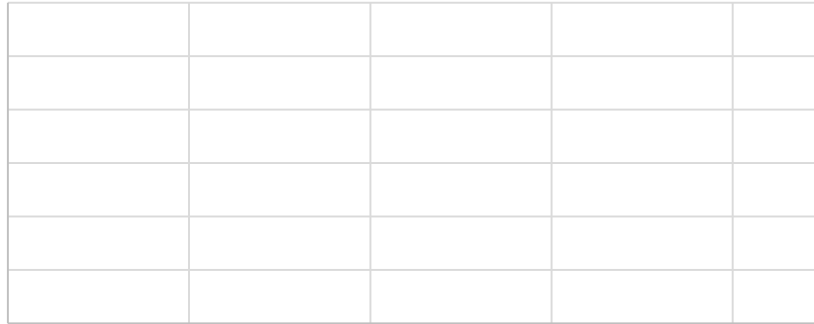

Figure 54. Test 2 Moment Versus Deflection Behavior

Table 18. Test 2 Cracking and Ultimate Moment Experimental Data versus Analytical Predictions

	Cracking Moment, k-ft	Ultimate Moment, k-ft	$M_{cr\ test}/$ $M_{cr\ calculated}$	$M_{n\ test}/$ $M_{n\ calculated}$
Tested	1,080	2,800	-	-
AASHTO	1,710	2,780	0.63	1.01
Moment-Curvature	2,050	2,720	0.53	1.03

M_{cr} = moment necessary to induce cracking; M_n = nominal (unfactored) ultimate moment capacity

Test 3

Test 3 reached a load of 313 kips and a deflection of 3.16 in for the first iteration and a load of 277 kips and a deflection of 3.35 in for the second iteration. The span was 48 ft for the first iteration and 53 ft for the second iteration. The calculated moment applied to the girder based on the maximum load, including self-weight, was 3,540 k-ft during the first iteration and 3,410 k-ft for the second iteration. Cracking in the concrete was first identified as it propagated from under the FRP at a load of 220 kips, corresponding to a cracking moment of 2,750 k-ft. Cracking was noted in the epoxy of the FRP composite system prior to this, but any cracking that may have existed in the concrete was hidden by the FRP.

The beam showed signs consistent with developing flexural failure prior to the end of the test. The cracking pattern in the deck between the load points indicated a compression failure was imminent. Figure 55 presents the predicted nominal moment versus deflection curves with the applied moment versus deflection curve for Test 3. Table 19 compares the calculated cracking and nominal moments with the applied cracking and failure moments. The AASHTO and moment-curvature calculations for the cracking moment appear very conservative. However, the variation can be explained when considering that initial cracking most likely occurred before it was visible above the FRP. AASHTO calculations and moment-curvature calculations both over-predicted the moment capacity of the girder.
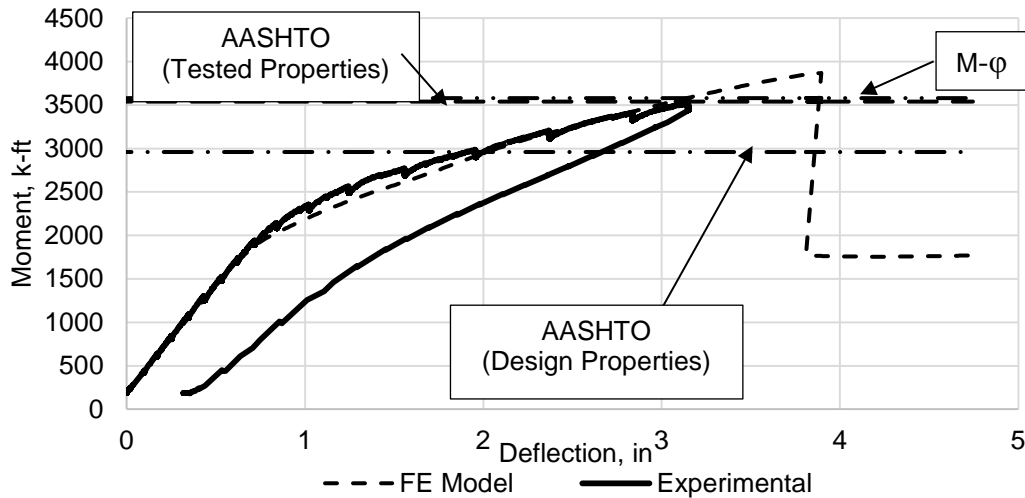
Figure 55. Test 3 Moment Deflection Behavior (M-φ = moment-curvature)

Table 19. Test 3 Cracking and Ultimate Moment Experimental Data versus Analytical Predictions

	Cracking Moment, k-ft	Nominal Moment, k-ft	$M_{cr\ test}/$ $M_{cr\ calculated}$	$M_{n\ test}/$ $M_{n\ calculated}$
Tested	2,750	3,540	-	-
AASHTO (Tested Properties)	201	3,540	13.7	1.00
Moment-Curvature	132	3,580	20.8	0.99

M_{cr} = moment necessary to induce cracking; M_n = nominal (unfactored) ultimate moment capacity

Test 4

Test 4 was executed with a span of 58 ft for the first iteration and 50 ft for the second iteration. The first iteration of the test reached an applied load of 241 kips and a deflection of 4.12 in, for an applied moment of 2,921 k-ft and a total moment of 3,213 k-ft, including self-weight of approximately 0.78 kips/ft. The second iteration of the test reached an applied load of 266 kips and a deflection of 3.61 in, for an applied moment of 2,931 k-ft and a total moment of 3,163 k-ft including self weight. Cracking was observed for the first iteration at an applied load of approximately 120 kips for an applied cracking moment of 1,450 k-ft and a total cracking moment of 1,753 k-ft.

The failure mode of Test 4 was a flexural-compression failure in which the concrete in the deck between the load points was crushed (Figure 56 (left)). Flexural cracking was observed along the bottom flange, with widening cracks as the load increased near the ultimate capacity (Figure 56 (right)). After the test, the repair concrete was chipped out to investigate the strand splices, which showed no observable slipping, rupturing, or excessive yielding.

The total moment versus deflection curve for the first iteration is shown in Figure 57 and compared with predictions using AASHTO and moment-curvature. Figure 58 shows the total moment versus deflection curve for the second iteration and compares it to predictions. Table 20 compares the cracking moment and nominal moment obtained from test data with predictions using each analysis method. The AASHTO and moment-curvature methods provided

conservative estimates of strength. Similar to Test 2, each method over-predicted the cracking moment because of the lack of precompression in the repair concrete.

Figure 56. Test 4 Flexural Compression Failure in the Deck (left) and Cracking Pattern in Beam Below Load Point (right)
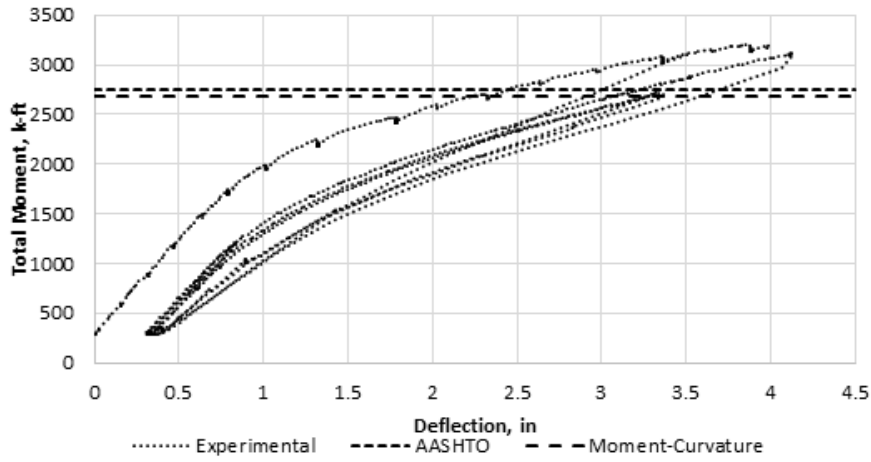

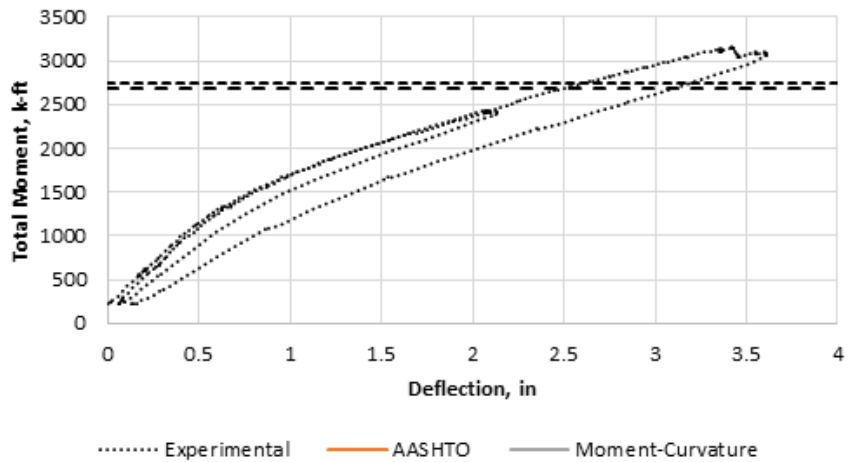**Figure 57. Test 4, Iteration 1 Moment Deflection Behavior**

**Figure 60
58. Test 4, Iteration 2 Moment Deflection Behavior**

48

Table 20. Test 4 Cracking and Ultimate Moment Experimental Data Versus Analytical Data

	Cracking Moment, k-ft	Ultimate Moment, k-ft	$M_{cr\ test}/$ $M_{cr\ calculated}$	$M_{n\ test}/$ $M_{n\ calculated}$
Tested	1,750	3,160	-	-
AASHTO	1,820	2,740	0.96	1.15
Moment-Curvature	2,060	2,710	0.85	1.17

M_{cr} = moment necessary to induce cracking; M_n = nominal (unfactored) ultimate moment capacity

Test 5

Test 5, with a span of 52 ft, reached an applied load of 222 kips, for a maximum applied moment of 2,514 k-ft and a total moment of 2,768 k-ft including the self-weight of the girder of 0.78 kips/ft. The total deflection at the center of load was 3.02 in. Cracking was observed at an applied load of approximately 180 kips for an applied cracking moment of 2,038 k-ft and a total cracking moment of 2,293 k-ft.

The beam failed in horizontal shear transfer because of saw-cut gaps along the length of the girder from demolition of the bridge (see Figure 39). These saw cuts split the composite deck into different lengths and restricted the deck's ability to act compositely with the beam. Cracking occurred in the deck but cracks retreated below the saw cuts into the girder, creating a stress concentration. The failure occurred suddenly with concrete crushing in the interface of the deck and the beam.

The total moment versus deflection curve for the Test 5 is shown in Figure 59 and compared with predictions using AASHTO. Table 21 compares the cracking moment and nominal moment obtained from test data with predictions using each analysis method. The AASHTO and moment-curvature methods were both conservative. Possibly because of the FRCM material covering up cracks in the girder, the estimate of the cracking load from the AASHTO method was very low.
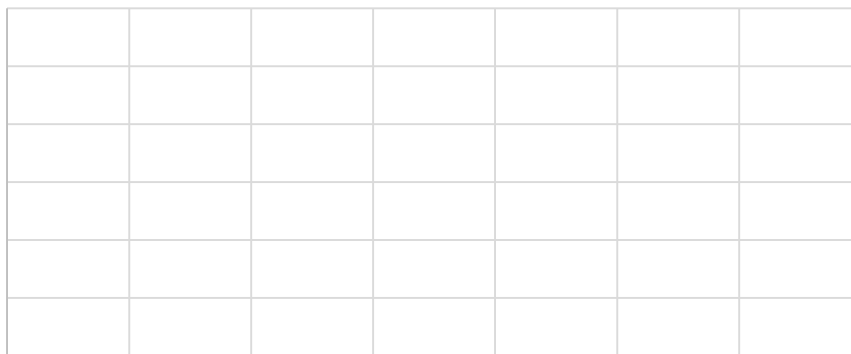

Figure 59. Test 5 Moment Versus Deflection Behavior

Table 21. Test 5 Cracking and Ultimate Moment Experimental Data Versus Analytical Data

	Cracking Moment, k-ft	Ultimate Moment, k-ft	$M_{cr\ test}/$ $M_{cr\ calculated}$	$M_{n\ test}/$ $M_{n\ calculated}$
Tested	2,290	2,770	-	-
AASHTO	1,580	2,670	1.45	1.04
Moment-Curvature	1,870	2,710	1.22	1.02

M_{cr} = moment necessary to induce cracking; M_n = nominal (unfactored) ultimate moment capacity

Test 6

Test 6, with a span of 52 ft, reached an applied load of 269 kips, for a maximum applied moment of 3,050 k-ft and a total moment of 3,304 k-ft including self-weight. The total deflection was 3.62 in. Cracking was heard and then observed at an applied load of approximately 170 kips for an applied cracking moment of 1,926 k-ft and a total cracking moment of 2,180 k-ft.

The failure mode of Test 6 was a flexural compression failure in which the concrete in the deck between the load points crushed. This failure is shown in Figure 60. Flexural cracking was observed along the bottom flange, with widening cracks as the load increased near the ultimate capacity. The total moment versus deflection curve for Test 6 is shown in Figure 61 and compared with predictions using AASHTO. Table 22 compares the cracking moment and nominal moment obtained from test data with predictions using each analysis method. The AASHTO and moment curvature methods both under-predicted the nominal moment capacity of the girder. Possibly because of the FRCM material covering up cracks in the girder, the estimate of the cracking load from the AASHTO method was very low.

Figure 60. Compression Failure in the Composite Deck

Table 22. Test 6 Cracking and Ultimate Moment Experimental Data Versus Analytical Data

	Cracking Moment, k-ft	Ultimate Moment, k-ft	$M_{cr\ test}/$ $M_{cr\ calculated}$	$M_{n\ test}/$ $M_{n\ calculated}$
Tested	2,180	3,300	-	-
AASHTO	1,710	2,840	1.27	1.16
Moment-Curvature	2,030	2,890	1.07	1.14

M_{cr} = moment necessary to induce cracking; M_n = nominal (unfactored) ultimate moment capacity

Figure 61. Test 6 Moment Versus Deflection Behavior

Validation of Analysis Methods

This section compares the tested and calculated data from the reported tests. In the analyses presented herein, the self-weight of the beam was initially applied as a distributed loading. Subsequently, the concentrated applied forces were introduced in the model. Since the deflection resulting from self-weight of the specimens was present in the unloaded state of the beams, the reported analytical results provide values of the additional deflection caused by the concentrated loadings. In other words, the deflection caused by self-weight of the girders is removed from the analytical results. The load-deflection response from each test is presented and the ability of both the nonlinear beam models and continuum-based FE models to predict those responses is discussed.

Validation of Nonlinear Beam Models

The results of the validation analyses using the beam models for the first test are presented in Figure 62a for Test 1.1 and Figure 62b for Test 1.2. The failure mode for both analyses was concrete crushing in the deck. This was indicated by the fact that at peak load, the strain in the concrete fiber at the top of the deck reaches -0.003, the ACI indicator of crushed concrete. Both analyses match well with the experimental data, especially the second iteration, which was more important to modeling because there was no equipment failure to affect the experimental results.

The analyses for the second test were conducted for four different values of strand splice strength. The first analysis run was at the lower bound of splice strength, 212.5 ksi ($0.85\,f_{pu}$). The second analysis was at 225 ksi ($0.9\,f_{pu}$) splice strength.   The third analysis was at 237.5 ksi ($0.95\,f_{pu}$) splice strength, while the fourth analysis was at the upper bound of splice strength at 250 ksi (f_{pu}). The results of these analyses are shown in Figure 63a. The failure mode for the first three analyses was strand splice rupture. This was indicated by the fact that at peak load, the stress in the repaired steel strand fiber reaches the specified splice strength, and then begins to decrease as load drops. The fourth analysis, though, with splice strength at full 250 ksi, fails in

51

concrete crushing mode, with the strain in the concrete fiber at the top of the deck reaching -0.003 (under the sign convention used, negative strain indicates compression).
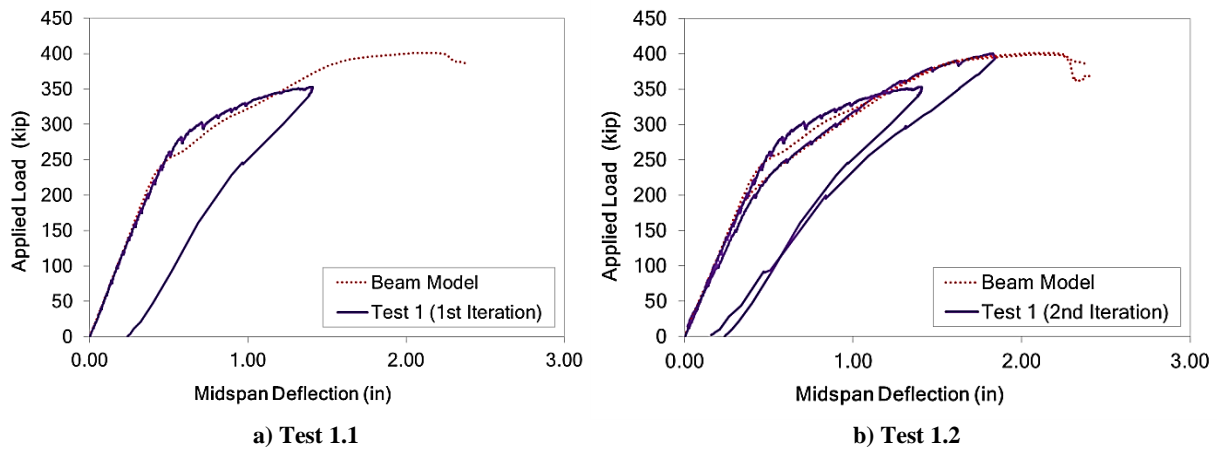

a) Test 1.1   b) Test 1.2
Figure 62. Comparison of Experimental and Analytical Load-Deflection Curves for Test 1

Both the second and third analyses match well with the experimental data, especially the peak load of the 225 ksi analysis, and the predicted maximum deflection of the 237.5 ksi analysis. Based on the analysis results, the 212.5 ksi failure strength for strand splices under-predicts the strength of the repair, while the 250 ksi failure strength over-predicts the strength. The 225 ksi and 237.5 ksi models are so close that one cannot be chosen by using nonlinear beam models alone. The more refined, continuum-based, FE analyses discussed in the following section allowed the selection of a unique curve for the spliced strands.

Two analyses were conducted for the third test, using alternative stress-strain curves for the FRP overlay. The first analysis was of the intermediate crack-induced debonding failure scenario. The failure mode for this analysis was FRP debonding, indicated by the fact that at the peak load, the strain in the FRP layer, ε_{fd}, reaches 0.005173. The second analysis was of the full flexure failure scenario. The failure mode for this analysis was concrete crushing, where the strain in the concrete fiber at the top of the deck reaches -0.003, which is the ACI indicator of crushed concrete (ACI 318-14, 2014). The results of these analyses are shown in Figure 63b.
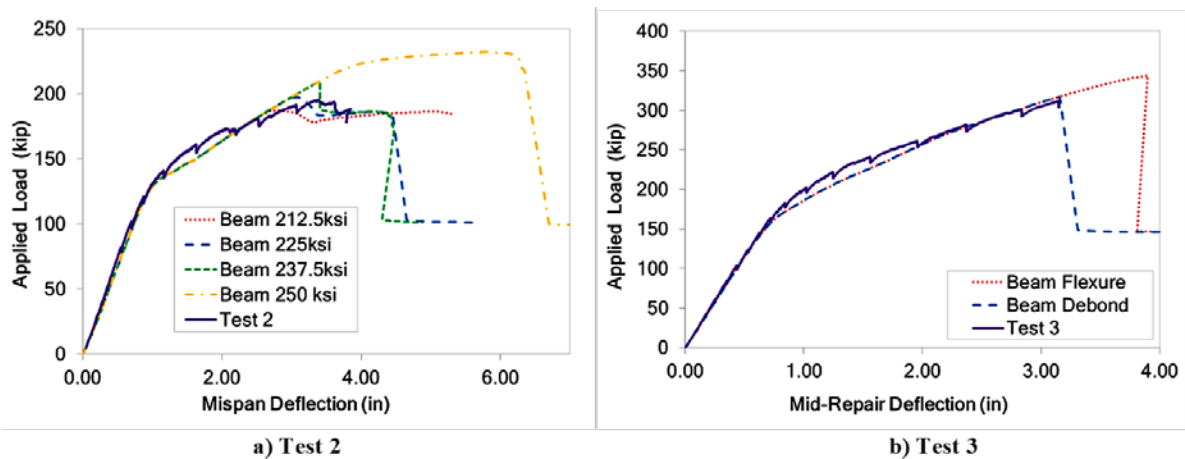

a) Test 2   b) Test 3
Figure 63. Comparison of Experimental and Analytical Load-Deflection Curves for Tests 2 and 3

Both analyses match well with the experimental data. Since the peak load of the debonding mode corresponds to a deflection of 3.15 inches, which was the deflection at the end of the test, it cannot be determined which material model should be preferred for the FRP repair. Such decision is rendered possible by the more refined FE analyses presented in the following section.

For the Test 4 nonlinear beam model, the four analyses were of the two different splice strengths with the two different iterations of the test setup. Since the failure of Test 4 was by concrete crushing and splice rupture was not seen, it was assumed that the splice strength had been fully restored to 250 ksi (f_{pu}). The splice model from the Test 2 splice repair was confirmed, as rupture occurred at 225 ksi (0.9 f_{pu}). Modeled in these analyses are the two most likely splice strengths: 225 ksi (0.9 f_{pu}) and 250 ksi (f_{pu}).

The first set of analyses was the first iteration of the test, where the span was 58 ft and the beam was loaded to 241 kips before it became apparent that the beam was becoming out of plumb. The results of the analyses of this load setup with splice strength of 225 ksi (0.9 f_{pu}) and 250 ksi (f_{pu}) are shown in Figure 64a. The second set of analyses was the second iteration of the test, where the span was changed to 50 ft and the beam was loaded until concrete crushing failure occurred. To model this scenario, the model was loaded to 241 kips, unloaded, and then the load-deflection response was recorded. This was done to account for the cracking caused by such preloading. The results from this second analysis are shown in Figure 64b.
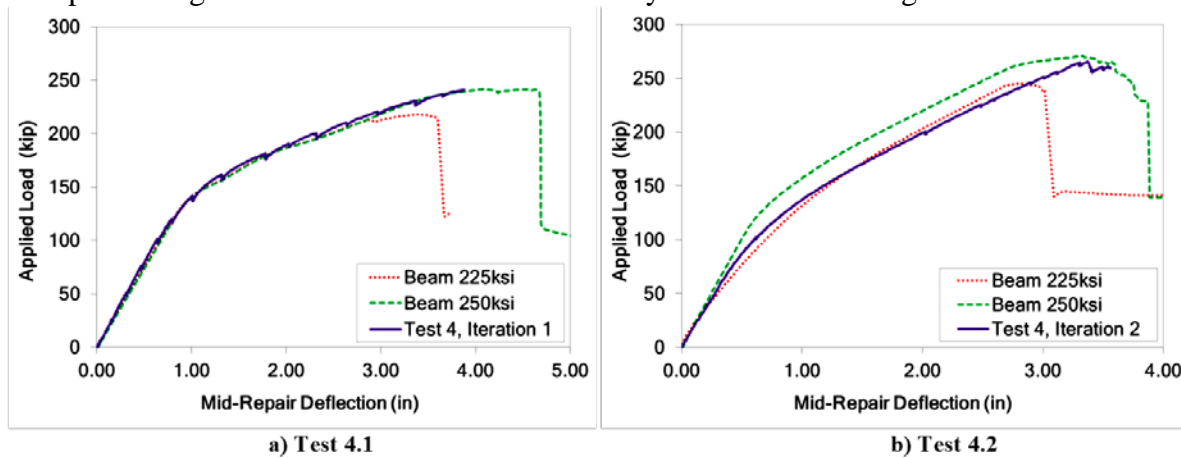

a) Test 4.1   b) Test 4.2

Figure 64. Comparison of Experimental and Analytical Load-Deflection Curves for Test 4

The failure mode for both iterations at 225 ksi splice strength was strand splice rupture, while at 250-ksi splice strength the failure mode was concrete crushing. This indicated that the 250-ksi splice strength model was more appropriate for this scenario because the failure mode in the Test 4, Iteration 2 was concrete crushing. It was valid to assume that the 250-ksi failure strength for strand splices was the correct model to use for a four-strand splice repair.

For the Test 5 nonlinear beam model, the two analyses were of the two different FRCM material model scenarios. The first analysis was the elastic manufacturer's model scenario. The second analysis was the bilinear experimental model scenario. The failure mode of both analyses was concrete crushing, where the strain in the concrete fiber at the top of the deck reaches -0.003. The results of these analyses are shown in Figure 65. Both analyses match well

53

with the experimental data up until the point when the beam was unloaded at 180 kips. It is possible that this point was when horizontal shear cracking occurred between the girder and deck; thus the deck effectively contributed less to carrying compressive load, which resulted in a lesser load-deflection response than expected.

Since the issues with horizontal shear cracking occurred, results from these analyses were inconclusive as to which model better predicts behavior.
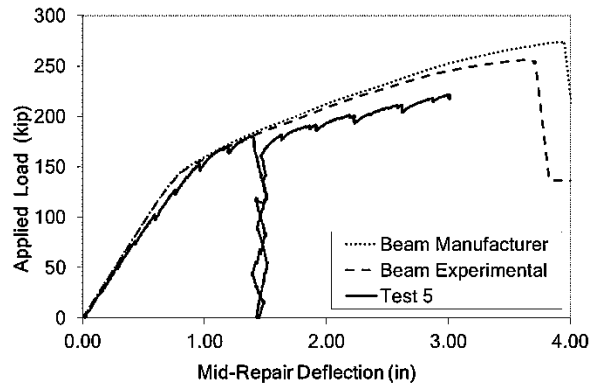

Figure 65. Load-Deflection Response of Test 5 Versus Nonlinear Beam Models

For the Test 6 nonlinear beam model, the four analyses were of the two different splice-material model scenarios and the two different FRCM-material model scenarios. The first set of analyses was of the manufacturer's FRCM model and the two splice strengths of 225 ksi ($0.9\,f_{pu}$) and 250 ksi (f_{pu}). The second set of analyses was of the experimentally derived FRCM model and the two splice strengths. In all analyses, the failure mode was concrete crushing, where the strain in the concrete fiber at the top of the deck reaches -0.003. From the two analyses of splice strength of 225 ksi, although the splices ruptured in the analysis, the FRCM had enough residual tensile strength to allow full flexural failure of the girder. The results of the manufacturer's FRCM model analyses are shown in Figure 66a, while the experimental FRCM model analyses are shown in Figure 66b.
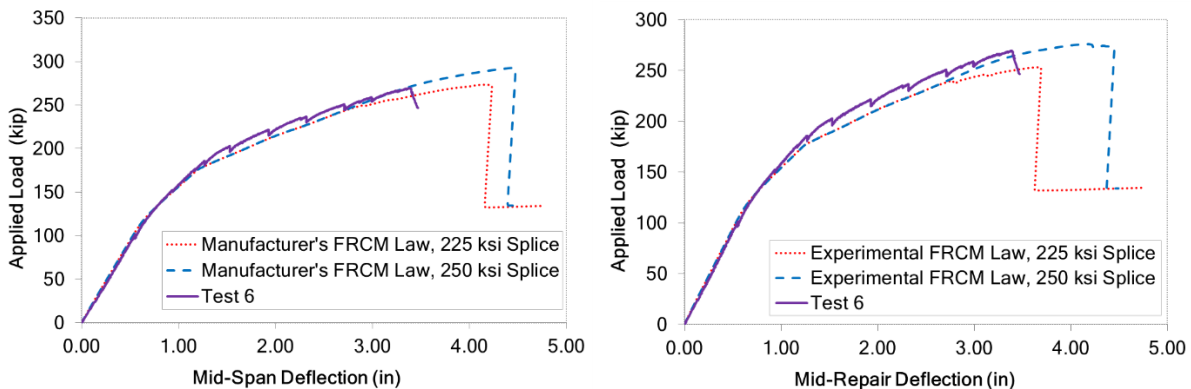

Figure 66. Comparison of Experimental and Analytical Load-Deflection Curves for Test 6: a) FRCM Model Based on Manufacturer's Data (Man.) and b) FRCM Model Based on Experimental Material Test Data (Exp.)

54

The two analyses at 250-ksi splice strength matched well with the experimental results, while the analyses with 225-ksi splice strength under-predicted the strength. The difference in the two FRCM models was not substantial enough to determine which is preferable, so a continuum-based FE model was used to determine the more accurate FRCM model.

Validation of Continuum-Based FE Models

A single analysis was conducted for the first test because of difficulties in establishing the exact loading scenario of the test. The analytical model was validated by the combination of the curves of both iterations of Test 1, which show the initial cracking in the first iteration and the post-cracking behavior in the second iteration. The failure mode within the continuum-based FE model was concrete crushing, just as in the nonlinear beam model. The results of this analysis are shown in Figure 67a. The continuum-based FE model matches well with the experimental data, though slightly over-predicts the girder strength.

For the Test 2 continuum-based FE model, the two analyses were of the two different splice strength scenarios. The first analysis run was at 225-ksi ($0.9\,f_{pu}$) splice strength, while the second analysis was at 237.5-ksi ($0.95\,f_{pu}$) splice strength. The results of this analysis are shown in Figure 67b. The failure of the continuum-based FE model was not strand rupture, as in the nonlinear beam model, but concrete crushing. It can be seen in the load-deflection plot that the girder loses strength with the splice rupture, but has enough residual tensile strength with those elements removed to continue until full flexural failure.

Both the continuum-based FE analyses agreed with the experimental data up until the peak load and both predicted the splice elements rupturing. Each analysis predicted residual strength in the girder that led to full flexural failure, which was not the case in the experimental test. For the purposes of being conservative, for the case of eight strands spliced, the preferred model for the strand splices to be used for subsequent analyses is splice rupture at 225-ksi ($0.9\,f_{pu}$) strength.

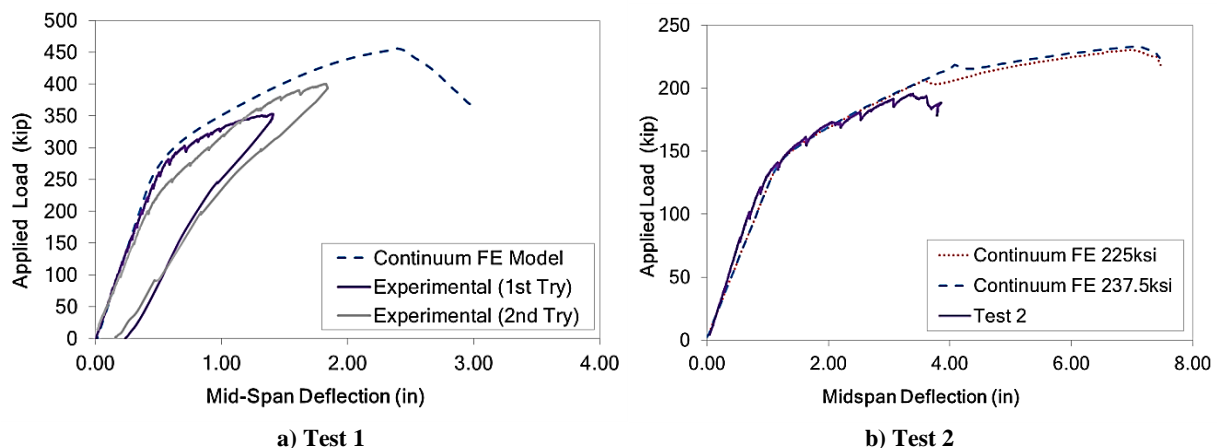a) Test 1   b) Test 2
Figure 67. Comparison of Experimental and Analytical Load-Deflection Curves for Tests 1 and 2

For the Test 3 continuum-based FE model, the two analyses were of the two different FRP failure mode scenarios. The first analysis was of the intermediate crack-induced debonding

failure scenario, and the second analysis was of the full flexure failure scenario. The results of these analyses are shown in Figure 68a. Both analyses surprisingly showed concrete crushing as the failure mode. This was because, even with the debonding stress-strain model, there was shown to be redistribution of stresses in the shell elements when debonding was reached in one shell. Because of the redistribution of stresses, further strength was achieved until flexural failure.

Both the analyses agree with the experimental data. Since both analyses show the same strength, it is conservative to assume the use of the intermediate crack-induced debonding strength model to be the appropriate model for subsequent analyses. For the Test 4 continuum-based FE model the only analysis run was the Test 4, Iteration 1 support condition with strand splice strength of 250 ksi (f_{pu}). The results of this analysis are shown in Figure 68b.   The failure of the continuum-based model is, just as in the nonlinear beam model, concrete crushing.

It is valid to assume that for the case of four strands spliced, the model for the strand splices to be used for subsequent analyses is the one with splice rupture at 250-ksi (f_{pu}) strength. There is a discrepancy between the splice models depending on the amount of strands spliced. This could have been due to the fact that with more strands spliced, more stress was concentrated in the splice chuck, and the splice rupture was not purely tensile, but a combination of shear and tension.
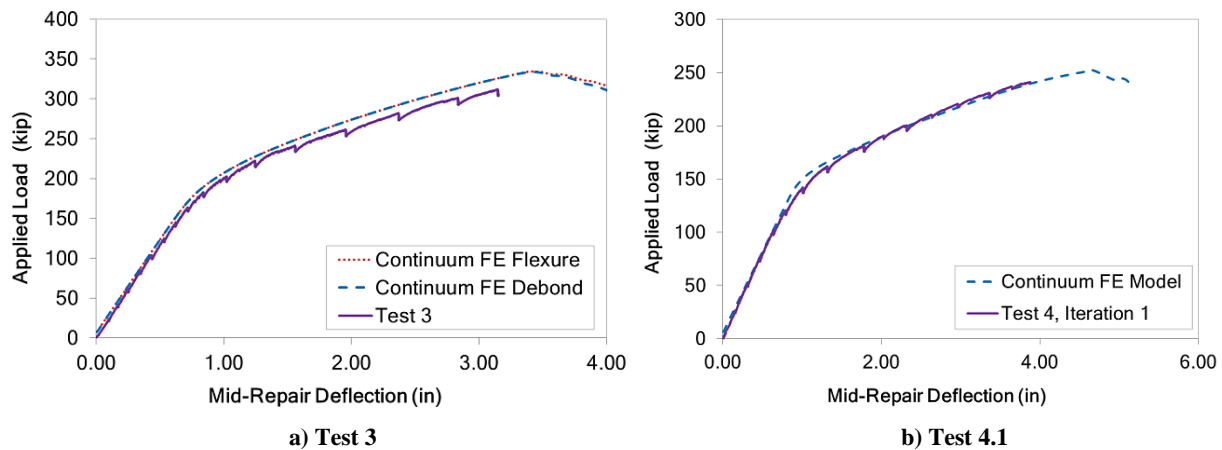

a) Test 3   b) Test 4.1

Figure 68. Comparison of Experimental and Analytical Load-Deflection Curves for Tests 3 and 4.1

For the Test 5 continuum-based FE model the two analyses run are with the two different FRCM material model scenarios. The first analysis run was the elastic manufacturer's model scenario. The second analysis run was the bilinear experimental model scenario. The results of this analysis are shown in Figure 69a. Both analyses indicate failure caused by concrete crushing. The effect of the modeled saw cuts is evident in the analyses. At the saw cut locations, concrete deck elements fail in a different manner than in the experimental test. Similar to the nonlinear beam analyses, both continuum-based FE analyses agree with the experimental data up until the point when the beam was unloaded at 180 kips. It remains probable that this point was when the horizontal shear cracking occurred. The horizontal shear cracking led to less deck effectively present to carry compressive load, causing a decreased load-deflection response than was expected.
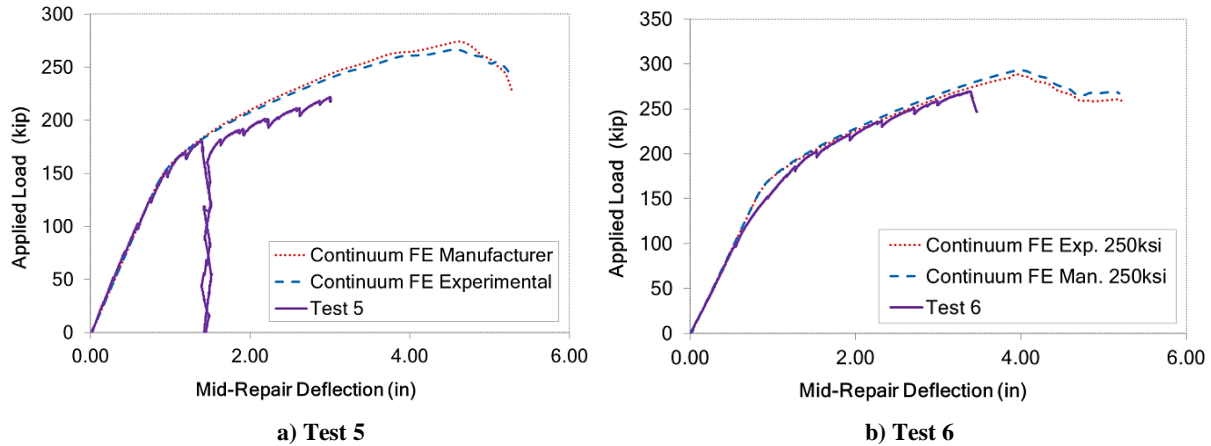
56

a) Test 5	b) Test 6

Figure 69. Experimentally and Analytically Obtained Load-Deflection Curves for Tests 5 and 6

For the Test 6 continuum-based FE model, the two analyses were of the two different FRCM material model scenarios, both using a 250-ksi strand splice strength. The first analysis used the elastic manufacturer's model scenario. The second analysis used the bilinear experimental model scenario. The results of these analyses are shown in Figure 69b. Both analyses showed concrete crushing as the failure mode. Just as in the nonlinear beam analyses, both analyses agree with the experimental data.

Summary of Results and Discussion

A summary comparison between the experimental tests and the validation analyses using the beam models is presented in Table 23. A similar comparison is summarized in Table 24 for the FE models. Overall, both the beam models and FE models provided very satisfactory estimates of the peak strength and the deflection at failure for all the girders.

The validation analyses allowed the researchers to determine which alternative stress-strain curves should be employed for the various retrofit measures, in the remainder of the present study. Regarding the strand-splice repair, a splice failure stress of 225 ksi was selected for the eight-strand splice, while a failure stress of 250 ksi was selected for the four-strand splice. For the retrofit using overlays of FRP and FRCM, the validation analyses were inconclusive. The fact that no significant damage was observed in the retrofitted tensile zones of the cross-sections precludes the reliable determination of which of the alternative stress-strain curves should be used. Given that the analysis in the next section focuses on prototype girders that fail in the tension zone, and to provide conservative results, the stress-strain curves that give the minimum retrofit strength were used for the FRP and FRCM. Thus, the stress-strain curve corresponding to crack-induced debonding of the FRP and the curve obtained from the FRCM material tests were used for the remainder of this study.

Table 23. Summary of Comparison between Experimental Test Results and Beam Models

Analysis	Experimental Peak Load, kips	Experimental Maximum Deflection, in	Predicted Load at Maximum Deflection, kips	Error (%)	Model Predicted Peak Load, kip	Model Predicted Max Defl., in
Test 1, Iteration 1	353	1.41	372	5.5	401	2.08
Test 1, Iteration 2	400	1.82	394	-1.4	399	2.08
Test 2, 212.5 ksi	195	3.39	179	-8.4	187	2.75
Test 2, 225 ksi	195	3.39	184	-6	198	3.05
Test 2, 237.5 ksi	195	3.39	208	6.3	208	3.4
Test 2, 250 ksi	195	3.39	209	7.1	232	3.78
Test 3, Debond	311	3.15	317	1.9	317	3.15
Test 3, Flexure	311	3.15	317	2	344	3.9
Test 4.1, 225 ksi	241	3.88	125	-48.1	218	3.42
Test 4.1, 250 ksi	241	3.88	240	-0.6	241	4.51
Test 4.2, 225 ksi	265	3.38	143	-45.9	245	2.85
Test 4.2, 250 ksi	265	3.38	269	1.4	270	3.32
Test 5, Manufacturer	181	1.39	183	14.3	274	3.94
Test 5, Experimental	181	1.39	181	11.0	256	3.65
Test 6, Man./ 225ksi	269	3.39	260	-3.3	273	4.17
Test 6, Man./ 250ksi	269	3.39	271	0.9	293	4.45
Test 6, Exp./ 225ksi	269	3.39	250	-7.1	253	3.66
Test 6, Exp./ 250ksi	269	3.39	264	-1.8	276	4.18

Table 24. Summary of Comparison between Experimental Test Results and FE Models

Analysis	Experimental Peak Load, kips	Experimental Maximum Deflection, in	Predicted Load at Maximum Deflection, kips	Error (%)	Model Predicted Peak Load, kips	Model Predicted Maximum Deflection, in
Test 1	400	1.82	427	6.7	456	2.39
Test 2, 225 ksi	195	3.39	202	3.4	230	6.99
Test 2, 237.5 ksi	195	3.39	203	3.7	233	7.07
Test 3, Debond	311	3.15	326	4.7	333	3.41
Test 3, Flexure	311	3.15	326	4.8	334	3.41
Test 4.1 (250 ksi)	241	3.88	240	-0.4	253	4.63
Test 5, Manufacturer	181	1.39	182	10.2	274	4.63
Test 5, Experimental	181	1.39	181	8.8	267	4.59
Test 6, Manufacturer	269	3.39	278	3.5	293	3.99
Test 6, Experimental	269	3.39	273	1.4	289	3.94

Results of Modeling In-Situ Beams

After the creation of analytical models for the six experimental tests, the one undamaged girder and five repair methods, it was important to use the analytical modeling tools to evaluate the effectiveness of these repair methods. The experimental data were not comparable because of the different spans being tested and the incompleteness of tests in showing full failure. Analytical modeling was used evaluate equivalent prototype girder test setups to make a direct comparison between repair methods. The direct comparison test chosen was with AASHTO loading conditions and limit states because these beams were initially designed in accordance with AASHTO provisions and any subsequent repairs would take into account these provisions. AASHTO LRFD Bridge Design Specification allows for the flexural design strength of each beam in a bridge to be determined with the addition of an effective width of the concrete deck (AASHTO 2010). This effective width of concrete deck accounts for the composite deck action that occurs in the actual bridge.

Prototype Girders

As a simplification, the girders were designed with effective width and loading appropriate for interior girders. It was understood that impact damage is more likely to occur on exterior girders, but the inclusion of parapets complicates the analysis (Harries, 2006). The main goal was to provide repair designs and model the repaired girder in order to verify the strength of the repair. Therefore, all girders modeled were considered to be interior and exclude parapets that add biaxial bending.

From the provisions in AASHTO LRFD Specifications, Article 4.6.2.6 (AASHTO 2010), the effective width of the deck was found to be 88 in, corresponding to the center-to-center distance between adjacent bridge girders. The cross-section of the prototype girder with the full effective bridge deck is shown in Figure 70.

Two different limit states were used to verify the effectiveness of the repairs: strength and serviceability. To serve its purpose, a structure must be serviceable under ordinary use and must be safe against collapse (Nilson, 1987). Considerations for strength and serviceability are found in Article 3.4.1 of AASHTO LRFD (AASHTO, 2010). The design load for Strength I criteria was checked against the nominal capacity found through the analysis. Serviceability requires that deflections be suitably small, crack widths be kept within acceptable limits, and vibrations be minimized. Dead and live loads are applied with the Service I and Service III load factors. Compressive and tensile stresses in concrete and tensile stresses in the strands were checked for adequacy. In addition, the concrete section was checked to see if it remains uncracked.

Bridge load calculations were completed according to AASHTO LRFD (AASHTO 2010) specifications and are compiled in Table 25. Dead loads considered were the self-weight of the deck, self-weight of the girder, wearing surface, parapets, deck forms, and miscellaneous loads. Live loads were calculated based on a lane load and the loads of the more critical HS-25 vehicle and the design Tandem vehicle. Since this specific bridge was built around 1960, it was originally designed for a lower HS-20 vehicle loading according to the 1960 AASHO Specifications. The total loads for the HS-20, HS-25, and Tandem trucks, including dead loads

from various components, are shown in Table 25. From calculations, it was determined that the HS-25 was the more critical to represent the conditions of modern loading. Load factors were calculated from the provisions in Article 3.4.1. The load factors considered were with three limit states: Strength I, Service I, and Service III.
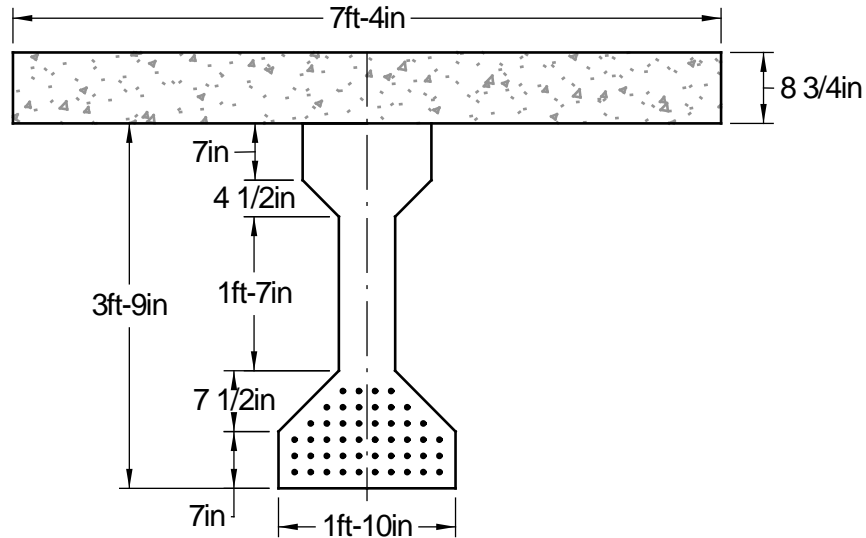

Figure 70. Prototype Girder Cross Section with Effective Bridge Deck

Table 25.   AASHTO Load Calculation Summary

Load Source	Loading	Moment	Strength I	Service I	Service III	Units
Deck	0.85 k/ft	356	446	356	356	k-ft
Girder	0.57 k/ft	240	300	240	240	k-ft
Parapets	0.25 k/ft	105	131	105	105	k-ft
Deck Forms	0.09 k/ft	38	47	38	38	k-ft
Miscellaneous	0.015 k/ft	6	8	6	6	k-ft
Wearing Surface	0.082 k/ft	34	52	34	34	k-ft
Lane	0.64 k/ft	269	467	267	213	k-ft
HS20	HS20	764	1,760	1,010	805	k-ft
HS25	HS25	955	2,200	1,260	1,010	k-ft
Tandem	TANDEM	675	1,560	890	712	k-ft
Total under HS20 (1960)			3,210	2,050	1,800	k-ft
Total under HS25 (2010)			3,650	2,310	2,000	k-ft
Total under Tandem (2010)			3,010	1,940	1,710	k-ft

The prototype analyses were modeled after considerations of the bridge plans and the test setup used for the full girder test in Test 2. The prototype girder analysis was a 58-ft simple span that was damaged 4 ft on either side of the midpoint. Damage was inflicted at the mid-span because typical impact damage from over-height vehicles occurs around the mid-span of girders, where a truck is likely to hit. The length of damage on the prototype girder was 8 ft based on data from the YRC Freight Company, which indicated the average width of a semi-trailer as approximately 8 ft (YRC Worldwide, 2015).

Two different sets of analyses were conducted on the girders. The first set of analyses was completed to check strength limits. The Strength Analysis configuration is shown in Figure 71. The load was applied as two point loads placed straddling the mid-span to keep the repaired section within a constant moment region. Thus, full flexural failure was initiated in the repaired region to show the strength of the repair. The girder strength was then compared to the Strength I load combinations for the HS-20 and HS-25 truck loadings, as well as used as direct comparison of repair strength.
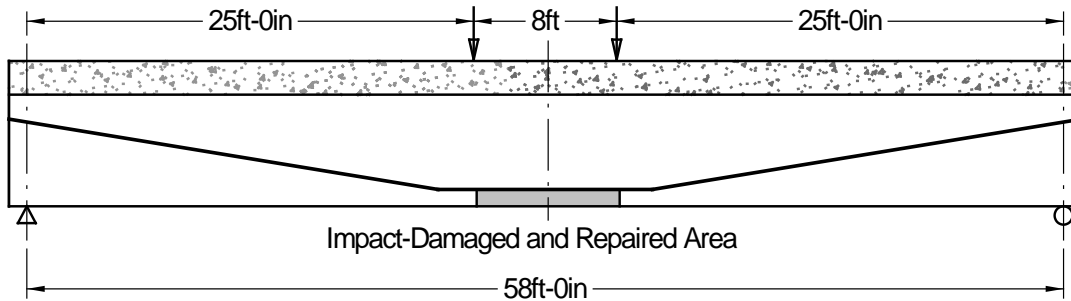
Figure 71. Prototype Girder Strength Analysis Configuration

The second set of analyses was completed to check the serviceability limit states. During these service analyses, the Service I load combination was applied to check the compressive stresses in the concrete and tensile stresses in the steel strands. The Service III load combination was applied to the check the tensile stresses in the concrete. Figure 72 shows the configuration of this Service Analysis, with HS-25 truck loading to represent 2010 design standards. Additionally, the analysis was repeated with HS-20 truck loading to represent 1960 design standards.

Given that the nonlinear beam models provided very good results for the girders tested, such models were employed in this section for the analysis of the prototype bridges.
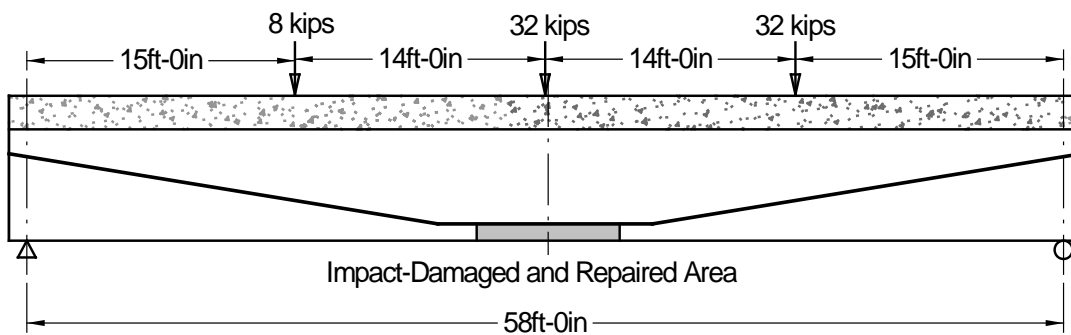
Figure 72. Prototype Girder Service Analysis Configuration with HS-25 Truck Loading

Analysis of Prototype Girders using Nonlinear Beam Models

All five of the repair methods investigated in the experimental tests were modeled. The material strengths used for both the concrete and steel strands were experimentally tested values. For the splice repairs, it was assumed that the splices would have the same cross-sectional area

as the other prestressing strands. For the FRP repairs, it was assumed that the two layers of FRP fibers would be 0.16 in thick and span the entire 22 in of the bottom flange. For the FRCM repairs, it was assumed that each of the four layers of FRCM fabric was 0.0018 in thick and all were located on the entire bulb of the bottom flange.

Analysis for AASHTO Strength Limit States

For the Prototype Girder Strength Analysis nonlinear beam model, a displacement-controlled analysis was conducted using OpenSees. The displacement was controlled at the load points and the corresponding force required to displace these nodes was measured. The moment and curvature of elements in the constant moment region were recorded during the analysis. This led to a moment-curvature plot that showed the response of the beam under the recreated testing scenario. From the moment-curvature plot, two points were of interest: first yielding of strand and ultimate strength. Ultimate strength was important in finding repair capacity. The ratio of ultimate curvature to first yielding curvature, known as curvature ductility, was important in determining the ductility of each repair method. An ideal repair method would have good ductility to give warning of imminent girder failure. The results of these analyses are summarized in Table 26, and comparisons are presented in Table 27.

The first set of analyses included three baseline models of the girder: undamaged, four strands damaged, and eight strands damaged. The moment-curvature responses for these girders are shown in Figure 73. The failure modes for all three analyses were full flexural failure, with the steel reinforcing strands rupturing at an ultimate strain of 0.05. Ideally, the repairs would restore the full, undamaged capacity. If not this was not achieved, it would have to be verified that the repair method has enough strength capacity to satisfy the Strength I limit state. Table 27 compares all of the repairs, using the undamaged condition as a baseline to compare capacity and ductility. From observation, by damaging the strands, a significant loss in strength was seen: 91.2% capacity if four strands were damaged and 82.1% capacity if eight strands were damaged. However, ductility was not greatly reduced; the four-strands-damaged model reached 98.9% ductility and the eight-strands-damaged model reached 95.1% ductility.
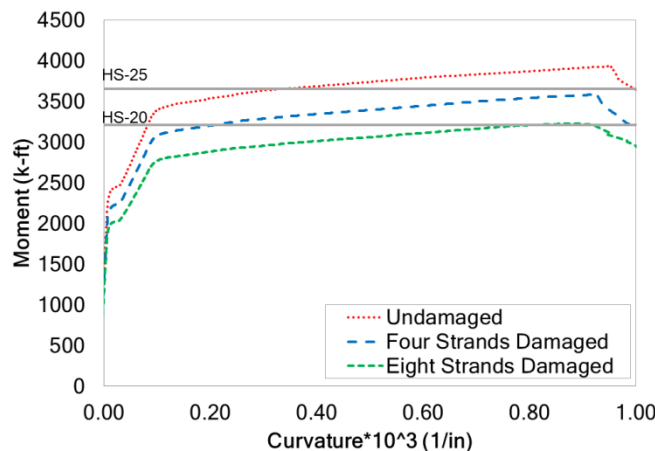

Figure 73. Moment-Curvature Response of Prototype Undamaged and Damaged Girder

The analyses were repeated with the five repair methods that were experimentally tested. The first was the four-strand splice repair as in Test 4. The moment-curvature response is shown in Figure 74a, as compared to the undamaged condition and the four-strands-damaged condition. The failure mode in the analysis was spliced strand rupture at a failure stress of 250 ksi, which is the full splice strength. According to the analysis, the repair restored 92.9% capacity and 37.4% ductility. After failure, the curve returned to the curve of the fully damaged condition, as expected.

The second repair analyzed was the eight-strand splice repair as in Test 2. The moment-curvature response is shown in Figure 74b, as compared to the undamaged condition and the eight-strands-damaged condition. The failure mode in the analysis was spliced strand rupture at a failure stress of 225 ksi, which corresponds to the premature splice strength failure observed in testing. The analysis indicated the repair restored 85.3% capacity and 11.5% ductility. The third repair analyzed was the four strands damaged with FRP repairs as in Test 3. The moment-curvature response is shown in Figure 75, as compared to the undamaged condition and the four-strands-damaged condition. The failure mode in the analysis was intermediate crack-induced debonding failure of the FRP at a strain of 0.0052. In this analysis, the repair restored 100.6% capacity and 11.6% ductility.
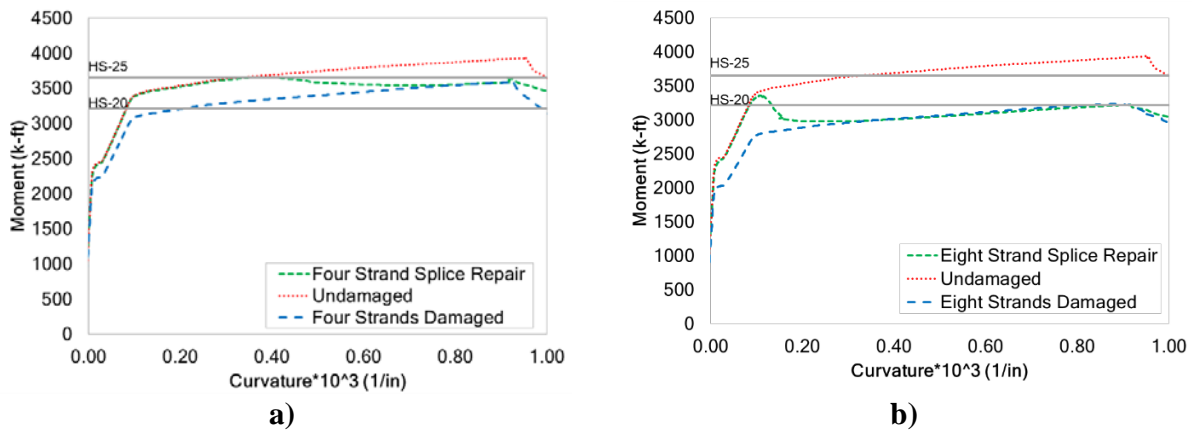

Figure 74. Moment-Curvature Response of Prototype Girder Investigating the Effect of Strand Splice Repair: a) Splice Repair on 4 Strands and b) Splice Repair on 8 Strands

The fourth repair analyzed was of four strands damaged with FRCM repair as in Test 4. The moment-curvature response is shown in Figure 76a, as compared to the undamaged condition and the four-strands-damaged condition. The failure mode in the analysis was FRCM debonding at a strain of 0.012. The analysis indicated the repair restored 90.2% capacity and 26.4% ductility. The final repair analyzed was the only combined repair method: four strands were damaged and both FRCM and strand splice repairs were applied as in Test 6. The moment-curvature response is shown in Figure 76b, as compared to the undamaged condition and the four-strands-damaged condition. The failure mode in the analysis was also FRCM debonding at a strain of 0.012. The analysis showed the repair restored 98.1% capacity and 26.4% ductility.
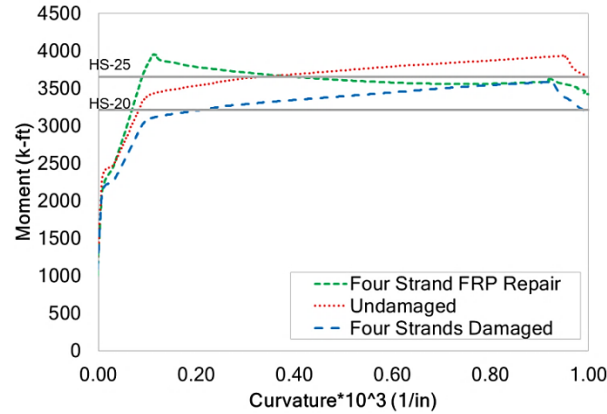
Figure 75. Moment-Curvature Response of Prototype Girder Investigating the Effect of an FRP overlay on a girder with 4 strands damaged
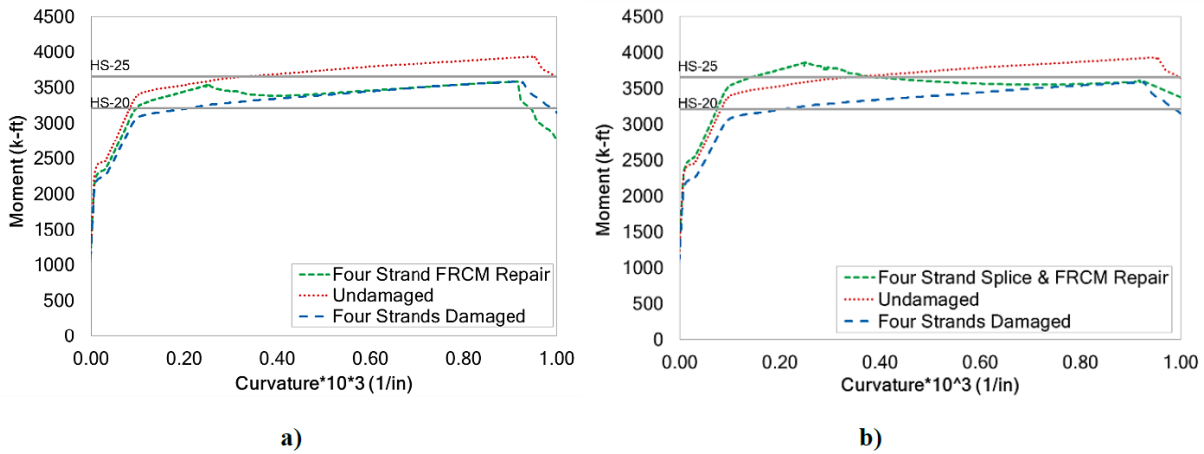

a)

b)

Figure 76. Moment-Curvature Response of Prototype Girder Investigating the Effect of a Repair Using FRCM Overlays: a) FRCM Overlay and 4 Strands Damaged and b) FRCM Overlay and Splice Repair on 4 Strands.

Table 26. Prototype Girder Strength Analysis Nonlinear Beam Model Summary

Case	Moment at First Yielding (k-ft)	Curvature at First Yielding (1/in)	Moment at Ultimate (k-ft)	Curvature at Ultimate (1/in)	Curvature Ductility
Undamaged	3,300	0.000088	3,930	0.00095	10.73
4 Strands Damaged	2,990	0.000087	3,580	0.00093	10.61
8 Strands Damaged	2,680	0.000087	3,230	0.00088	10.21
4 Strands Spliced	3,290	0.000088	3,650	0.00035	4.01
8 Strands Spliced	3,240	0.000088	3,360	0.00011	1.23
4 Strands FRP	3,630	0.000090	3,960	0.00011	1.25
4 Strands FRCM	3,130	0.000087	3,550	0.00025	2.83
4 Strands Spliced & FRCM	3,430	0.000088	3,860	0.00025	2.83

64

Table 27. Prototype Girder Strength Analysis Nonlinear Beam Model Comparison

Case	Percentage of Undamaged Capacity (%)	Percentage of Undamaged Ductility (%)	HS-20 Moment Demand (k-ft)	Percentage of HS-20 Demand Met (%)	HS-25 Moment Demand (k-ft)	Percentage of HS-25 Demand Met (%)
Undamaged	100	100	3,210	122	3,650	108
4 Strands Damaged	91.2	98.9	3,210	112	3,650	98.1
8 Strands Damaged	82.1	95.1	3,210	101	3,650	88.4
4 Strands Spliced	92.9	37.4	3,210	114	3,650	100
8 Strands Spliced	85.3	11.5	3,210	105	3,650	91.9
4 Strands FRP	101	11.6	3,210	123	3,650	108
4 Strands FRCM	90.2	26.4	3,210	110	3,650	97.1
4 Strands Spliced & FRCM	98.1	26.4	3,210	120	3,650	106

Analysis for AASHTO Service Limit States

For the Prototype Girder Service Test nonlinear beam model, a static analysis was conducted in OpenSees. The distributed loads from dead and live load, as well as the varying truck loads, were applied statically. Stresses in the concrete and steel fibers in the mid-span, where moment was at a maximum, were recorded. During these service tests, loading with the Service I load combination was applied to check the compressive stresses in the concrete and tensile stresses in the steel strands. The Service III load combination was applied to the check the tensile stresses in the concrete. These stresses were checked against AASHTO stress provisions (AASHTO 2010). Compressive stress in the concrete was limited to $0.45 \times f_c'$. Tensile stress in concrete was limited to $0.19 \times \sqrt{f_c'}$ (in ksi).   Tensile stress in prestressing strands was limited to $0.80 \times f_{pu}$. The section also had to be verified to be uncracked.

The analysis was conducted for HS-20 and HS-25 truck loading. These two loadings represent the design truck loadings for years 1960 and 2010, respectively. Under HS-20 loading criteria, the analysis revealed that all repairs, and even the fully damaged cases, were satisfactory. Under HS-25 loading criteria, the analysis, summarized in Table 28, reveals that all repairs satisfy the serviceability requirements. The only model that did not satisfy the serviceability requirements was the eight-strand damaged model, which showed cracking in the concrete in the tensile zone. Though it can be seen in the table that the tensile stress in the concrete was less than the service limit state, this was because the concrete had reached peak tensile strength and had effectively cracked.

Table 28. Prototype Girder Service Analysis Nonlinear Beam Model Comparison for HS-25 Truck Loading

Case	Compressive Stress at Top Deck Concrete, (ksi)	Service I Limit State, (ksi)	Tensile Stress at Bottom Girder Concrete, (ksi)	Service III Limit State, (ksi)	Tensile Stress at Bottom Girder Steel, (ksi)	Service III Limit State, (ksi)
Undamaged	-0.81	-2.71	0.24	0.49	144	200
4 Strands Damaged	-1.03	-2.71	0.40	0.49	159	200
8 Strands Damaged	-1.43	-2.71	0.32	0.49	198	200
4 Strands Spliced	-0.83	-2.71	0.27	0.49	145	200
8 Strands Spliced	-0.85	-2.71	0.29	0.49	146	200
4 Strands FRP	-0.92	-2.71	0.40	0.49	151	200
4 Strands FRCM	-0.89	-2.71	0.37	0.49	149	200
4 Strands Spliced & FRCM	-0.80	-2.71	0.19	0.49	144	200

DISCUSSION

Constructability of Repairs

There were several tasks required to complete each repair. The following are the tasks, general observations and the time and personnel required to perform each task.

- Each damaged location required saw-cutting along the perimeter of the repair to at least 1-in depth, and chipping of concrete around strands to prepare for the repair mortar. This operation took two students approximately three hours (6 man-hours) for each repair location.
- Strand splicing was a relatively quick and easy repair technique. The eight-strand repair required careful placement of the splices so they were not directly adjacent to each other. The repair took a three-man crew one hour to install four splices (3 man-hours).
- Formwork construction and placement of the repair mortar took two workers four hours (8 man-hours) to complete for each repair location. This task was always required regardless of the repair technique.
- Preparing the repaired concrete and mortar surface for the repairs by grinding and sand-blasting was a time-consuming process in the operation and required about the same time for either type of repair. For either type of repair, two workers required two hours (4 man-hours) per repair.

66

- In the field, the FRP should be applied to dry concrete, while the FRCM should be applied to saturated surface dry concrete. The FRP repair is more sensitive to weather conditions.
- Preparation and placing of the FRP and FRCM were very similar operations and took similar amounts of time, approximately five hours per repair for two workers (10 man-hours).
- The workers commented that they preferred the FRCM repair because the cementitious material is easier to work with than the epoxy and requires less personal protective equipment.

Based on these observations, adding splice chucks to any repair is relatively quick, easy and inexpensive. Using the chucks in tandem with one of the other repair techniques should provide considerable strength, and the additional repair (FRP or FRCM) will help protect the repair mortar in case of overloads that might crack it and result in durability problems. The FRP and FRCM repairs had many similarities in terms of application. The FRP has been field-proven over the years, while the FRCM is relatively new for bridge repairs. The advantages of the FRCM are that workers are familiar with cementitious mortar materials and that the workers do not need full protective suits or face masks that are needed for in FRP repairs.

Strength Returned by Repairs

For every test performed, hand-calculations of flexural strength were performed using the methods of the AASHTO LRFD Bridge Design Specifications (AASHTO 2010) along with recommendations from ACI 440.2R (2008) for FRP and ACI 549.4R (2013) for the FRCM. A strain compatibility approach was also employed. These methods provided conservative estimates of strength as summarized in Table 29.

Table 29. Comparison of AASHTO Method and Strain Compatibility Method to All Test Results

Test No.	Type of Repair	Tested Ultimate Moment, k-ft	AASHTO Nominal Moment, k-ft	Strain Compatibility Nominal Moment, k-ft	M_{test}/M_{AASHTO}	$M_{test}/M_{strain\ comp}$
1	Undamaged	3,220	2,950	2,930	1.09	1.10
2	8 strands spliced	2,800	2,780	2,720	1.01	1.03
3	FRP	3,540	3,540	3,580	1.00	0.99
4	4 strands spliced	3,160	2,740	2,710	1.15	1.17
5	FRCM	2,770	2,670	2,710	1.04	1.02
6	4 strands spliced and FRCM	3,300	2,840	2,890	1.16	1.11
				Average	1.08	1.07
				St. Dev.	0.07	0.07

Since the AASHTO method provided a good estimate of strength, it was used to calculate the undamaged strength of each tested location. The undamaged strength varied slightly from test to test because of differences in the top slab dimensions and eccentricity of the prestressing strand. Table 30 compares the calculated undamaged strength to the tested strength to evaluate the repair methods' ability to return a beam to its undamaged strength.

Table 30. Comparison Calculated Undamaged Strength to Tested Repaired Strength

Test No.	Type of Repair	Tested Ultimate Moment, k-ft	AASHTO Undamaged Nominal Moment, k-ft	$M_{repaired}/M_{undamaged}$
1	Undamaged	3,220	2,950	1.09
2	8 strands spliced	2,800	2,770	1.01
3	FRP	3,540	2,740	1.29
4	4 strands spliced	3,160	2,740	1.15
5	FRCM	2,770	2,710	1.02
6	4 strands spliced and FRCM	3,300	2,710	1.22

As can be seen from the table, all the repair techniques were able to return the beams to their undamaged strength. The eight-strands-spliced and FRCM repairs alone provided only slight increases in strength, while the FRP and the FRCM combined with splices provided significant additional strength to the beam.

As mentioned previously, the test beams were not ideal representations of a composite beam with effective slab width because of the narrow top flange width, which resulted from the demolition techniques. Since the AASHTO method was shown to provide reasonable and conservative estimates of strength, it was also used to model more realistic in-situ beam scenarios. Table 31 presents calculations based on the Type III beam with the full effective width of composite slab in the Arcadia Bridge, which is 7 ft – 4 in, at mid-span of the beam.

This table indicates that when the expected failure mode is tension-controlled, rather than the compression-controlled failures seen in the test beams, the repairs are not as effective at returning original strength. The best options, based on this table, are also the FRP repair and the FRCM repair used in tandem with splice chucks. Note that this is the same conclusion that would be drawn based on the non-linear beam model results presented in Table 27. The values are different, but the two repairs with the best performance were the same. Also note that, even with FRCM, when the number of spliced strands becomes larger, it is difficult to return the beam to full strength.

Table 31. Returned Strength from Repairs for Beams with Full Width Deck

Type of Damage and Repair	Undamaged Strength, k-ft	Repaired Strength, k-ft	$M_{repaired}/M_{undamaged}$
4 strands spliced	3,610	3,580	0.99
8 strands spliced	3,610	3,500	0.97
4 strands severed with FRP repair	3,610	4,560	1.26
4 strands severed with FRCM repair	3,610	3,540	0.98
4 strands severed with FRCM and splice repair	3,610	3,890	1.08
8 strands severed with FRCM and splice repair	3,610	3,590	0.99
12 strands severed with FRCM and splice repair	3,610	3,300	0.91

It should be noted that FRCM is a relatively new repair technique. It has been used extensively in concrete and masonry repairs in buildings and parking garages, but has not seen wide application in bridges. Several aspects of installation and performance should be studied further, including the effects of installing the system on a structure that might be open to traffic at the time. The long-term fatigue behavior of the system should also be studied further.

Non-linear Modelling

The repair that performed the best in terms of strength capacity restored was the four-strand FRP repair, at 100.6% post-repair strength, though it provided a mere 11.6% of the ductility of the undamaged condition. The repair that restored the most ductility was the four-strand splice repair with 37.4% ductility restored, though it provided only 92.9% capacity. The strength improvement was minor compared to the 91.2% capacity of the four-strand damaged condition. The repair with the best combination of capacity and ductility restored was the four-strand combined FRCM and splice repair. This repair restored 98.1% capacity and 26.4% ductility.

Table 27 compares the capacity of the repair methods to the different Strength I service limit states. From observation, all repair methods, even the fully damaged cases, satisfy the HS-20 design loading used in 1960. Only the three previously mentioned repair methods (four-strand splice, four-strand damage with FRP repair, and four-strand damage with FRCM and splices) satisfy the HS-25 design loading used in 2010.

Comparison of All Models

All of the possible analytical models investigated in this project (AASHTO LRFD, strain compatibility, non-linear beam and non-linear FEA) provided conservative estimates of damaged and repaired strength. The simple LRFD approach, with recommendations for the FRP and FRCM provided by ACI (ACI 440 (2008) and ACI 549 (2013)) is adequate for the determination of repaired strength for cases in which 15% or fewer strands are severed and repaired. The other three methods should be considered for more severely damaged beams, or cases in which many beams in one span are damaged, and distribution of load is also a concern. The other methods can provide detailed information about moment-curvature and load-displacement behavior, which cannot be determined with the simple sectional model of AASTHO LRFD.

CONCLUSIONS

Conclusions from Observations of Repairs

- *The FRCM repair is very feasible from a constructability standpoint.* Multilayer repairs can be applied quickly because no drying time is required for the mortar between layers.

- *Splice chucks are easily installed and effective in developing most of the original strength of the strands.* However, the effectiveness is reduced as the number of splices in one location increases.

- *FRCM and FRP repairs take similar levels of effort to install, but the FRCM cementitious matrix is generally more familiar to construction workers and requires less personal protective gear.*

Conclusions from Testing and Simple Analysis

- *The AASHTO LRFD (2010) method for calculating flexural strength, using measured material properties, provides a conservative estimate of tested capacity of the undamaged beam.*

- *Using the recommendations of ACI440.2R (2008) for the added strength from the FRP and ACI549.4R (2013) for the added strength of the FRCM in conjunction with the AASHTO LRFD method results in conservative estimates of strength of the repaired beams.*

- *Assuming that the splice chucks will allow the strands to achieve 100% of their ultimate strength is conservative when calculating strength using LRFD. However, based on more detailed analysis, 100% was conservative for four-strand repairs, but 85% of ultimate strength was conservative for eight-strand repairs.*

- *The strain compatibility approach also provides good estimates of strength, but is more time-consuming to perform.*

- *Based on AASHTO-guided estimates of undamaged strength, all of the repair methods can return the impact-damaged beams to the AASHTO calculated strength.*

- *Even for low levels of damage, a combination of FRP repair or FRCM repair along with strand splicing can achieve a better strength return, compared to any single repair technique used alone.*

- *There is still a fair amount of uncertainty with regards to the durability of FRCM under heavy cyclic loading.* Certainly FRCM repairs have proven to be very feasible for repair of bridge beams that have been impacted by over-height vehicles. Additionally, modeling techniques have provided good estimates of strength of beams repaired with FRCM. However, the modeling up to this point has not considered other real-world scenarios in which a bridge is subjected to high, heavy truck traffic.

Conclusions from Non-linear Beam and FE Analysis

- *The excellent accuracy of the beam models indicates that these models can be used alone for the preliminary performance assessment of damaged and repaired girders.* Of course, the analyst must always be aware of the fact that a beam model cannot explicitly account for potentially crucial effects such as diagonal cracking.

- *The validated simulation tools enable extensive parametric performance assessment for damaged and repaired bridge beams and systems.* The beam-based models can even be used in practice, for the assessment of the impact of collision-induced damage and the selection of repair techniques (if necessary) for actual bridge systems.

- *Evaluations of allowable stresses were performed using the non-linear beam model, and all repair methods were able to keep the original concrete within allowable stresses. Since repair concrete is not prestressed, it is more likely to crack.*

RECOMMENDATIONS

1. *For hand calculations of original and repaired strength, VDOT's Structure and Bridge Division and District engineers* should use ACI440.2R (2008) for the added strength from the FRP, and ACI549.4R (2013) for the added strength of the FRCM along with the AASHTO LRFD method for flexural strength. These methods provide conservative estimates of repaired strength.

2. *For hand calculations of original and repaired strength, VDOT's Structure and Bridge Division and District engineers can assume that splice chucks can develop 100% of the strength of the tendon. However, based on the results of the more detailed methods, the engineer should be granted the discretion to reduce the assumed strength.*

3. *VDOT's Structure and Bridge maintenance crews and contractors should only use splice chucks alone if the number of strands severed is no more than 15% of the total number of strands, and there is adequate space to splice the strands without congestion.*

4. *VDOT's Structure and Bridge maintenance crews and contractors should consider combination repairs such as splices with FRP or splices with FRCM for severe repairs.* The concrete patch material will very likely crack under the combination of shrinkage and service loadings. The FRP or FRCM over the repair concrete not only provides added strength but also protects the patch mortar and prestressing steel from deterioration related to this cracking, and ensuing ingress of water and salts and corrosion of strand.

5. *For the time being, VDOT's Structure and Bridge Division should not allow FRCM repair to be used on bridges with high truck traffic.*

BENEFITS AND IMPLEMENTATION PROSPECTS

Like the rest of the United States, Virginia is not immune to bridge strikes by over-height vehicles, particularly with bridges crossing over the Interstate system. In some cases, the damage is merely cosmetic; in other cases, the damage can be severe enough to cause District Bridge Engineers to close the bridge to traffic. Those closures can be costly in terms of the construction to replace a single or multiple beams, as well as the disruption to traffic. The results of this research can help to mitigate both the replacement costs and the traffic disruptions by keeping the damaged beams in place and repairing them back to service strength in less time than would

be needed for replacement. Furthermore, this study provides guidance for calculating the strength regained by the repairs using FRP, FRCM, splice chucks, or a combination thereof. These calculations will give District Bridge Engineers the confidence needed to ensure the safety of the traveling public while keeping Virginia moving.

Based on the findings of this report, *VDOT Structure and Bridge Division* will implement *Recommendations 1* through *4* by incorporating appropriate guidance for repair of prestress girders into the *VDOT Manual of the Structure and Bridge Division, Part 2: Design Aids and Typical Details, Chapter 32 – Maintenance and Repair*. These guidelines will be put in place by January 2018.

ACKNOWLEDGMENTS

REFERENCES

American Association of State Highway and Transportation Officials. *AASHTO LRFD Bridge Design Specifications.* American Association of State Highway and Transportation Officials, Washington, DC, 2010.

American Association of State Highway and Transportation Officials. *Guide Specifications For Design Of Bonded FRP Systems For Repair And Strengthening Of Concrete Bridge Elements.* American Association of State Highway and Transportation Officials, Washington, DC, 2012.

ACI Committee 318. *Building Code Requirements for Structural Concrete and Commentary (ACI 318-14).* American Concrete Institute, Farmington Hills, MI, 2014.

ACI Committee 440. *Guide for the Design and Construction of Externally Bonded FRP Systems for Strengthening Concrete Structures* (ACI 440.2R). American Concrete Institute, Farmington Hills, MI, 2008.

ACI Committee 549. *Guide to Design and Construction of Externally Bonded Fabric-Reinforced Cementitious Matrix (FRCM) Systems for Repair and Strengthening Concrete and Masonry Structures* (ACI 549.4R). American Concrete Institute, Farmington Hills, MI, 2013.

ASTM C109/C109M – 13 *Standard Test Method for Compressive Strength of Hydraulic Cement Mortars (Using 2-in. or [50-mm] Cube Specimens)* ASTM International, West Conshohocken, PA, 2013. http://www.astm.org/Standards.htm Accessed May 2, 2015.

ASTM D3039/D3039M – 08, *Standard Test Method for Tensile Properties of Polymer Matrix Composite Materials.* ASTM International, West Conshohocken, PA, 2008. http://www.astm.org/Standards.htm Accessed May 2, 2015.

Agrawal, A. K., Xu, X., & Chen, Z.. *Strikes on Low Clearance Bridges by Over-Height Trucks in New York State*. United States Department of Transportation, Washington, 2013. http://www.rita.dot.gov/utc/sites/rita.dot.gov.utc/files/utc_spotlights/pdf/spotlight_0113.pdf Accessed December 05, 2014.

Broadhouse, B.J. *The Winfrith Concrete Constitutive Model in LS-DYNA3D*. Report SPD/D(95)363, AEA Technology, 1995. http://ftp.lstc.com/anonymous/outgoing/jday/concrete/Winfrith_Paper_Feb1995.pdf

Chang, F.K., and Chang, K.Y., A Progressive Damage Model for Laminated Composites Containing Stress Concentration. *Journal of Composite Materials*, 21, 1987, pp. 834-855.

Di Ludovico, M., Nanni, A., Prota, A., and Cosenza, E. Repair of Bridge Girders with Composites: Experimental And Analytical Validation. *ACI Structural Journal*, Vol. 102 No. 5, 2005, pp. 639-648.

Gangi, M.J. *Analytical Modeling of the Repair of Impact Damaged Prestressed Concrete Bridge Girders.* Master's Thesis, Virginia Tech, Blacksburg, Va, 2015.

Hallquist, J. O. *LS-DYNA Keyword User's Manual*. Livermore Software Technology Corporation, 2007.

Harries, K. *Full-scale Testing Program on De-commissioned Girders from the Lake View Drive Bridge*. University of Pittsburgh, Pittsburgh, PA, 2006.

Harries, K. A., Kasan, J., and Aktas, C. *Repair Methods for Prestressed Girder Bridges.* University of Pittsburgh, Department of Civil and Environmental Engineering. Harrisburg: Commonwelth of Pennsylvania Department of Transportation, 2009.

Harries, K. A., Kasan, J., Miller, R., and Brinkman, R. *Updated Research for Collision Damage and Repair of Prestressed Concrete Beams*. NCHRP Project 20-07, Task 307, University of Pittsburgh, Department of Civil Engineering, Pittsburgh. 2012.

Hisham, M., and Mohd, Y.. *Nonlinear Analysis of Prestressed Concrete Structures under Monotonic and Cycling Loads*. PhD dissertation, University of California, Berkeley, 1994.

Hognestad, E.. *Ultimate Strength of Reinforced Concrete in American Design Practice.* Research and Development Laboratories. London: Portland Cement Association, 1956.

International Code Council Evaluation Service (ICC-ES) *Physical and Mechanical Properties of FRP Composite Materials*, AC125, ICC Evaluation Service, LLC, 2013a.

International Code Council Evaluation Service (ICC-ES) *Acceptance Criteria for Masonry and Concrete Strengthening Using Fabric-reinforced Cementitious Matrix (FRCM) Composite Systems*. AC434, ICC Evaluation Service, LLC, 2013b.

International Code Council Evaluation Service. *ICC-ES Evaluation Report - V-Wrap Fiber-Reinforced Polymer Composite System.* ESR-3606, Report Holder: Structural Technologies, LLC, published by ICC Evaluation Service, LLC 2014. http://www.icc-es.org/Reports/pdf_files/load_file.cfm?file_type=pdf&file_name=ESR-3606.pdf Accessed October 20, 2016.

Jones, M.S. *Repair of Impact Damaged Prestressed Bridge Girders with Strand Splices and Fabric Reinforced Cementitious Matrix Systems,* Master's Thesis, Virginia Tech, Blacksburg, Va, 2015.

Labia, Y., Saiidi, M. and Douglas. *Evaluation and Repair of Full-Scale Prestressed Concrete Box Girders.* Report No. CCEER-96-2, University of Nevada, Reno, NV, 1996.

Liesen, J.A. *Repair of Impact-Damaged Prestressed Bridge Girders Using Strand Splices and Fiber Reinforced Polymer,* Master's Thesis, Virginia Tech, Blacksburg, VA, 2015.

Loflin, B. J. *Bond and Material Properties of Grade 270 and Grade 300 Prestressing Strands.*, Master's Thesis, Virginia Tech, Blacksburg, VA 2008.

Michael, A. *Moment-Curvature: Bonded Tendons.* Retrieved May 5, 2015, from Frederick University, Department of Civil Engineering ACES 480 Class Notes, 2010. http://staff.fit.ac.cy/eng.ma/Aces480notes/Prestressed_Moment_Curvature.pdf

Mazzoni, S., McKenna , F., Scott, M., and Fenves , G. *Opensees Command Language Manual*. Berkeley, CA: Pacific Earthquake Engineering Research (PEER) Center, 2006.

McGuire, W., Gallagher, R., and Ziemian, R. *Matrix Structural Analysis: Second Edition.* CreateSpace Independent Publishing Platform, 2015.

Nanni, A. Carbon FRP Strengthening: New Technology Becomes Mainstream. *Concrete International: Design and Construction*, Vol 19, No 6, June, 1997, pp. 19-23.

Nanni, A. FRCM Strengthening – A New Tool in the Concrete and Masonry Repair Toolbox. *Concrete International: Design and Construction*, April 2012.

Nilson, A. H. *Design of Prestressed Concrete (2nd ed.)*. John Wiley & Sons, New York, New York, United States, 1987.

Ottosen, N. S. A Failure Criterion For Concrete, *Journal of Engineering Mechanics*, Vol 103, 1977, 527-535.

Pino, V., and Nanni, A. *Repair of Damaged Prestressed Concrete Girder with Fabric Reinforced Cementitious Matrix and Fiber Reinforced Polymer Composites*. University of Miami, College of Engineering, Gables, FL, 2015.

Prestress Supply Incorporated. *Grabb-It Cable Splice*. Retrieved December 12, 2014, from Prestress Supply, 2010 http://www.prestresssupply.com/Products/StrandRepair/GRABBITCableSplice.aspx

Shanafelt, G.O. and Horn, W.B., *Damage Evaluation and Repair Methods for Prestressed Concrete Bridge Members.* NCHRP Report 226, Project No. 12-21, Transportation Research Board, Washington, DC, 1980.

Shanafelt, G.O. and Horn, W.B., *Guidelines for Evaluation and Repair of Prestressed Concrete Bridge Members.* NCHRP Report 280, Project No. 12-21(1), Transportation Research Board, Washington, DC, 1985.

Teng, J., Chen, J., Smith, S., and Lam, L. *FRP Strengthened RC Structures*. John Wiley & Sons, West Sussex, England, 2002.

Tumialan, G. FRCM Systems. *Structrures Magazine,* 2014.

Virginia Department of Highways (VDOH), "RTE. 614 Underpass Plan Set", Office of the Bridge Engineer, Richmond, VA, August 1957.

Wipf, T.J., Kalaiber, F.W., Rhodes, J.D. and Kempers, B.J.. *Effective Structural Concrete Repair.* Report to the Iowa Department of Transportation, Iowa State University, Ames, IA, 2004.

YRC Worldwide. *Trailer Dimensions*. (WordPress.com) Retrieved February 8, 2015, from YRC Freight: http://yrc.com/trailer-dimensions/

Zobel, R.S., Jirsa, J.O., Fowler, D.W., and Carrasquillo, R.L. *Evaluation and Repair of Impact-Damaged Prestressed Concrete Bridge Girders.* Report to the Center for Transportation Research, The University of Texas at Austin, Austin, TX 1997.